Alexander Jedinger, BSc

Development of a real-time simulation model of hybrid powertrains in motorsports

MASTER'S THESIS

to achieve the university degree of
Diplom-Ingenieur

Individual Master's Degree Program
Electrical and Automotive Engineering

submitted to

Graz University of Technology

Supervisors:

Dipl.-Ing. Martin Ackerl
Dipl.-Ing. Dr.techn. Jürgen Fabian
Institute of Automotive Engineering

Dipl.-Ing. Christoph Leichtfried
AVL List GmbH

Graz, June 2015

AFFIDAVIT

I declare that I have authored this thesis independently, that I have not used other than the declared sources/resources, and that I have explicitly indicated all material which has been quoted either literally or by content from the sources used. The text document uploaded to TUGRAZonline is identical to the present master‘s thesis dissertation.

---------- ----------
Date Signature

ACKNOWLEDGMENT

I am using this opportunity to express my gratitude to everyone who supported me throughout the course of this thesis. I am thankful for their aspiring guidance, invaluable and constructive criticism and friendly advice during the project work.

I would like to thank AVL List GmbH, for giving me the opportunity and the resources to work on this project. A special thanks to my supervisor, Mr. Christoph Leichtfried, who was always there to support me.

To my supervisors at the university, Mr. Jürgen Fabian and Mr. Martin Ackerl, I would like to express my gratitude for their guidance. Through critical thinking and constructive criticism, they helped to author a sophisticated and well-structured thesis. Thank you very much for the time and effort.

Many thanks to the Electric Drives and Machines Institute, especially Mr. Klaus Krischan and Mr. Heinrich Eickhoff, for their support and expertise. I am grateful for their excellent help on difficult technical issues, often provided on very short notice.

Finally, I would like to express my sincere gratitude to my family. My parents, for giving me the freedom and opportunity to pursue this degree, and the continuous support throughout my education. And my siblings, for the emotional support and trust. In addition, I want to thank my girlfriend, Ariel, for the countless hours of listening and proofreading.

KURZFASSUNG

Die Verwendung von Elektro- und Hybridantrieben im Motorsport nimmt stetig zu und stellt die Fahrzeugentwicklung und -simulation vor neue Herausforderungen. Die Entwicklung von Betriebsstrategien für diese neuen Komponenten erfordert detaillierte Modelle für alle Teile des Antriebsstranges, um maximale Leistung bei minimalem Kraftstoffverbrauch zu erreichen.

Ziel der Arbeit war die Entwicklung eines MATLAB® Simulink® Modells für Elektromotoren und Frequenzumrichter in Hybridantrieben für Anwendungen im Motorsport. In Zusammenarbeit mit der Rennsportabteilung der AVL List GmbH wurde ein Modell entwickelt, das anhand von Messungen am Prüfstand und allgemeinen Motordaten parametriert werden kann. Dieser Ansatz ermöglicht die Abbildung aller gängiger Radialflussmaschinen, ohne genaue Kenntnis über deren innere Strukturen. Neben dem elektromechanischen Verhalten wurden auch die thermischen Eigenschaften der Komponenten abgebildet. Das Modell ist echtzeitfähig, und kann für verschiedene Antriebsstrangkonfigurationen verwendet werden. Das entwickelte Modell wurde mit einem realen Antriebssystem verifiziert, allerdings konnten aufgrund fehlender Messungen nicht alle Eigenschaften überprüft werden.

Schließlich wurde das Modell in das bestehende Gesamtfahrzeugsimulationsmodell von AVL (*Vehicle Simulation Model – Powertrain Model VSM-PTM*) integriert. Dies wird sowohl als reine Software-Simulation als auch als Teil von Hardware-in-the-Loop Prüfständen eingesetzt. Die Simulationsergebnisse können als plausibel angesehen werden, müssen aber erst mit Messungen eines realen Antriebsstranges verifiziert werden.

ABSTRACT

The use of hybrid and electric propulsion systems in motorsports is rising continuously, posing new challenges for vehicle models and simulations. This requires detailed models of all parts of the powertrain. The development of operating strategies to incorporate these new hybrid and electric components is necessary in order to achieve maximum performance at the lowest fuel consumption.

The main objective of this project, done in close collaboration with the racing department of AVL List GmbH, was to create a MATLAB® Simulink® model of electric motors and inverters in hybrid electric powertrains used in motorsports. A model was developed that can be parameterized with a defined set of measurements from a test bench and basic specifications of an electric drive. This approach allows for its use for all major types of radial flux machines without requiring detailed knowledge of the drive's inner structure. Both the electromechanical and thermal behavior of the motor and inverter were described. The model is capable of operation in real time and can be adjusted to different powertrain layouts. It was verified with an existing electric drive, however, some features could not be tested due to a lack of measurements.

The model was integrated into AVL's existing simulation software, *Vehicle Simulation Model - Powertrain Model (VSM-PTM)*. In VSM-PTM, the model operates as a standalone software model and on real time platforms as part of Hardware-in-the-Loop tests. The simulation results seem plausible and are awaiting verification with measurements from a real powertrain.

ACRONYMS AND ABBREVIATIONS

ACO	Automobile Club de l'Ouest
AVL	Anstalt für Verbrennungskraftmaschinen List GmbH
DC	Direct Current
ERS	Energy Recovery System
FEA	Finite Element Analysis
FIA	Fédération Internationale de l'Automobile
HEV	Hybrid Electric Vehicle
HiL	Hardware in the Loop
HV	Hybrid Vehicle
ICE	Internal Combustion Engine
IM	Induction Motor
IPM	Interior Permanent Magnet Motor
KERS	Kinetic Energy Recovery System
MGU-H	Motor Generator Unit Heat
MGU-K	Motor Generator Unit Kinetic
RMS	Root Mean Square
SPM	Surface Mounted Permanent Magnet Motor
VSM-PTM	Vehicle Simulation Model – Powertrain Model

TABLE OF SIGNS AND SYMBOLS

Symbol	Unit	Description
a	m²/s	Thermal diffusivity
$A_{cu,th}$	m²	Contact area between winding and stator teeth
$A_{cu,yk}$	m²	Contact area between winding and stator yoke
A_{slot}	m²	Contact area between winding and stator iron
B	T	Magnetic flux density
c_d	-	Aerodynamic drag coefficient
$cos\varphi$	-	Power factor
C_p	J/(kg·K)	Specific heat capacity
C_{pn}	J/(kg·K)	Specific heat capacity
c_{rr}	-	Per wheel rolling resistance coefficient
d_c	m	Width of cooling jacket
d_{eq}	m	Equivalent thickness of air and insulation material in the stator slot
f	Hz	Frequency
$G_{cu,ir}$	W/K	Thermal admittance between copper and stator iron
G_{th}	W/K	Thermal admittance
H	A/m	Magnetic field strength
h_{airgap}	W/(m²·K)	Heat transfer coefficient of the airgap
h_{ch}	W/(m²·K)	Heat transfer coefficient coolant to housing
h_{yc}	W/(m²·K)	Heat transfer coefficient yoke to coolant
$\hat{I}$	A	Peak value of current
i_a, i_b, i_c	A	Phase currents for phase a, b, c
i_d	A	Current in direct axis
I_{DC}	A	Current from dc supply
$I_{dc,cell}$	A	DC current for each battery cell
I_{ph}	A	Phase current (RMS)
i_q	A	Current in quadrature axis
I_S	A	Stator phase current (RMS)
k_{air}	W/(m·K)	Thermal conduction coefficient of air
$k_{cu,ir}$	W/(m·K)	Equivalent thermal conduction coefficient of air and insulation material in the stator slot
k_{ir}	W/(m·K)	Thermal conduction coefficient of the stator core
l_C	m	Axial length of cooling jacket
L_d	H	Inductance in direct axis
L_q	H	Inductance in quadrature axis

Symbol	Unit	Description
l_s	m	Length (height) of stator
l_{sb}	m	Stator slot perimeter
l_{shf}	m	Length of shaft
m	kg	Thermal mass
m	kg	Vehicle mass
m_n	kg	Thermal mass of a specific thermal node
N_{Nu}	-	Nusselt number
N_{ph}	-	Number of phases
N_{Pr}	-	Prandtl number
N_{Ta}	-	Taylor number
p	-	Number of pole pairs
P_{cu}	W	Motor copper losses
P_{DC}	W	Heat flux from housing to environment
P_{el}	W	Electrical power
P_{Fe}	W	Motor iron losses
P_{fr}	W	Motor friction losses
p_{ir}	-	Ratio of tooth iron volume to total tooth plus slot volume
P_L	W	Power dissipation
$P_{L,cell}$	W	Power dissipation of each battery cell
$P_{L,inverter}$	W	Overall inverter losses
$P_{L,motor}$	W	Overall motor losses
$P_{L,other}$	W	Motor iron, friction and ventilation losses
P_{Ln}	W	Power dissipation in a specific thermal node
P_{mech}	W	Mechanical power
P_{PU}	kW	Overall power unit power
P_v	W	Motor ventilation losses
$\dot{q}$	W	Rate of heat transfer
$\dot{q}_{coolant2housing}$	W	Rate of heat transfer between coolant and housing
$\dot{q}_n$	W	Rate of heat transfer to/from a specific thermal node
$\dot{q}_{yoke2coolant}$	W	Rate of heat transfer between yoke and coolant
$R(T)$	Ω	Temperature dependent resistance
$R_{cu,ir}$	K/W	Thermal Resistance between copper and stator iron
R_i	Ω	Equivalent series resistance for each battery cell
r_{ir}	m	Inner radius of rotor iron core
r_{is}	m	Inner radius of stator teeth
r_{iy}	m	Inner radius of stator yoke
r_m	m	Mean radius of stator yoke
r_{mr}	m	Mean radius of rotor

Symbol	Unit	Description
r_{or}	m	Outer radius of rotor
r_{oy}	m	Outer radius of stator yoke
R_S	Ω	Mean stator winding resistance
R_{th}	K/W	Thermal resistance
R_{th1}	K/W	Thermal resistance between shaft and rotor
R_{th1}	K/W	Thermal resistance between junction and heatsink
R_{th2}	K/W	Thermal resistance between rotor and teeth
R_{th2}	K/W	Thermal resistance between heatsink and coolant
R_{th3}	K/W	Thermal resistance between teeth and yoke
R_{th3}	K/W	Thermal resistance between coolant and housing
R_{th4}	K/W	Thermal resistance between yoke and coolant
R_{th4}	K/W	Thermal resistance between housing and environment
R_{th5}	K/W	Thermal resistance between coolant and housing
R_{th6}	K/W	Thermal resistance between housing and environment
R_{th7}	K/W	Thermal resistance between winding and teeth
R_{th8}	K/W	Thermal resistance between winding and yoke
R_{U-V}	mΩ	Ohmic resistance between phase u and v
R_{V-W}	mΩ	Ohmic resistance between phase v and w
R_{W-U}	mΩ	Ohmic resistance between phase w and u
S_{cu}	m²	Cross-sectional area of copper in the stator slot
S_{slot}	m²	Cross-sectional area of stator slot
t	s	Time
T	Nm	Torque
T	K	Temperature
T_0	K	Initial temperature
T_{0n}	K	Initial temperature of a specific thermal node
T_{air}	K	Ambient temperature during dc test
T_{case}	K	Temperature of case during dc test
$T_{coolant}$	K	Mean temperature of coolant
T_{dem}	Nm	Demand torque
T_n	K	Temperature of a specific thermal node
T_{wi}	K	Inlet temperature of coolant
T_{wo}	K	Outlet temperature of coolant
$U_{a,b,c}$	V	Phase voltages for phase a, b, c
U_S	V	Stator phase voltage (RMS)
V_{DC}	V	Voltage from dc supply
w	kg	Mass of liquid in cooling jacket
$\dot{w}$	kg/s	Coolant mass flow

Symbol	Unit	Description
α_{cu}	K^{-1}	Temperature coefficient of copper
ΔT	K	Temperature difference
η	-	Efficiency
η_I	-	Inverter efficiency
η_M	-	Motor efficiency
η_{PU}	%	Overall power unit efficiency
ν	m^2/s	Kinematic viscosity
π	-	Ratio of circle's circumference to diameter
τ	s^{-1}	Time constant
Ψ_{PM}	Wb	Flux linkage from permanent magnets
ω	s^{-1}	Angular velocity

TABLE OF CONTENTS

1 INTRODUCTION

This thesis is about the design and development of a real-time model of hybrid powertrains for motorsports applications. The project was done in close collaboration with the racing department of AVL List GmbH (AVL).

1.1 MOTIVATION

The number of racing classes using hybrid electric propulsion systems is constantly rising, which creates new challenges for vehicle simulation. Not only are additional components, such as electric motors and batteries, increasing the complexity of the powertrain layout, they are also offering new ways of operation and control of the vehicle.

The Vehicle Simulation Model- Powertrain Model (VSM-PTM) contains detailed models for most parts of racing vehicles, including a sophisticated model for internal combustion engines (ICEs). However, the existing models for electric drives were very basic, based solely on a maximum torque over speed curve without accounting for efficiency or losses of the electric drive or the battery.

In order to maximize power output at a given fuel consumption and ultimately reduce lap time, all parts of the hybrid powertrain need to be modelled with great detail. For racing leagues with open regulations regarding the use of hybrid powertrain components (i.e. the 24 Hours of Le Mans), a flexible vehicle simulation model which covers a wide range of powertrain layouts is desirable. To fulfill these requirements, detailed models of electric motor, inverter, and energy storage were necessary.

1.2 OBJECTIVE

The main objective of the project was the creation of a MATLAB® Simulink® model of the electric components of a hybrid electric powertrain as it is being used in motorsports. The model had to be capable of operation in real time and also be flexible enough to be used for different powertrain configurations. In addition, the model had to be implemented in the existing simulation software VSM-PTM. In VSM-PTM, the model operates as a standalone software model and as a part of Hardware-in-the-Loop (HiL) simulations.

For this thesis, the focus was on a model for the electric motor and inverter. The result of a prior project within AVL was used as a model for energy storage in a lithium-ion battery.

There are many different modeling approaches with large variations in complexity, computation time, and parameterization effort (Section 2.2). In order for the project to be successful and the result to be useful in the future, it was important to define the appropriate level of complexity of the model. AVL's existing vehicle simulation model was analyzed and the following requirements for the electric drive model were defined.

Since the model was integrated in VSM-PTM, a simulation platform for HiL-simulations, it needed the same real-time capabilities as VSM-PTM. This means the model had to run in Matlab® Simulink® at a frequency of 2 kHz. Additionally, the model needed to be easy to parameterize while maintaining a high level of accuracy. Motorsport applications typically push components to their limits, requiring that the model is accurate in extreme operating conditions. Because manufacturers tend to be secretive about design and control algorithms for the electric drive, the model could not require this information. For the thermal layout of motor and inverter, liquid cooling could be assumed.

Another essential requirement was the representation of the actual physical parameters of the components (i.e. voltages and currents). The electric drive model was later connected to a battery model and therefore needed to have the proper physical interface. Because of the simulation frequency of 2 kHz and the requirement for real time operation, high frequency phenomena were not modeled.

In order to fully integrate into VSM-PTM, the desired model required all necessary interfaces to the surrounding model. The interface components are comprised of coolant temperatures and flow rates for the connection to the vehicle cooling circuit, the battery interface, and the mechanical connection to the drive shaft (Figure 1). Moreover, the model parameters had to be integrated in the PTM parameter structure.

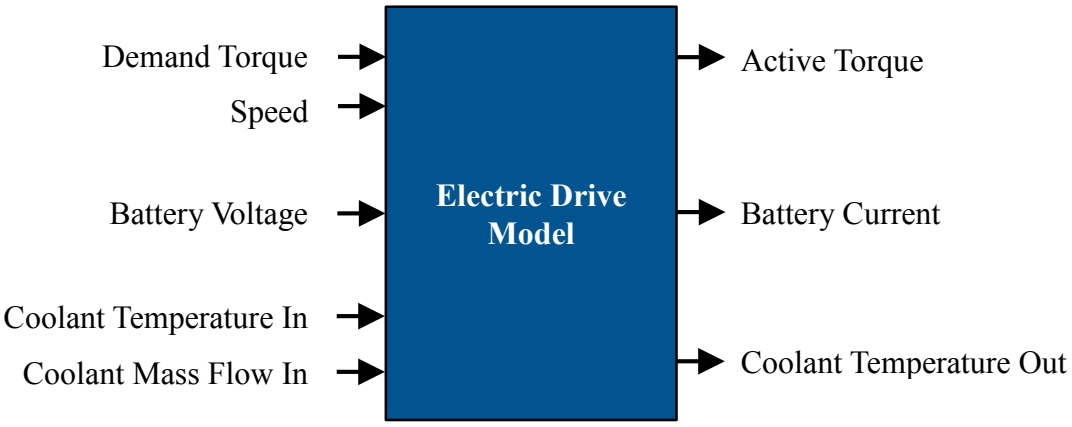

Figure 1: Required model interfaces

To attain a detailed thermal model, the losses of the drive were separated (Figure 2). While the inverter losses are represented in one value, the motor losses are split up into two parts, according to their origin. These three portions of losses are then mapped onto their corresponding nodes in the thermal model (Section 3.1.5 and 3.1.6).

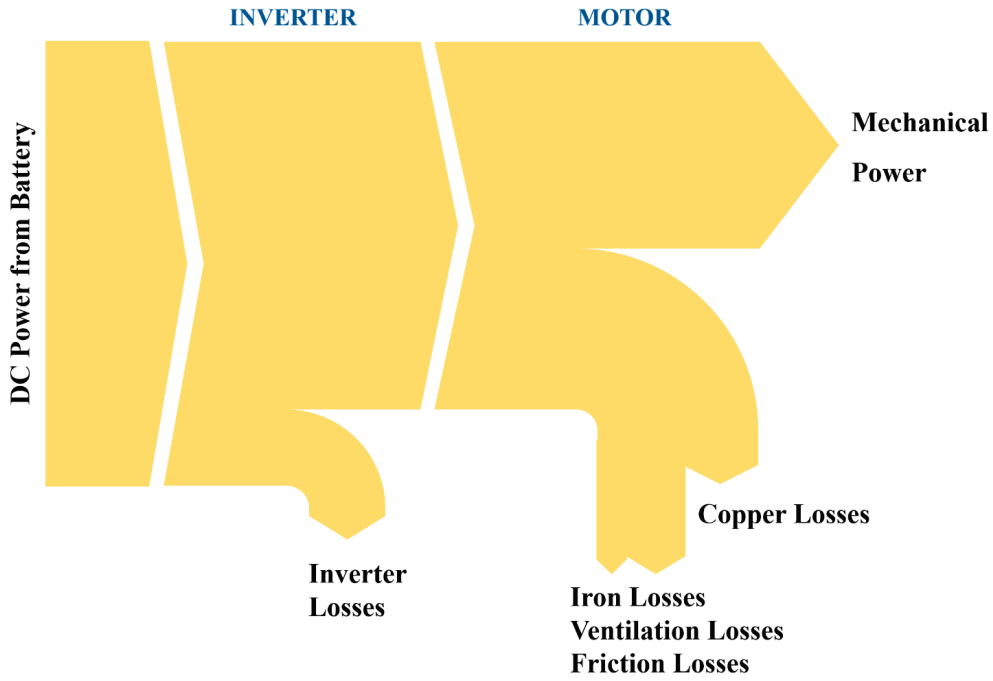

Figure 2: Flow of energy for the electric drive model

2 FUNDAMENTALS

2.1 HYBRID POWERTRAINS IN VEHICLES

Hybrid powertrains in vehicles are one of the most promising concepts to reduce the use of fossil fuels and emissions in traffic. Currently many automotive manufacturers are developing hybrid vehicles (HVs), particularly hybrid electric vehicles (HEVs). The success of established hybrid concepts, like the Toyota Prius, proves not only the ability to decrease fuel consumption and emissions to meet current and future regulations, but also that there is a high demand from consumers.

HVs use more than one source of energy to power the vehicle. Typically, one of those sources works unidirectional (i.e. the energy can only be converted in one direction) (Figure 3, Powertrain (1)). In most cases, this part represents a gasoline or diesel powered ICE. The second source of energy acts not only as a source of power, but also as an energy storage system, harnessing and releasing energy on demand (Figure 3, Powertrain (2)). The most common way of doing that is with electric motors as the energy converter and batteries or super capacitors for the energy storage. Another concept is using a flywheel to store energy, and connect it to the drivetrain through two electric machines or a continuously variable transmission.

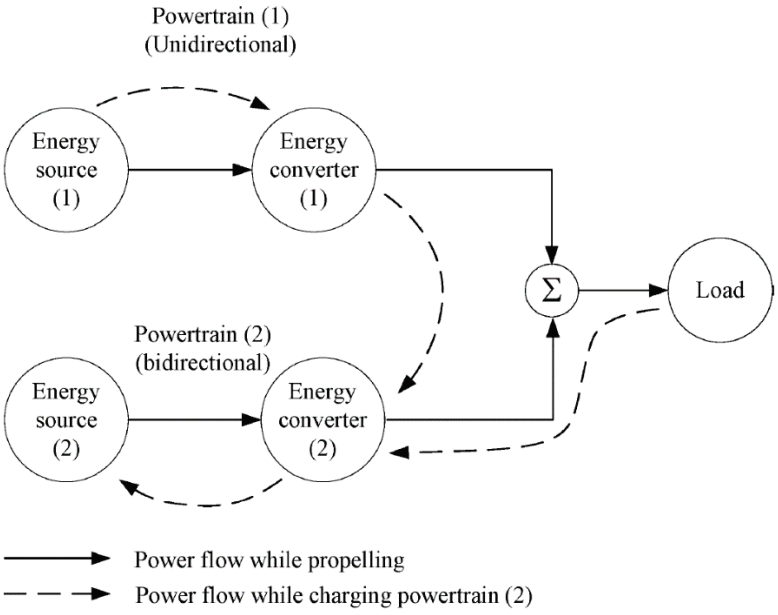

Figure 3: Principal topology of hybrid powertrains [1]

2.1.1 TOPOLOGIES OF HYBRID ELECTRIC POWERTRAINS

As previously mentioned, the vast majority of HVs in series production and development are HEVs, powered by an ICE in combination with electrical energy storage. The most common topologies of such powertrains are introduced in the following sections.

2.1.1.1 PARALLEL HYBRID ELECTRIC POWERTRAIN

In a parallel hybrid electric powertrain configuration, the ICE and the electric motor are both mechanically connected to the wheels and to each other (Figure 4). Several modes of operation are possible:

- Only the ICE delivers power to the transmission
- Only the electric motor delivers power to the transmission
- Both ICE and electric motor deliver power to the transmission
- The electric motor receives power from the transmission (recuperation)
- The electric motor receives power from the ICE
- The electric motor receives power from the transmission and the ICE
- The ICE delivers power to the transmission and the electric motor.

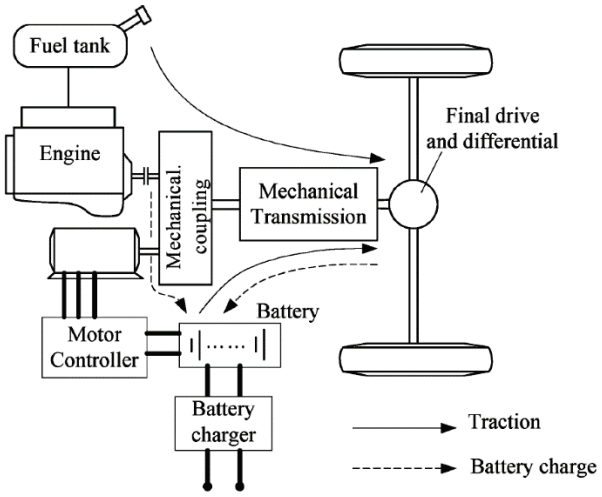

Figure 4: Parallel hybrid electric powertrain [1]

A big advantage of this concept is the ability to deliver torque from both power sources directly to the wheels without any energy conversion, resulting in high transmission efficiency for both the ICE and the electric drive. Another advantage is the scalability of the electric drive. It can be used with small starter-generator units for a start-stop system, as

well as with large electric machines and batteries that offer a substantial range of fully electric driving. The major disadvantage is the inability to drive the ICE in only the most fuel efficient operating point due to the mechanical coupling with the drivetrain [2].

2.1.1.2 SERIES HYBRID ELECTRIC POWERTRAIN

A series hybrid electric powertrain can be seen as a fully electric powertrain with an additional source of electric energy in form of an ICE coupled to a generator (Figure 5). This is the typical layout of electric vehicles with range extenders, where the vehicle is usually powered fully electrically and the ICE is used to extend the range by converting fossil fuels to electricity when the battery is depleted.

Advantages of the series hybrid electric layout include the ability to operate the ICE in a narrow speed range, enabling it to be smaller and more fuel efficient. Also, there is only one source of torque, which reduces the number of mechanical components compared to a parallel layout. Because of the favorable torque-speed characteristics of suitable electric machines, a multi-gear transmission becomes unnecessary. Moreover, packaging is more flexible since most parts of the powertrain are solely connected by electric wires. This concept also bears disadvantages, such as the low overall efficiency of the ICE, due to conversion of mechanical to electrical power and back to mechanical power. The concept requires not only a powerful electric motor for propulsion since it is the only source of mechanical power, but also requires an electric generator to be attached to the ICE [2].

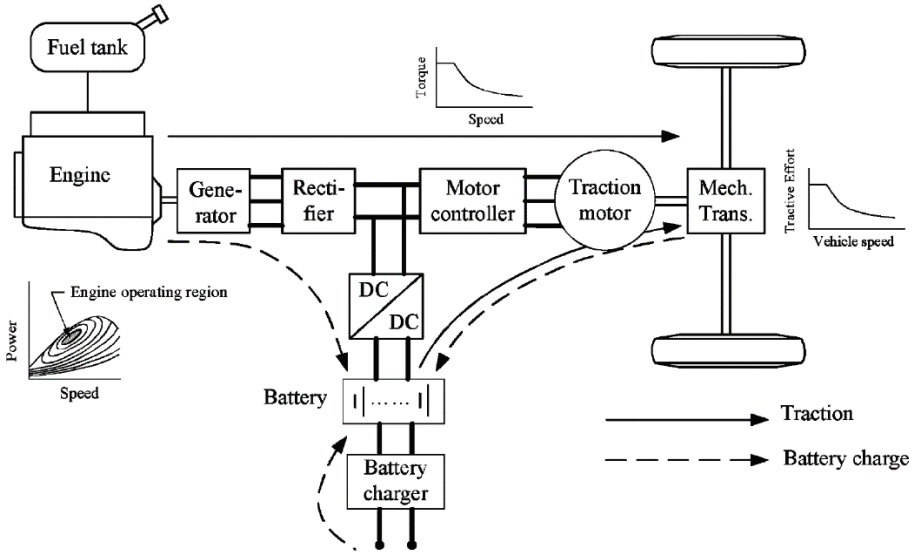

Figure 5: Series hybrid electric powertrain [1]

2.1.1.3 Other Hybrid Electric Powertrain Topologies

Besides the discrete use of series and parallel hybrid electric powertrains, there are also other layouts. One example is a combination of a series and parallel hybrid powertrain, which combines advantages of both layouts. In most operation modes it acts as a regular series hybrid powertrain, allowing fully electric driving with a range extender. However, when maximum power is needed, the ICE can be mechanically connected to the drive shaft using a planetary gearbox or a set of clutches resulting in a higher efficiency at high speeds [1].

2.1.2 Hybrid Powertrains in Motorsports

Saving energy is becoming increasingly important not only for passenger and commercial vehicles but also in motorsports. The following sections give an overview of racing series with hybrid powertrains and their topologies.

2.1.2.1 Formula One

In 2009, Formula One introduced their first hybrid system by adding a kinetic energy recovery system (KERS) to their powertrain. It was a parallel hybrid topology, where an electric or kinetic energy storage was attached to the crank shaft, enabling the KERS to recuperate energy when braking and propelling the car with 60kW for up to 6.6 seconds per lap [3].

In 2014, as a part of major changes in regulations, the Fédération Internationale de l'Automobile (FIA) introduced the Energy Recovery System (ERS), a much more advanced and integrated hybrid concept. It comprises two motor generator units (MGU), one attached to the crankshaft (MGU-K) and one attached to the shaft of the turbo-charger (MGU-H). According to the FIA [4], the MGU-K may operate with an electric power of up to 126kW (~120kW mechanical power) at no more than 50krpm. The MGU-H may run at a maximum of 125krpm but is not limited in power. For energy storage, there is a battery that can provide a maximum of 4MJ of boost energy per lap while being charged at a maximum of 2MJ per lap. Figure 6 illustrates the components of the 2014 F1 power unit.

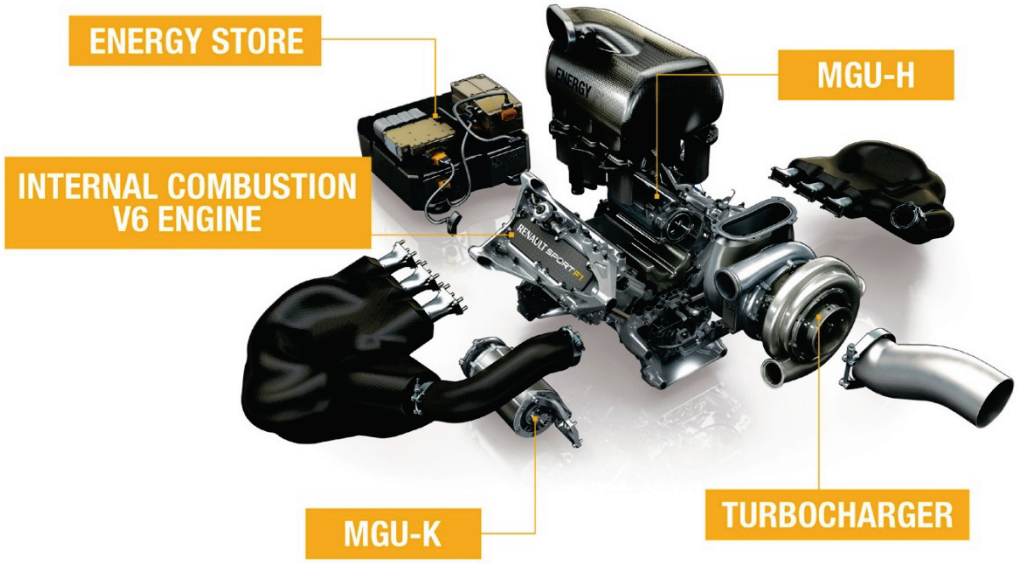

Figure 6: Formula One power unit in 2014 [5]

The 2014 ERS enables a more sustained use of the hybrid components, with twice the power and ten times the storage capacity compared to the preceding KERS. Although more powerful, it also requires more sophisticated controls to coordinate MGU-H, MGU-K, battery and ICE.

2.1.2.2 24 Hours of Le Mans

The Automobile Club de l'Ouest (ACO), host of the 24 Hours of Le Mans, changed the technical regulations in 2009, and again in 2012 and 2014, allowing HVs to enter the race and giving participating teams more freedom in the design of the powertrain. Since then, many variations of hybrid powertrains were used and have proved to be more successful than their ICE powered counterparts. In 2012, the Audi R18 e-tron, equipped with a fly-wheel energy storage system, was the first hybrid car to win the 24 Hours of Le Mans.

2.1.3 Requirements for Hybrid Powertrains in Motorsports

Like most parts in a motorsports vehicle, the requirements for hybrid powertrains are different than those in passenger cars. Important factors for passenger vehicles such as cost, smooth operation, and low noise typically have lower priority in motorsports.

The main goal in racing is to achieve the lowest lap time, which is affected by a large number of vehicle properties. Those most relevant to the powertrain are discussed in the

following sections and are illustrated with results of VSM simulations. The simulations were done with a typical setup for open wheeled single-seater racecars, derived from an existing dataset at AVL Racing. The results show the sensitivity of the system with respect to various parameters. Table 1 gives an overview of important parameters for the simulation, where c_d is the aerodynamic drag coefficient, c_{rr} the per wheel rolling resistance coefficient, m the vehicle mass, P_{PU} the overall power of the power unit and η_{PU} the overall efficiency of the power unit.

Table 1: Vehicle parameters for simulations

c_d	c_{rr}	m	P_{PU}	η_{PU}
-	-	kg	kW	%
0.952	0.018	695	445	35

The track used in the simulations was the Autodromo Nazionale Monza in Italy (Figure 53, page 59) with a length of 5,754 meters. Figure 7 shows the vehicle speed profile of the simulation with the parameters from Table 1, resulting in a lap time of 92.87s.

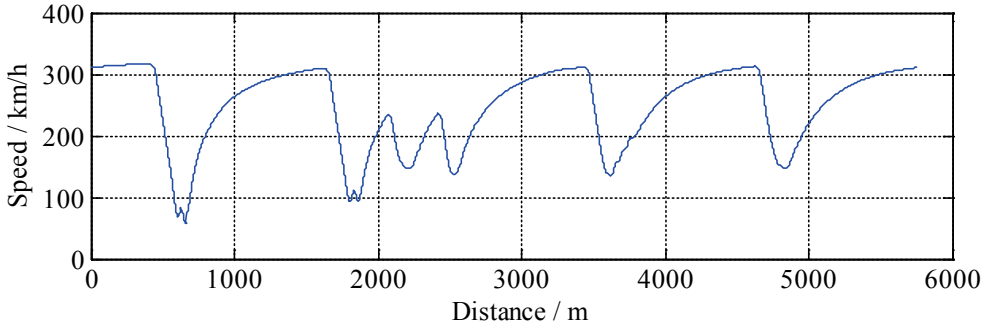

Figure 7: Vehicle speed at the Autodromo Nazionale Monza, simulation result

2.1.3.1 POWER

The most obvious factor for a quick lap is the overall power of the hybrid power unit. The higher the propulsion power, the faster the car and therefore the lower the lap time. The result of VSM simulations with different ICE power is shown in Figure 8. Although the lap time decreases with higher power, the graph also indicates that the improvement is not proportional to the power gain. This is because of the increasing aerodynamic drag at higher vehicle speeds. In addition, the duration of full power during a lap decreases with increased maximum power since the tires are operated at the slip limit for a longer time.

Consequences of a change in ICE power (e.g. from increased vehicle weight, higher fuel consumption) have been ignored in these simulations.

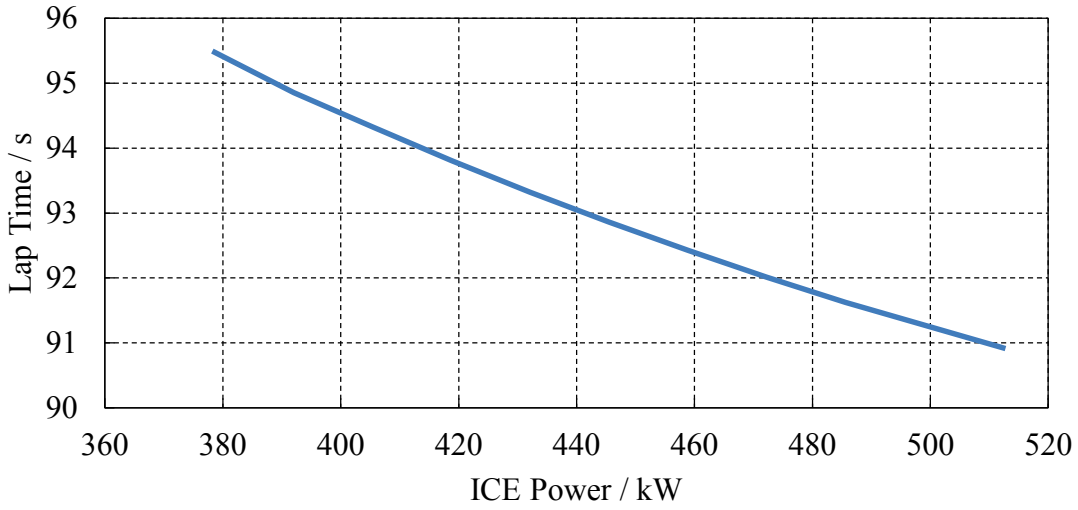

Figure 8: Influence of propulsion power on lap time

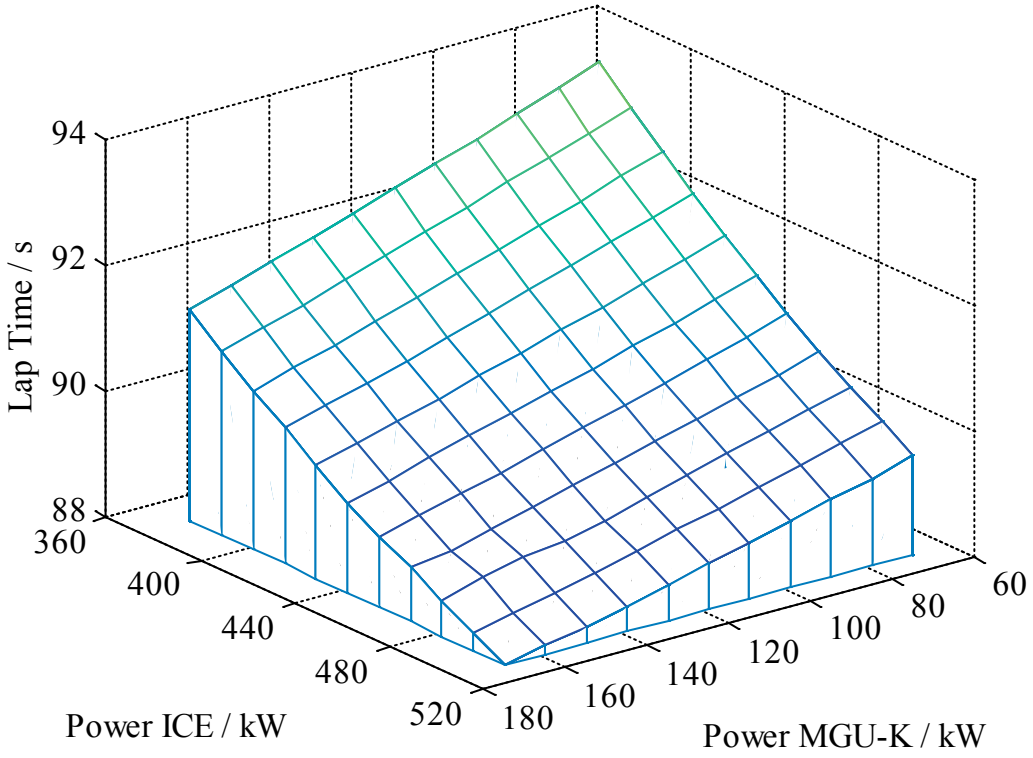

Figure 9: Influence of ICE power and MGU-K power on lap time

In a parallel hybrid configuration like in Formula One, it is worth considering how powerful combustion engines and electric motors should be. Figure 9 illustrates the effect of ICE power and MGU-K power on lap time. In this example, the MGU-K always operates

when the ICE is at full load, without considering the MGU-K's energy limits. It shows that an increase of the MGU-K's power by 100kW gains 1.5s in lap time, while the same increase of power for the combustion engine gains about 2.5s.

Since the power of the MGU-K is limited to a maximum of 120kW, the ICE is the only device that can be worked on with the current regulations. There is also a limitation of fuel consumption to 100kg per race and fuel mass flow to no more than 100kg/h at any time [4]. As a result, the efficiency of the combustion engine is a very crucial part for success, and a lot of engineering effort is put into its optimization.

2.1.3.2 VEHICLE WEIGHT

To illustrate the effects of vehicle weight, Figure 10 shows VSM simulation results at different vehicle weights. All other parameters remained constant. Since mass affects the acceleration of the vehicle, higher mass at a constant engine power leads to a linear increase in lap time.

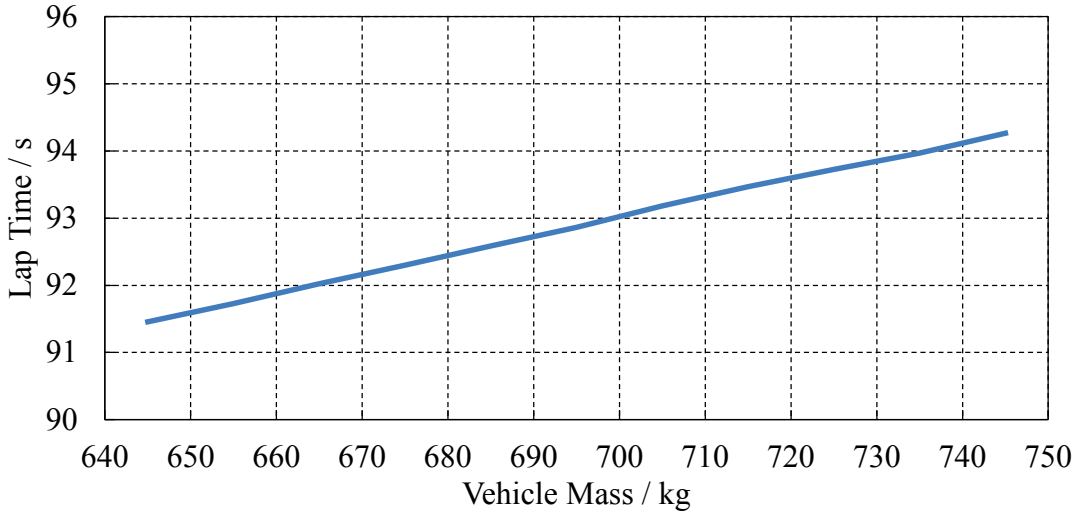

Figure 10: Influence of vehicle mass on lap time

2.1.3.3 AERODYNAMIC PERFORMANCE

Another very important contributor to lower lap times in modern motorsports is the aerodynamic behavior of the car. While higher downforce improves the car's traction limit, allowing for higher cornering speeds, it has negative effects on the drag coefficient. Consequently, the maximum speed is reduced. Figure 11 shows simulation results of different

aerodynamic drag on the car's lap time. All other parameters, including downforce, were kept constant.

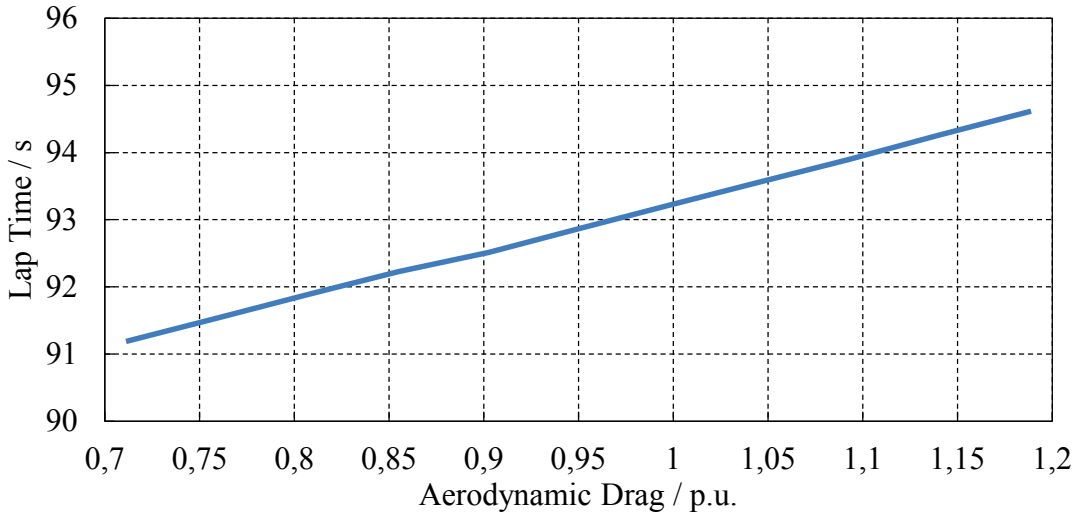

Figure 11: Influence of aerodynamic drag on lap time

2.1.3.4 EFFICIENCY

The efficiency of the power unit gained in importance particularly after some of the biggest race classes passed regulations to limit fuel consumption. When fuel consumption is limited, every improvement in efficiency directly affects the lap time. Figure 12 shows the lap time over different power unit efficiencies. Similar to the effect of propulsion power (Figure 8), the lap time gain decreases at higher efficiencies since the additional power can only be used when the wheels are below the slip limit.

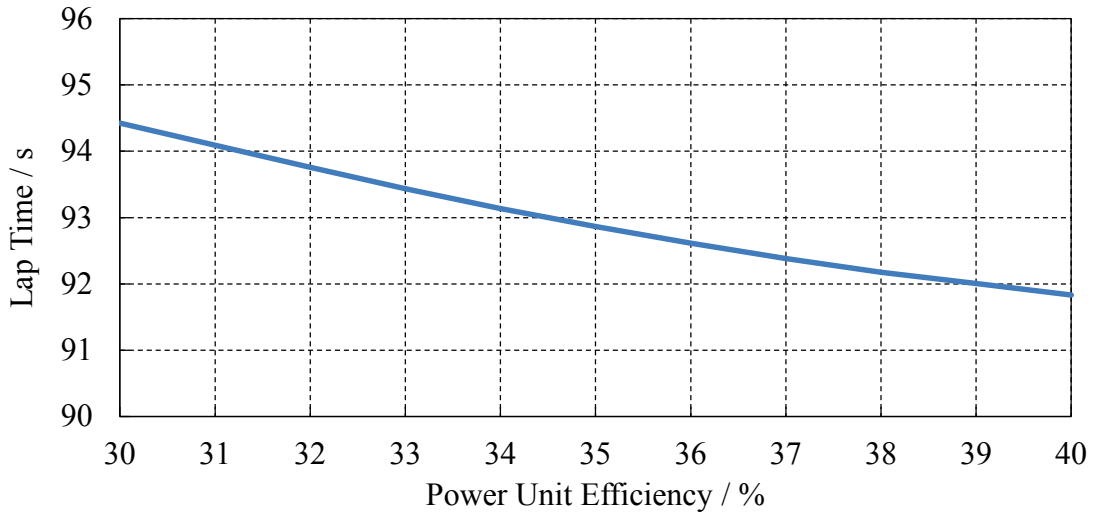

Figure 12: Influence of power unit efficiency on lap time

Another aspect of efficiency is when to use the available energy over the course of a lap. Figure 13 shows the relationship of energy and MGU-K power and their influence on lap time. It turns out that with the same amount of energy per lap, different lap times can be obtained. The more concentrated the boost of the MGU-K at the beginning of each straight (i.e. the higher the MGU-K power), the lower the overall lap time.

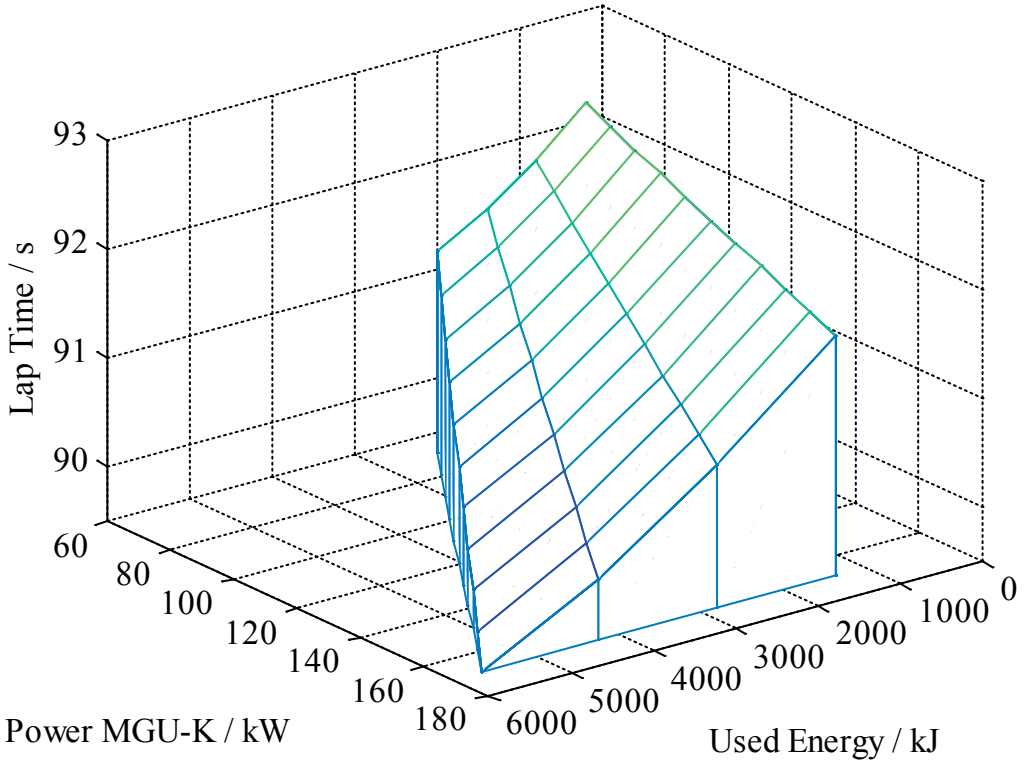

Figure 13: Influence of MGU-K power and used energy on lap time

2.2 MODELING OF ELECTRIC DRIVES

Describing the behavior of electric drives has been a topic of interest for decades, and is still an ongoing field of research. The following sections will discuss some of the most popular ways of modeling electric drives, both for the electromagnetic and the thermal domain.

2.2.1 BASICS OF ELECTRIC DRIVES

Traditionally, electric motors run uncontrolled, directly fed from the electric grid. Thus, there is typically only one rotational speed at which they can continuously operate. It is determined by the winding configuration of the motor and therefore cannot be changed without major modification of the motor. By using a power processing unit (PPU), also

referred to as inverter, and appropriate controls, the electric motor can be decoupled from the electric power source. This enables it to run within a range of speeds rather than at a single speed. An electric drive system typically consists of a motor, the PPU, a sensor for the motor's rotor position and the controller [6]. Some drives, particularly induction motor (IM) drives, do not always require a sensor for the rotor position or speed. Figure 14 illustrates a typical drive system including the source of electricity and the mechanical load.

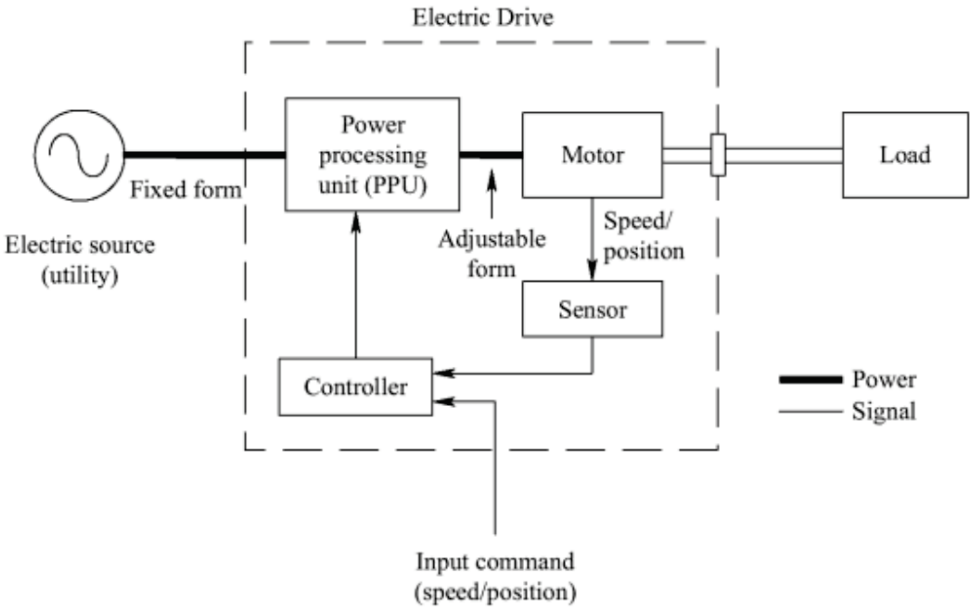

Figure 14: Block Diagram of a typical Electric Drive System [7]

The main part of the PPU is a set of semiconductors that converts the fixed form of electricity (Figure 14) to the desired form for driving the motor. In traction applications, the fixed form is typically direct current (DC) voltage from a battery. The most crucial part of an electric drive is the controller, which generates the demanded waveform for the inverter by evaluating the input command and the rotor position.

Another significant advantage allowing for the use of electric motors in traction applications is the ability to not only drive a motor at positive and negative rotational speeds, but also apply positive and negative torques. This results in the so-called four-quadrant operation shown in Figure 15.

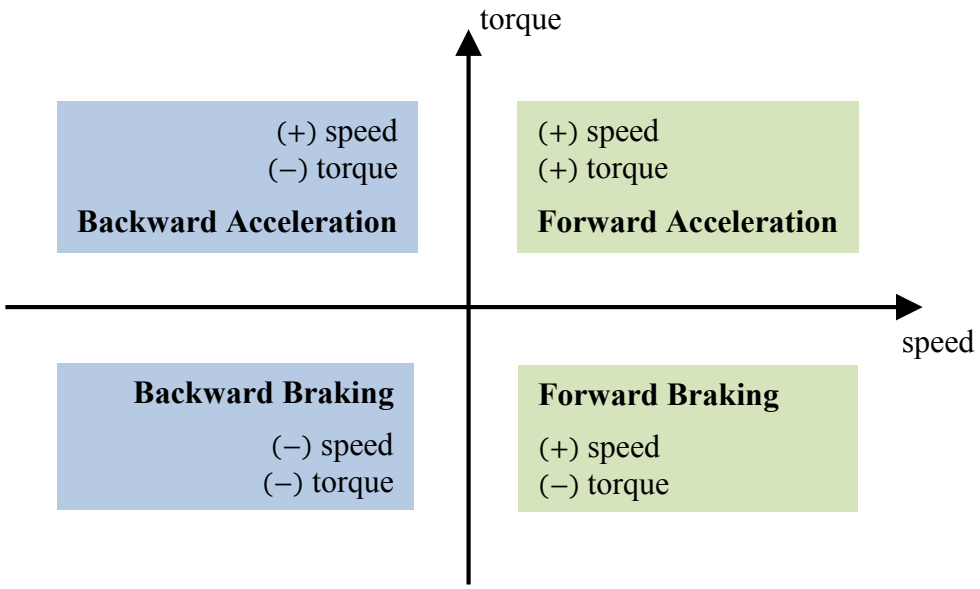

Figure 15: Four-quadrant operation of electric drives in vehicles

Inverters can be used to drive most types of electric motors. The most common types used in vehicles for propulsion purposes are IMs, interior permanent magnet synchronous motors (IPM), and surface mounted permanent magnet synchronous motors (SPM) [8, 9, 10]. Details about the functionality of these machines can be found in [6, 11] and other literature about fundamentals of electric machinery.

2.2.2 Electromechanical Behavior of Electrical Machines

There is a variety of approaches to modeling electric machines which greatly differ in complexity and accuracy. The choices for a given model have to be made according to the desired level of detail and available data for parameterization of the model. For the following models discussed in this section, permanent magnet synchronous motors were used. However, the introduced models can be used for most common types of electric machines.

Independent of the chosen model, there are several basic relations for symmetric three phase electric machines that are used in this thesis [6]. The active power fed into a three phase electric machine can be calculated as

$$P_{el} = 3 \cdot I_S \cdot U_S \cdot cos\varphi, \tag{2.1}$$

with I_S and U_S as the stator current and voltage, respectively, and $cos\varphi$ as the power factor of the machine. The mechanical power on the rotor shaft of the machine is calculated as

$$P_{mech} = T \cdot \omega, \tag{2.2}$$

where T is the mechanical torque and ω is the angular velocity of the rotor. By combining Equation (2.1) and (2.2) the overall efficiency η of the machine can be obtained as follows:

$$\eta = \frac{P_{mech}}{P_{el}}. \tag{2.3}$$

2.2.2.1 Equivalent Circuit

A simple way of describing the behavior of electric machines is to derive equivalent electric circuits, which represent more complex physical processes taking place inside the machine. Figure 16 shows the single phase equivalent circuit of a permanent magnet synchronous machine, with R_1 as the stator resistance, L_1 as the stator inductance, U_T as the terminal voltage, I_1 as the stator current and U_{PM} as the induced voltage due to the permanent magnets in the rotor.

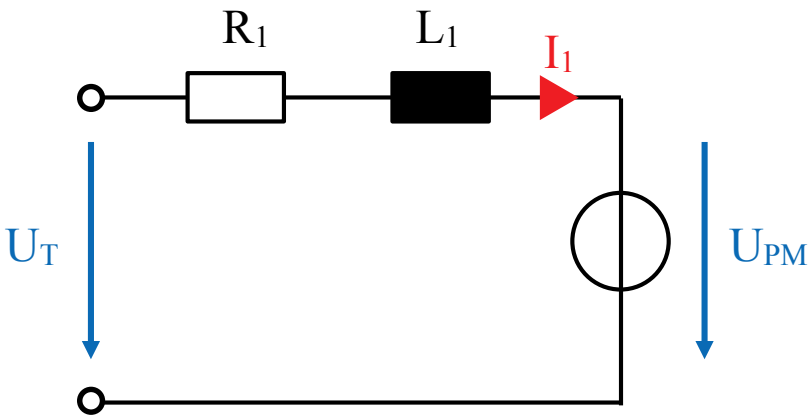

Figure 16: Single-phase equivalent circuit of a SPM

Single phase equivalent circuits are a good base for modeling and understanding the functionality of electric machines and are rapidly simulated. However, they only describe the basic behavior of the machine and do not account for magnetic saturation, geometric

asymmetries or frequencies of higher order. Furthermore, there is no simple mathematical connection between the electrical input and the mechanical output of the machine.

2.2.2.2 SPACE VECTOR MODEL

For three-phase-systems, the space-vector representation is the most commonly used approach today. It is based on the fact that the sum of the three phase voltages, currents, etc., in a symmetric three-phase-system without a neutral conductor is always zero. Equation (2.4) clarifies this relationship for the stator phase voltages as follows,

$$U_a + U_b + U_c = 0. \tag{2.4}$$

One phase value can be calculated from the two other phases, so it is sufficient to know the values of two phases to define the system. The relationship can also be described with a system of two vectors using a Cartesian coordinate system. This is called dq-, or Park-Transformation, and will be explained in the following paragraphs using the stator currents as an example. In general, the phase currents of a three-phase system can be described as

$$\begin{aligned} i_a &= \hat{I} \cdot \cos(\omega t + \varphi_a) = \hat{I} \cdot e^{j\varphi_a}, \\ i_b &= \hat{I} \cdot \cos(\omega t + \varphi_b) = \hat{I} \cdot e^{j\varphi_b}, \\ i_c &= \hat{I} \cdot \cos(\omega t + \varphi_c) = \hat{I} \cdot e^{j\varphi_c}, \end{aligned} \tag{2.5}$$

where $\varphi_a = 0,\ \varphi_b = \frac{2\pi}{3}$, and $\varphi_c = \frac{4\pi}{3}$ correspond to the 120° temporal shift between the phases. In a three-phase electric motor, the phases also have a 120° physical gap with respect to each other (see Figure 17a), which, when adding them geometrically, results in a constant magnitude vector rotating with the angular frequency ω. The idea of the Park-Transformation is to define a coordinate system that rotates with the same frequency ω, creating a domain where the physical three-phase system is represented through non-rotating DC-vectors. Equation (2.6) shows the transformation proposed by Park [12].

$$\begin{bmatrix} i_d \\ i_q \end{bmatrix} = \frac{2}{3} \begin{bmatrix} \cos(\theta) & \cos\left(\theta - \frac{2\pi}{3}\right) & \cos\left(\theta + \frac{2\pi}{3}\right) \\ -\sin(\theta) & -\sin\left(\theta - \frac{2\pi}{3}\right) & -\sin\left(\theta + \frac{2\pi}{3}\right) \end{bmatrix} \cdot \begin{bmatrix} i_a \\ i_b \\ i_c \end{bmatrix} \tag{2.6}$$

For most types of electric machines (except induction machines), θ is the angular position of the rotor. Figure 17 illustrates the transition from the physical three-phase system to the imaginary two-phase Cartesian system.

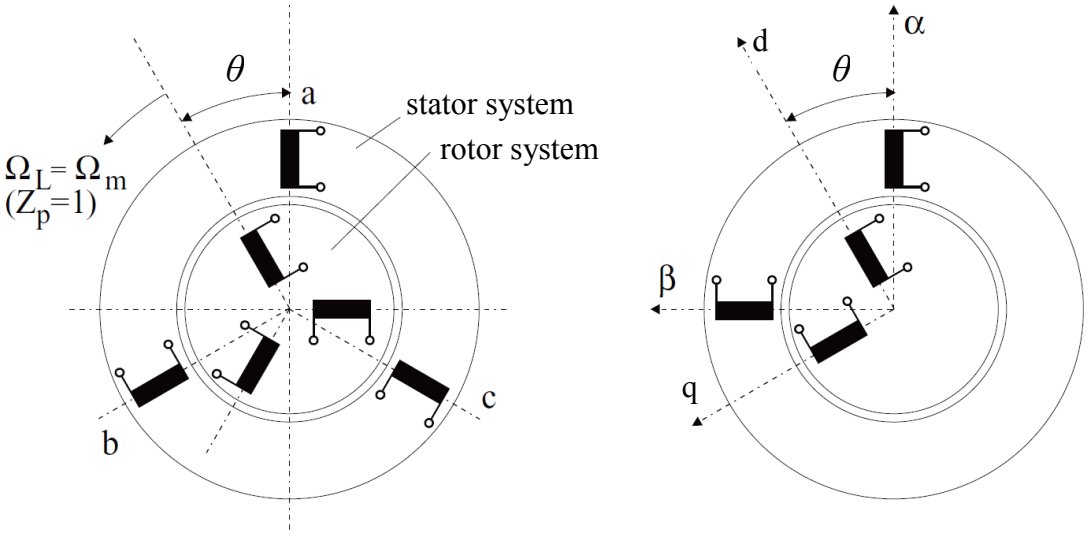

(a) three-phase system (b) two-phase Cartesian system

Figure 17: Transition from three-phase to two-phase system [6]

A major advantage of this approach is that the connection between the electrical and mechanical behavior of the machine can be written in a simple way [13]. The air gap torque for SPM machines is given by

$$T = \frac{3}{2}\, p \cdot \Psi_{PM} \cdot i_q, \tag{2.7}$$

where p is the number of pole pairs, Ψ_{PM} is the flux linkage due to the permanent magnets in the rotor, and i_q is the current in the q-axis. Considering the reluctance torque of IPM machines, the air gap torque expands Equation (2.7) to

$$T = \frac{3}{2}\, p \left(\Psi_{PM} \cdot i_q + \left(L_d - L_q\right) \cdot i_d \cdot i_q\right), \tag{2.8}$$

where L_d and L_q are the inductances in d- and q-axis. Equations (2.7) and (2.8) are the basis of the field oriented control method used in many modern electric drive applications.

2.2.2.3 FINITE ELEMENT ANALYSIS (FEA)

The finite element method has become more popular in recent decades, partly due to the increasing computational power of computers. In contrast to the approaches discussed in Sections 2.2.2.1 and 2.2.2.2, it focuses on the spatial electromagnetic field distribution in the machine (i.e. it stays close to the actual physical phenomena). The finite element method is used in several fields of engineering and is not limited to electromagnetic fields. Because the electromagnetic FEA is the only relevant application for this thesis, the others are not discussed in detail.

The basic idea of electromagnetic FEA is to solve the underlying set of partial differential equations (Maxwell's equations) for a particular problem. The Maxwell's equations are as follows:

$$\begin{aligned} \nabla \cdot \boldsymbol{E} &= \frac{\rho}{\varepsilon_0}, \\ \nabla \cdot \boldsymbol{B} &= 0, \\ \nabla \times \boldsymbol{E} &= -\frac{\partial \boldsymbol{B}}{\partial t}, \\ \text{and } \nabla \times \boldsymbol{B} &= \mu_0 \left(\boldsymbol{J} + \varepsilon_0 \frac{\partial \boldsymbol{E}}{\partial t} \right). \end{aligned} \tag{2.9}$$

Analytical solutions of these equations can only be obtained for simple problems. In order to solve them for more complex problems, the problem is divided into a large number of simpler elements. These elements are solved numerically and are reassembled to form the solution of the initial problem. Figure 18 shows the discretization of a 2D SPM problem into triangular elements, done with the FEA software JMAG.

Since this is a numeric approach, the solution will never be exact, but the accuracy increases as the number of elements grows. This also increases the computation time, so there is a trade-off between accuracy and necessary computational power or time. Therefore, many FEA models for electrical machines are two-dimensional, simulating only one radial plane of the machine. If there are symmetries in that radial plane, the FEA model may also simulate only parts of that radial plane. Consequently, the model size of FEA problems varies greatly, from some thousands of elements (e.g. 2D quarter models) to

several millions of elements (e.g. full 3D models). Because the finite element method is based on the spatial distribution of fields, the geometry of the machine as well as material parameters, like magnetic saturation, are taken into account. FEA models are not limited to symmetric electrical machines, but able to solve various electromagnetic problems.

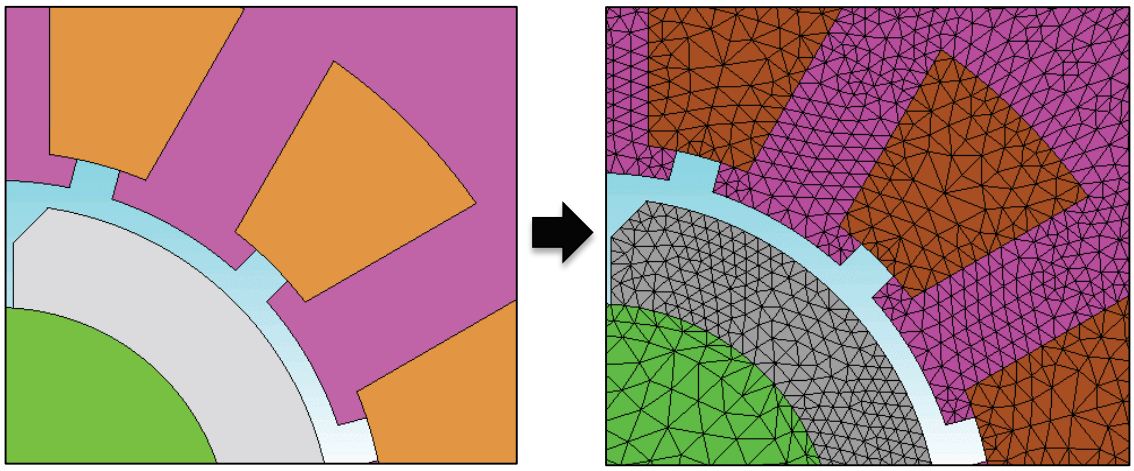

Figure 18: Division into finite elements for a 2D SPM problem

2.2.3 Determination of Losses in Electrical Machines

Particularly for electrical drives in vehicles, high efficiency is of great importance. In order to calculate the efficiency in a model, the losses that occur in various parts of the machine need to be determined. Those can be divided into four main contributors as follows:

$$P_L = P_{cu} + P_{fe} + P_{fr} + P_v. \tag{2.10}$$

The majority of losses occur in the winding (P_{cu}) and the iron core (P_{fe}). Additional losses can be defined as friction losses (P_{fr}) and ventilation losses (P_v). In the following sections, the causes and various modeling approaches for these types of losses will be introduced.

2.2.3.1 Copper Losses

Copper losses occur in the stator winding and are also referred to as ohmic or winding losses. They are caused by the ohmic resistance of the stator windings, typically made of copper, and the current flowing through these windings. For three phase machines, the basic calculation is done by

$$P_{cu} = 3 \cdot I_S^2 \cdot R_S, \tag{2.11}$$

where I_S is the root mean square (RMS) value of the current through one phase, and R_S is the mean resistance of one phase winding. Since the resistance of copper varies with temperature, R_S is not constant. The thermal behavior of the resistance of copper can be approximated by

$$R(T) = R(T_0) \cdot \big(1 + \alpha_{cu} \cdot (T - T_0)\big), \tag{2.12}$$

with $R(T_0)$ as the resistance at a reference temperature T_0 and α_{cu} as the temperature coefficient of copper. For commercial copper used in electric machines, the temperature coefficient is $\alpha_{cu} = 3{,}81 \cdot 10^{-3}\ K^{-1}$ [14].

2.2.3.2 Iron Losses

Iron losses occur in the magnetic parts of rotor and stator and are also referred to as core losses or magnetic losses. The losses are caused by the alternating magnetic field and can be divided into two separate phenomena: hysteresis losses and eddy current losses.

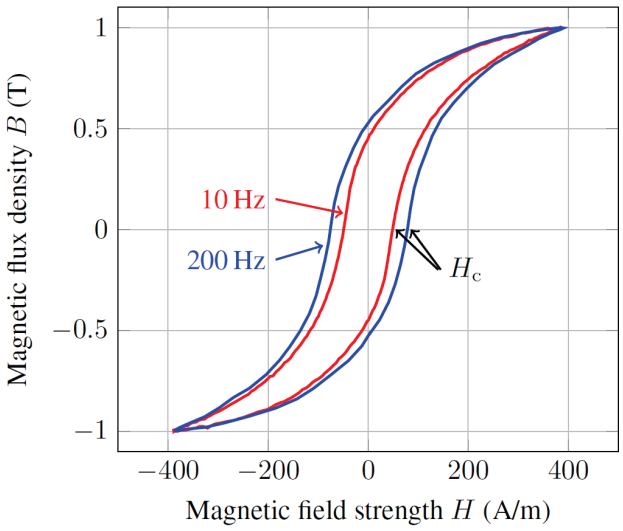

Figure 19: B-H hysteresis curve of a ferromagnetic material at 10Hz (red) and 200Hz (blue) [15]

Hysteresis losses occur due to the nonlinear behavior of ferromagnetic materials. If a ferromagnetic material is exposed to a magnetic field H in one direction, which then declines and changes to the opposite direction, the resulting magnetic field density B does not

follow linearly. Due to the reorientation of the Weiss domains in the material [6], the transition from a positive to negative magnetic field and vice versa follows a hysteresis loop (Figure 19). The area enclosed by the hysteresis loop represents the specific energy for each cycle, which is proportional to the iron losses. The specific iron losses at a frequency f of the magnetic field H can be calculated with

$$p_{fe} = f \oint H \, dB. \tag{2.13}$$

Eddy current losses, or joule losses, are caused by the eddy currents in the conductive regions of the machine due to the alternating magnetic field and, consequently, the induced voltage. They are divided into classic and anomalous eddy current losses. Classic eddy current losses originate from the induced voltage, causing circular currents in the stack of iron sheets, which lead to losses due to the ohmic resistance of the iron. The anomalous losses refer to losses from microscopic eddy currents caused by the displacement of the Bloch walls [16]. There are numerous ways of mathematically describing iron losses in electrical machines. Figure 20 gives an overview of common approaches.

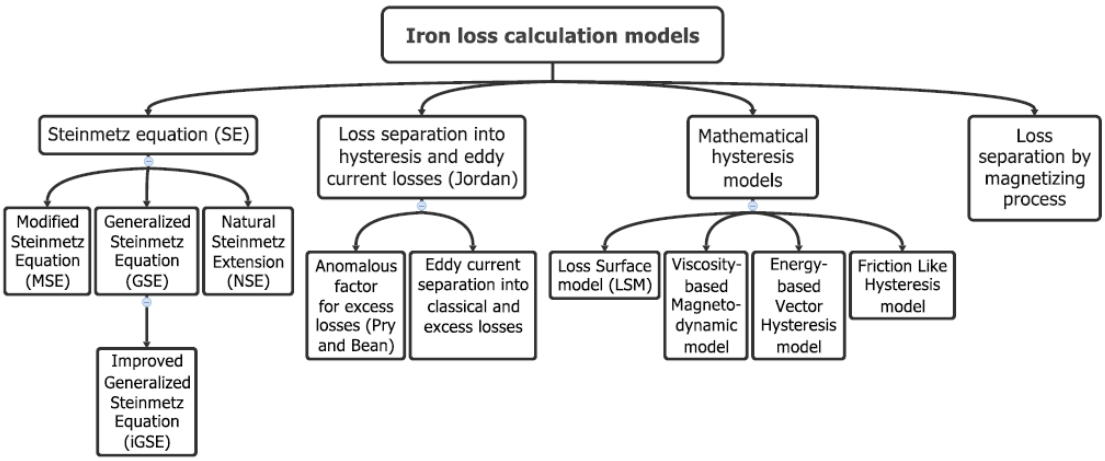

Figure 20: Different approaches for modeling the iron losses in electric machines [15]

2.2.3.3 MECHANICAL LOSSES

Mechanical losses occur due to the rotation of the motor's shaft. The majority of those losses are friction losses in the rotor bearings and ventilation losses in the air gap. In electric machines with permanent magnets, the mechanical losses cannot be measured separately because of the ever present iron losses. The permanent magnets would have to be removed to do the measurements.

2.2.4 THERMAL LUMPED PARAMETER MODEL

In order to account for the influence of temperature on the operation of an electric drive system and to design an adequate cooling circuit, the thermal behavior of the machine needs to be modelled. Since other thermal modelling approaches such as thermal finite element modelling or computational fluid dynamics would not meet the model requirement for real time capability, the concept of lumped parameters is the only approach discussed in detail.

A lumped parameter model, also called lumped element model or lumped capacitance model, reduces a thermal system to a number of interconnected discrete points. This simplifies the partial differential equations of the continuous time and space model of the physical system to a finite set of ordinary differential equations. It is analogous to the equivalent circuit approach used for electrical networks (Figure 21).

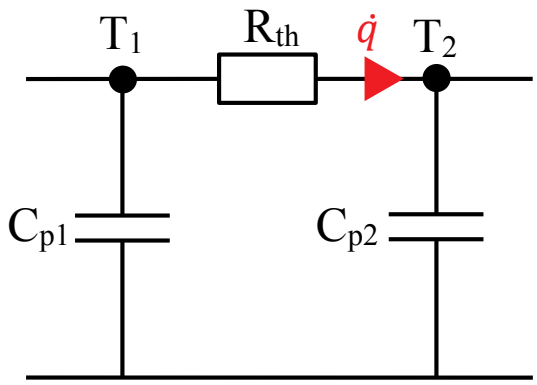

Figure 21: Example lumped parameter network

According to Fourier's law of thermal conduction, the local heat flux density can be calculated as the product of thermal conductivity λ and the negative local temperature gradient $-\nabla T$ as follows:

$$\vec{q} = -\lambda \nabla T. \tag{2.14}$$

Making the assumptions used for lumped element models, this can be simplified to

$$\dot{q} = \frac{\Delta T}{R_{th}} = \frac{T_1 - T_2}{R_{th}}, \tag{2.15}$$

where ΔT is the temperature difference between two nodes, and R_{th} is the thermal resistance between them. This is analogous to Ohm's Law for electrical circuits. The temperature of each mass point can be obtained by

$$T = \frac{1}{m \cdot C_p} \int (P_L - \dot{q}) dt + T_0, \tag{2.16}$$

with m being the mass of the particular lump, C_p the specific heat, P_L the rate of heat transfer to the lump, $\dot{q}$ the rate of heat transfer from the lump, and T_0 the initial temperature. The size of lumped element models can range from one or two lumps to massive, auto-generated models with a large number of elements.

3 METHODOLOGY

After covering the technical background for the thesis, the following sections explain the model that was designed and the assumptions it is based on.

3.1 DESIGN OF THE ELECTRIC DRIVE MODEL

According to the model requirements stated in Section 1.2, a modelling approach for the physical parts of the model was proposed. Figure 22 gives an overview of the organization of the different parts.

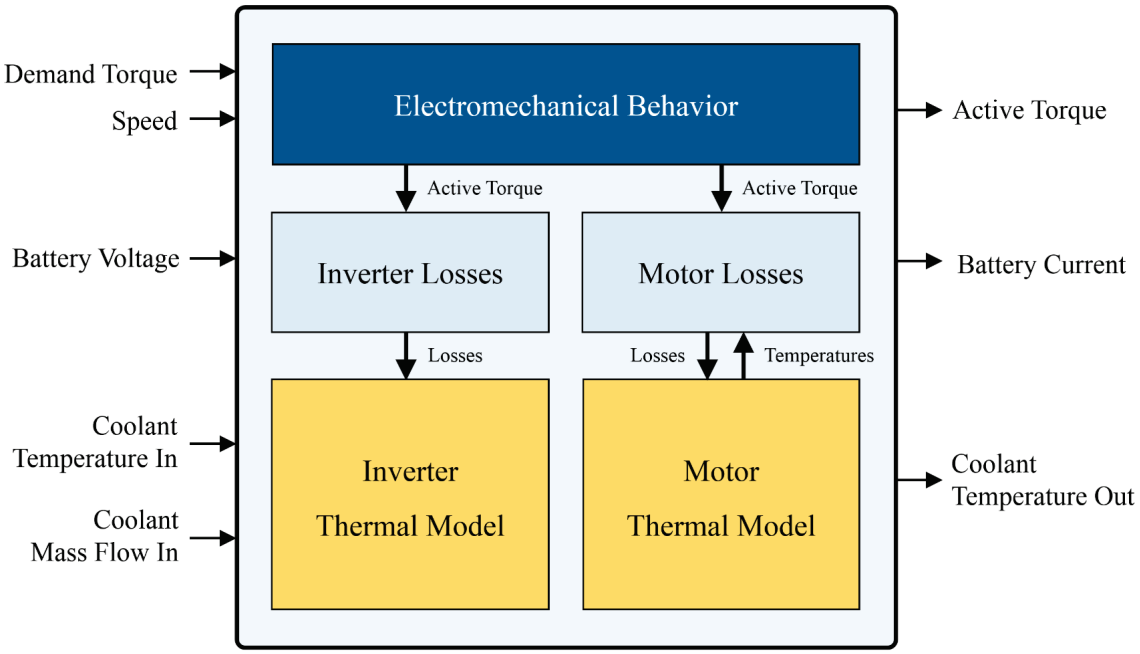

Figure 22: Electric drive model layout

The model consists of a basic representation of the electromechanical behavior, loss calculations for both inverter and motor, and the thermal models for inverter and motor.

3.1.1 ELECTROMECHANICAL BEHAVIOR

As mentioned in Section 1.2, the model could not require knowledge about the controls of the electric motor, and thus a space vector based approach was not feasible. For the same reason and the required real-time capabilities, any finite element modelling would not have met the requirements either. Consequently, the model for the electromechanical behavior simply comprises a time delay to account for the delay in torque production and

a limitation of maximum torque according to the motor speed and DC supply voltage. Figure 23 illustrates the modelling approach.

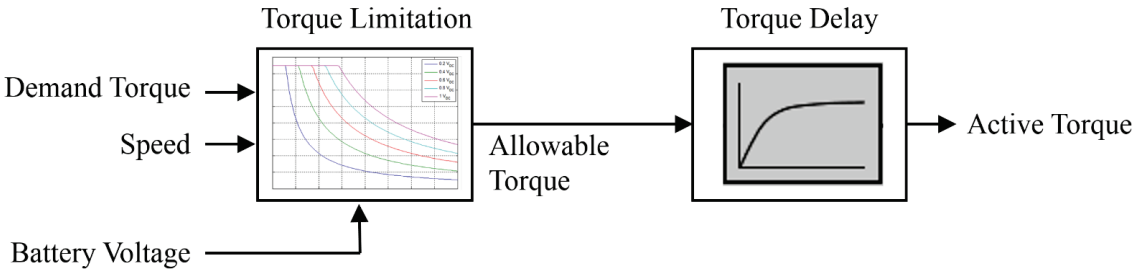

Figure 23: Modelling approach for the electromechanical behavior

The torque limitation block ensures that the produced torque never exceeds the motors maximum rating at a certain speed, and also reduces the maximum rating if the supply voltage drops below a critical value. Figure 24 illustrates the derating of motor torque when the supply voltage drops under a critical value V_{DC}, which results in a lower base speed (i.e. an earlier start of field weakening operation).

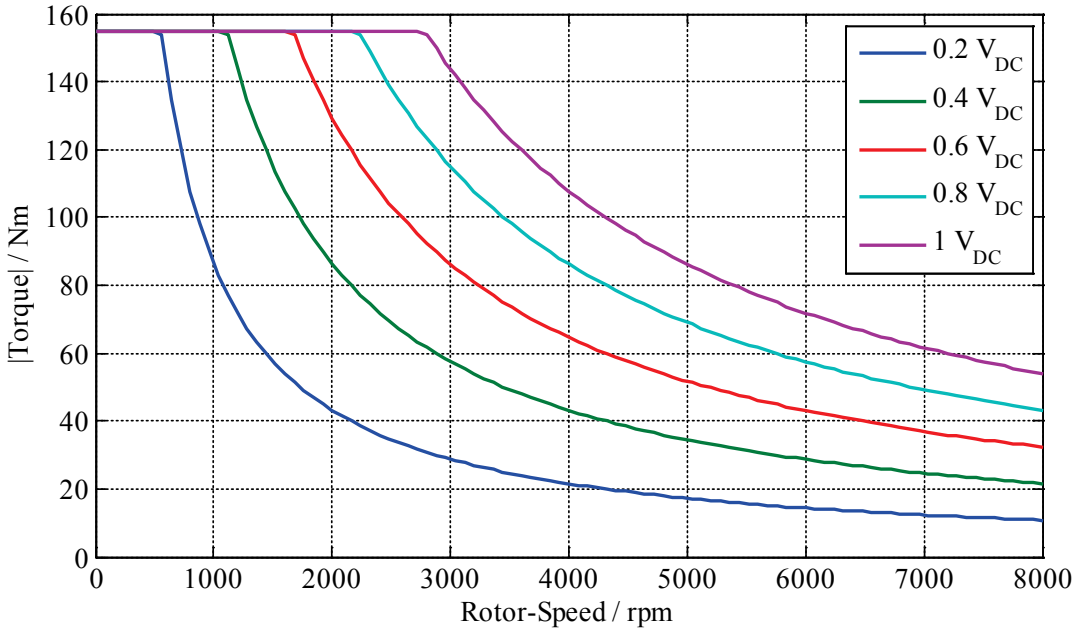

Figure 24: Motor torque derating due to low supply voltage

The motor's torque response can be represented with a first order lag element. The according mathematical form is

$$T = T_{dem} \cdot \left(1 - e^{-\frac{t}{\tau}}\right), \tag{3.1}$$

where T_{dem} is the demanded torque and τ is the torque delay time constant. Figure 25 shows the resulting model layout as it was implemented in Simulink. The go-to flags for speed and torque were used as inputs for the following loss determination.

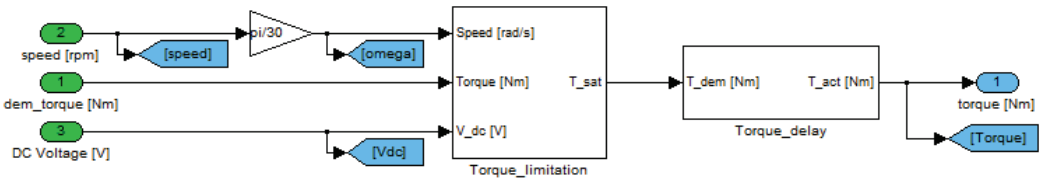

Figure 25: Simulink model for electromechanical behavior

3.1.2 Motor Losses

In order to model the thermal behavior of the electric drivetrain, the losses needed to be determined. In accordance with the model requirements (Section 1.2), the losses were estimated based on measurements of the motor efficiency over the whole operating range, including the temperature of the winding. The model distinguishes between copper losses and other losses, including iron, friction and ventilation losses. Since the major application for this model will be permanent magnet motors, where iron, friction, and ventilation losses are hard to measure separately, no further separation was made.

The copper losses are determined by

$$P_{cu} = N_{ph} \cdot I_{ph}^2 \cdot R_S, \tag{3.2}$$

where I_{ph} is the measured mean RMS phase current at each operating point, R_S the mean stator winding resistance at the current winding temperature, and N_{Ph} is the number of phases. The stator winding resistance was calculated with the following equation based on a measurement of the mean stator winding resistance at a known temperature, and the current winding temperature,

$$R_S(T) = R_S(T_0) \cdot \left(1 + \alpha_{cu} \cdot (T - T_0)\right). \tag{3.3}$$

Here, T_0 is the temperature where the mean stator winding phase resistance $R_S(T_0)$ was measured and α_{cu} is the temperature coefficient of copper. Figure 26 illustrates the proposed model layout for the determination of copper losses.

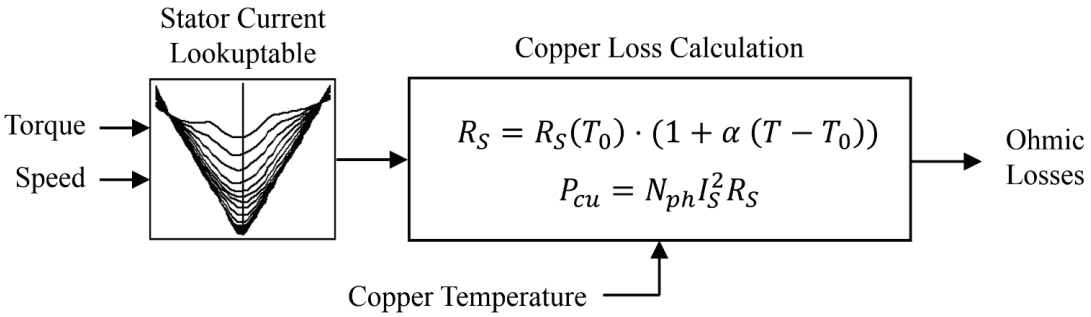

Figure 26: Modelling approach for the copper losses

Since the iron, friction and ventilation losses are not separated, there is no way to analytically describe the influence of temperature. Consequently, the temperature dependence of these losses was implemented as an additional parameter for the losses lookup table based on efficiency measurements at different motor temperatures. Considering the model requirements, this was a very accurate way of determining these losses. Figure 27 illustrates this model layout.

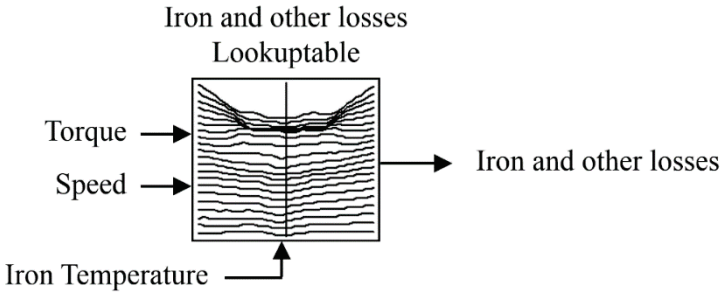

Figure 27: Modelling approach for iron and other losses

The determination of all motor losses implemented in Simulink is shown in Figure 28.

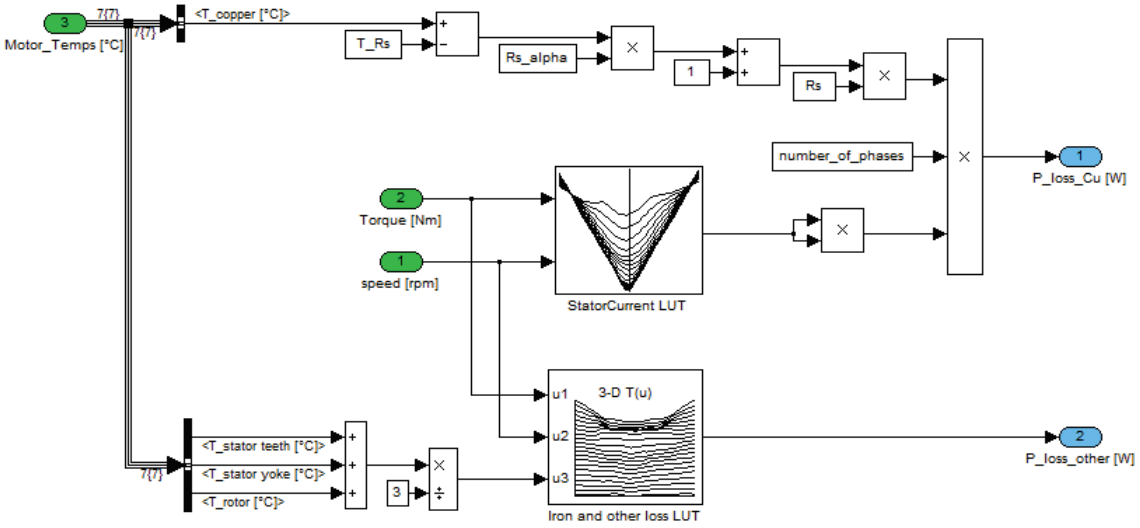

Figure 28: Simulink model for determination of motor losses

3.1.3 Inverter Losses

Since there is little to no knowledge about the inverter layout and operation modes, the loss determination was based solely on prior measurements. Figure 29 illustrates the simple implementation of the inverter losses.

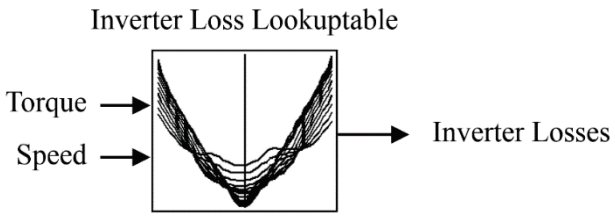

Figure 29: Simulink model for determination of inverter losses

3.1.4 DC Power Calculation

The interface to the DC power supply is the demanded DC current, which is calculated with

$$I_{DC} = \frac{P_{mech} + P_{L,motor} + P_{L,inverter}}{V_{DC}}, \tag{3.4}$$

where $P_{L,motor}$ and $P_{L,inverter}$ are the always positive losses of motor and inverter, P_{mech} is the mechanical power, and V_{DC} is the current battery voltage. Figure 30 shows the implementation of Equation (3.4) in Simulink.

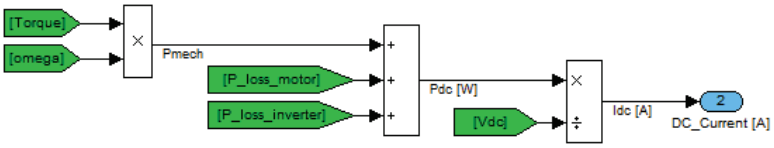

Figure 30: Calculation of DC current

3.1.5 Motor Thermal Model

The approach for the thermal modeling was a lumped element model. This can be easily parameterized or reduced to fit the available parameters and is sufficiently fast for real time operation. The proposed model assumed constant temperature in the axial direction of the machine (i.e. all lumped elements are in one radial plane), except the thermal resistance to the shaft, which also contains an axial component. Therefore, the application of the model is limited to radial flux machines. Figure 31 gives an overview of the proposed network, including the mapping of the dissipated losses. The blue nodes represent the mass points and discrete temperatures of the model, and the arrows show the flow of energy.

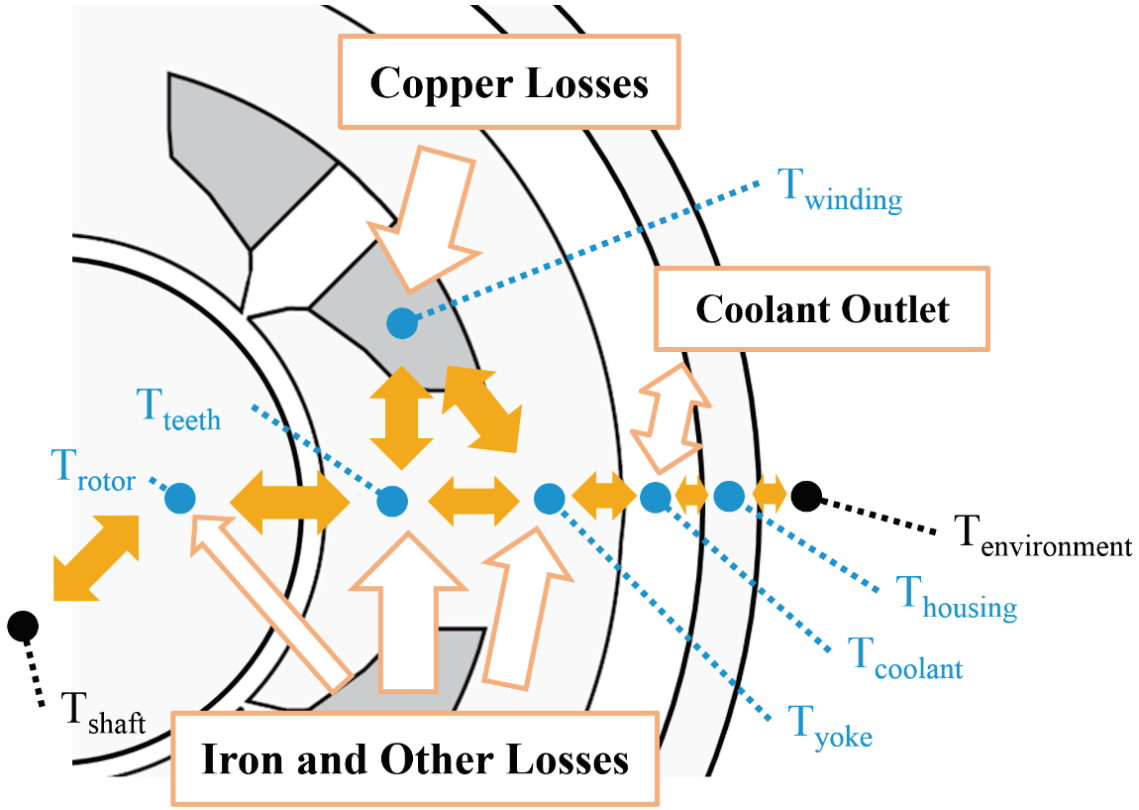

Figure 31: Overview of the motor thermal model

The model consists of six concentrated mass nodes, two constant temperature nodes and eight thermal resistances between these nodes. Figure 32 shows the thermal network with the mentioned parameters. The two nodes T_{shaft} and $T_{environment}$ are boundaries to the surrounding model and were assumed constant.

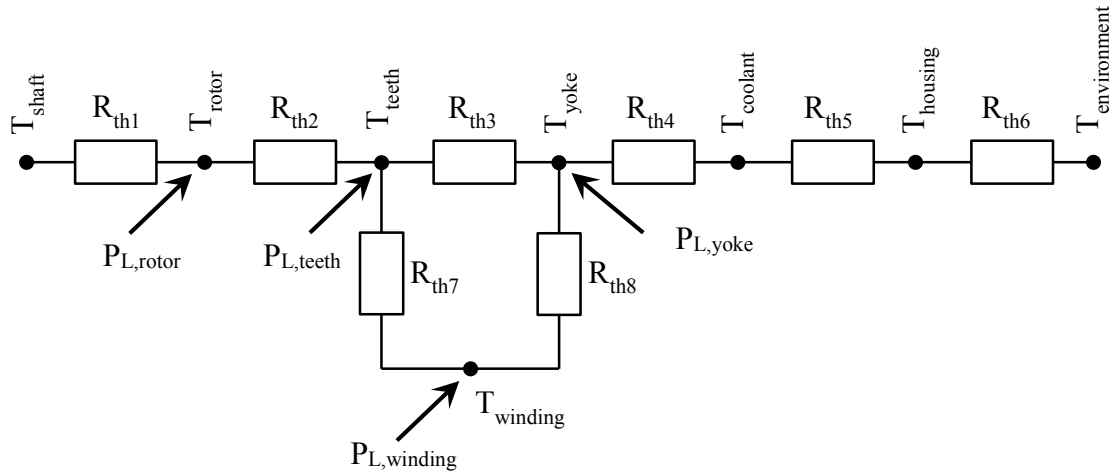

Figure 32: Lumped element model for motor

The mathematical representation for thermal conduction discussed in Section 2.2.4 is based on Equations (2.15) and (2.16). Therefore, the individual temperatures at the nodes are calculated by

$$T_n = \frac{1}{m_n \cdot C_{pn}} \int (P_{Ln} - \dot{q}_n) dt + T_{0n}, \tag{3.5}$$

with n indicating the individual nodes, T_{0n} the initial temperature, m_n the active thermal mass, and C_{pn} the specific heat capacity for each node. The rate of energy coming from the losses P_{Ln} was zero for all elements except *rotor, teeth, yoke* and *winding*. According to the network in Figure 32, the conductive heat flux $\dot{q}_n$ is the sum of two or more heat flux components.

The iron and other losses in each operating point, determined in Section 3.1.3, are distributed to three mass points (Figure 32) for the rotor, stator teeth and stator yoke. Due to the simplicity of the proposed lumped parameter model, the iron, ventilation, and friction losses are mapped onto those three nodes. Since the distribution is highly affected by the rotational speed of the motor, the model requires a table with the proportions of losses occurring in the rotor, stator teeth and yoke over the machine's operating speed range. As

an example, Figure 33 shows the effect of motor speed on different sources of iron loss [17].

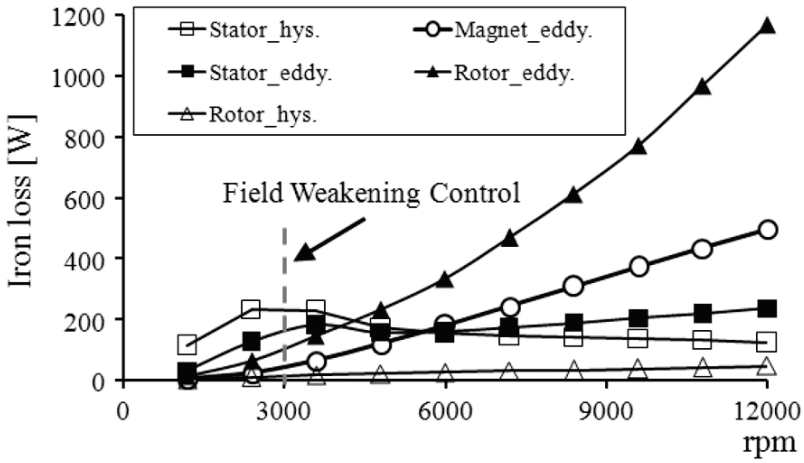

Figure 33: Sources of iron losses over rotor speed in an IPM machine [17]

The model of the water cooling was designed following the approach in [18]. There, spatially constant temperatures on the motor and housing surface, and constant liquid density and heat capacity are assumed. The average temperature of the liquid in the motor was assumed as

$$T_{coolant} = \frac{T_{wi} + T_{wo}}{2}, \tag{3.6}$$

where T_{wi} and T_{wo} are the liquid temperatures at the inlet and outlet of the cooling jacket, respectively. The resulting heat balance equation was

$$wC_p \frac{dT_{wo}}{dt} = \dot{w}C_p(T_{wi} - T_{wo}) + \dot{q}_{yoke2coolant} - \dot{q}_{coolant2housing}, \tag{3.7}$$

where w is the mass of liquid in the cooling jacket, $\dot{w}$ the liquid mass flow, C_p the liquid specific heat capacity, and $\dot{q}$ the heat flux from the adjacent nodes, stator yoke and housing. These were calculated with

$$\begin{aligned} \dot{q}_{yoke2coolant} &= \frac{1}{R_{th4}} \left(T_{yoke} - T_{coolant}\right) \\ and\ \dot{q}_{coolant2housing} &= \frac{1}{R_{th5}} \left(T_{coolant} - T_{housing}\right) \end{aligned} \tag{3.8}$$

with temperatures and thermal resistances according to Figure 32. The full motor thermal model that was implemented in Simulink can be found in APPENDIX B.

3.1.6 INVERTER THERMAL MODEL

Similar to the motor thermal model, the inverter thermal model is a lumped parameter type. Figure 34 illustrates the model layout that consists of four discrete mass points (blue nodes), where one of them represents the liquid cooling, and the constant environment temperature (black node). The dissipated heat is mapped onto the node for the semiconductor junction. The yellow arrows show the flow of energy between the nodes. Most of the energy leaves the system through the coolant outlet.

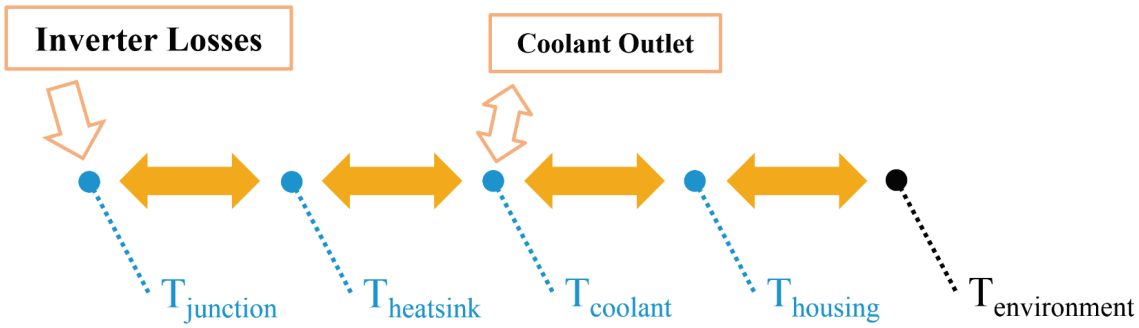

Figure 34: Overview of the inverter thermal model

The mathematical definition is similar to the motor thermal model, and based on Equations (3.5)-(3.8). Figure 35 shows the thermal lumped parameter network for the inverter.

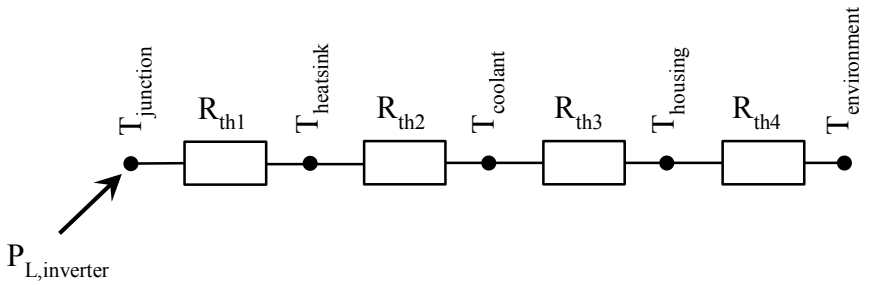

Figure 35: Lumped element model for inverter

The full inverter thermal model that was implemented in Simulink can be found in APPENDIX C.

3.2 PARAMETERIZATION

An essential part of the project was deriving the parameters for the model from real data and measurements. The parameters listed below are general parameters, which can be obtained from the motor datasheet or by conducting simple measurements.

- Rated Torque
  maximum motor torque in constant torque range
- Rated Speed
  maximum motor speed at full torque (start of field weakening)
- Maximum Speed
  absolute maximum motor speed
- Number of Phases
  number of stator phases
- Stator Winding Resistance
  mean stator winding resistance and winding temperature at measurement

Further necessary parameters and their determination are explained in the following sections.

3.2.1 ELECTROMECHANICAL PARAMETERS

Parameterization of the electromechanical part is done primarily with the general parameters listed above. Below are additional parameters for this particular part.

- Minimum DC voltage for normal operation
  minimum supply voltage where motor can run at full power
- Torque delay
  time constant of delay between torque demand and actual motor torque

Similar to the general parameters, the minimum supply voltage for normal operation should be given by the motor or inverter manufacturer. The motor torque delay can be measured by using a torque demand step as the controller input and measuring the resulting motor torque response. The time constant is the time from the input step until the output response reaches 63% of the demand value.

3.2.2 MOTOR LOSS PARAMETERS

For calculations of the motor losses, the motor efficiency, stator current and winding temperature needed to be measured for a number of operating points covering the full operating range of the machine. Figure 36 shows an example distribution of measurements.

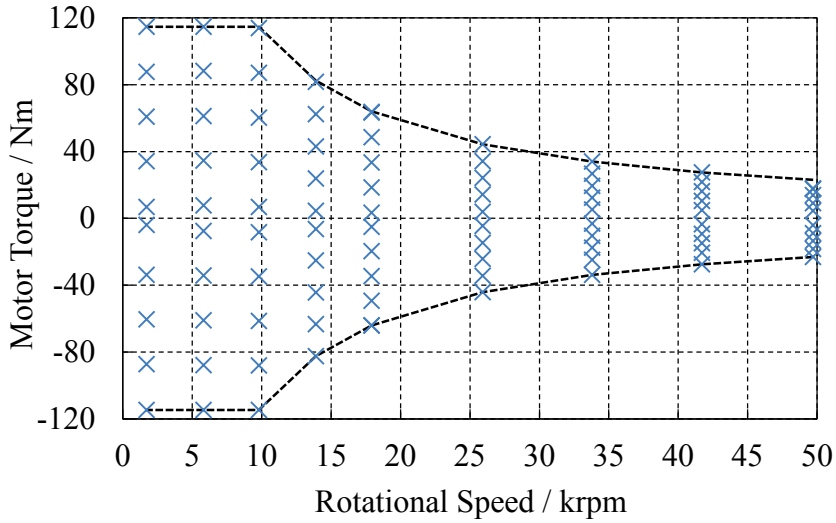

Figure 36: Example distribution of measurements over motor operating range

From this set of measurements, the motor losses $P_{L,motor}$ were calculated with

$$P_{L,motor} = T \cdot \omega \cdot \frac{(1-\eta_M)}{\eta_M} \quad for\ T > 0 \quad or$$
$$P_{L,motor} = -T \cdot \omega \cdot (1-\eta_M) \quad for\ T < 0, \tag{3.9}$$

depending on the flow of energy in each operating point. T is the motor torque, ω is the angular frequency, and η_M is the measured efficiency. The motor losses could then be separated into copper losses and other losses which include iron, ventilation and friction losses. Using Equation (3.2) to obtain the copper losses P_{cu} for each operating point, the other losses $P_{L,other}$ were calculated with

$$P_{L,other} = P_{L,motor} - P_{cu}. \tag{3.10}$$

The acquired values for stator current and iron and other losses at each point of measurement had to be converted into a continuous plane across the operating range and then discretized to be used in the Simulink model (Figure 37 and Figure 38). The Matlab code

for the generation of the necessary maps from measurement data can be found in APPENDIX A.

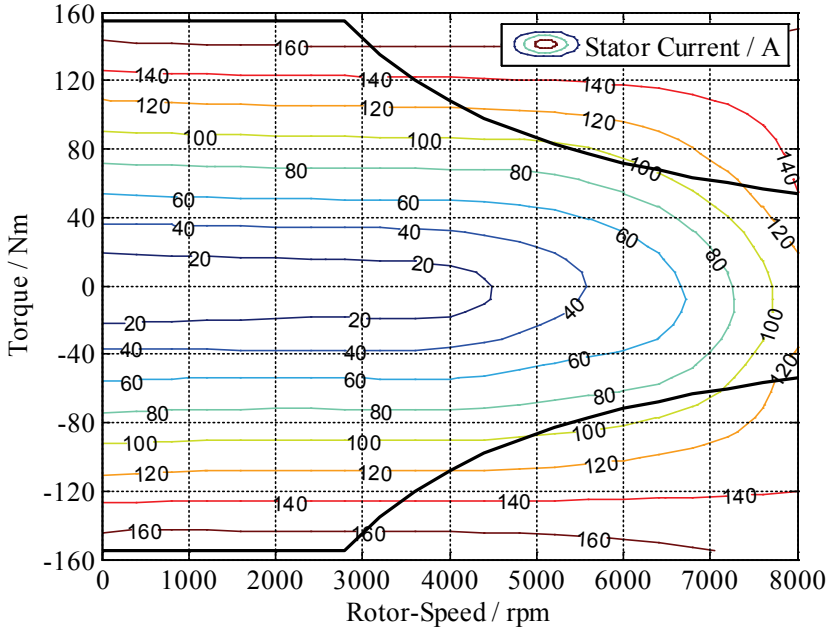

Figure 37: Example stator current map generated from measurements

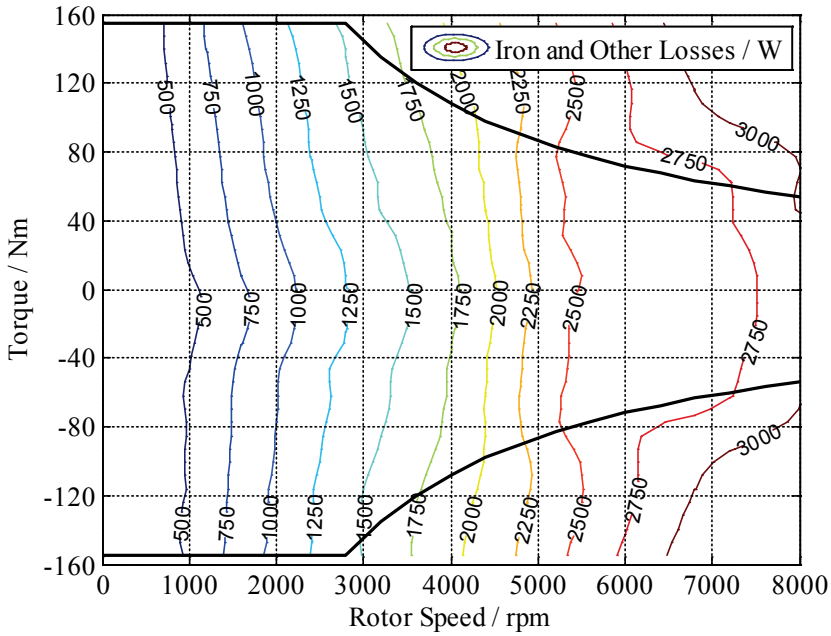

Figure 38: Example iron loss map generated from measurements

3.2.3 INVERTER LOSS PARAMETERS

Similar to the motor loss parameters, inverter efficiency measurements across the full operating range were required. The inverter losses were calculated and then interpolated and discretized for use in the Simulink model using

$$\begin{aligned} P_{L,inverter} &= \left(T \cdot \omega + P_{L,motor}\right) \cdot \frac{(1-\eta_I)}{\eta_I} \qquad for\ T > 0 \\ and\ P_{L,inverter} &= \left(-T \cdot \omega + P_{L,motor}\right) \cdot (1-\eta_I) \quad for\ T < 0 \end{aligned} \tag{3.11}$$

where η_I is the measured inverter efficiency at each operating point and $P_{L,motor}$ is the calculated motor losses. Figure 39 shows an example map of iron losses for the full operating range.

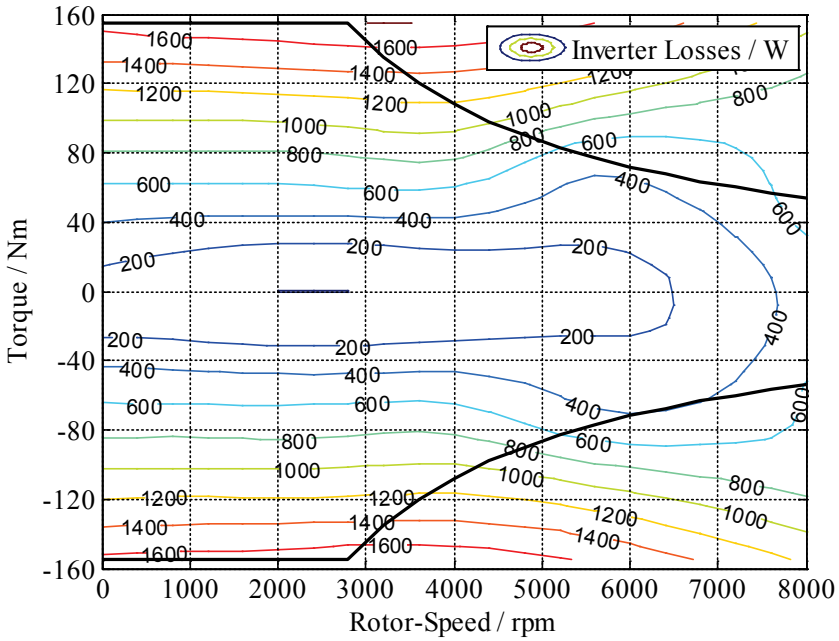

Figure 39: Example inverter loss map from measurements

3.2.4 MOTOR THERMAL PARAMETERS

Parameters for the motor lumped element model include thermal resistances, heat capacities and masses (Figure 32). In addition, the distribution of losses to rotor, teeth and stator yoke and the initial temperature for each node are required to fully parameterize the model. All necessary parameters are listed below.

- Thermal resistances
  - Shaft – Rotor (R_{th1})
  - Rotor – Stator teeth (R_{th2})
  - Stator teeth – Stator yoke (R_{th3})
  - Stator yoke – Cooling (R_{th4})
  - Cooling – Housing (R_{th5})
  - Housing – Environment (R_{th6})
  - Winding – Stator teeth (R_{th7})
  - Winding – Stator yoke (R_{th8})
- Specific heat capacities, masses and initial temperatures
  - Rotor ($C_{p\ rotor}, m_{rotor}, T_{0\ rotor}$)
  - Stator teeth ($C_{p\ teeth}, m_{teeth}, T_{0\ teeth}$)
  - Stator yoke ($C_{p\ yoke}, m_{yoke}, T_{0\ yoke}$)
  - Stator winding ($C_{p\ winding}, m_{winding}, T_{0\ winding}$)
  - Cooling liquid ($C_{p\ coolant}, m_{coolant}, T_{0\ coolant}$)
  - Housing ($C_{p\ housing}, m_{housing}, T_{0\ housing}$)
- Iron loss distribution between rotor, stator teeth and stator yoke

Since the thermal conductivities and iron loss distribution are not easy to measure, ways to analytically calculate these parameters based physical data are explained in the following sections. The number of nodes in the model can also be reduced to the desired size by simply setting the unsuitable thermal resistances and masses to zero.

3.2.4.1 THERMAL RESISTANCES

The thermal resistances used in Figure 32 can be calculated using the formulas proposed in [19]. The necessary geometric dimensions are illustrated in Figure 40.

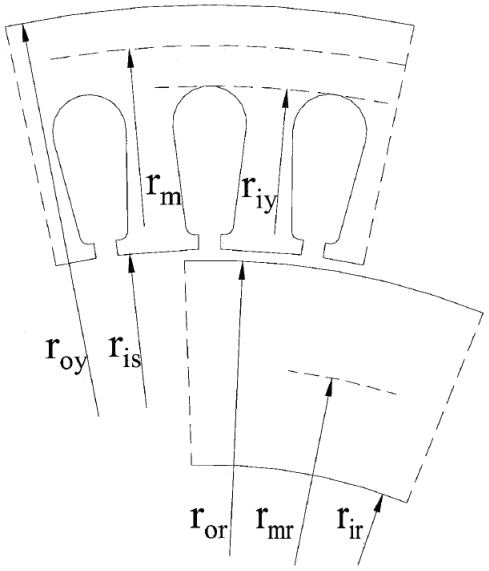

Figure 40: Definition of motor dimensions for thermal parameter calculation according to [19]

R_{th1} – Shaft to Rotor

R_{th1} represents the thermal resistance between the rotor and the shaft in radial direction as well as the resistance of the shaft for heat conduction outside of the engine. It is calculated by

$$R_{th1} = \frac{1}{2}\left(\frac{0.5\left(l_{shf} - l_S\right)}{k_{ir}\pi r_{ir}^2}\right) + \frac{1}{4}\left(\frac{0.5 l_S}{k_{ir}\pi r_{ir}^2}\right) + \frac{1}{2\pi k_{ir} l_S}\ln\left(\frac{r_{mr}}{r_{ir}}\right) \tag{3.12}$$

with l_{shf} as the length of the shaft, l_S the length of the stator and k_{ir} the iron thermal conduction coefficient. The first, second, and third term in the equation represents the resistance of the external part of the shaft, the shaft inside the rotor, and the resistance of the inner part of the rotor, respectively.

R_{th2} – Rotor to Stator Teeth (air gap)

The convective heat transfer in the air gap follows the Taylor-Couette Flow for fluids between two concentric rotating cylinders. The following describes the calculation method according to [19] and [20].

The most common definition for the Taylor number is

$$N_{Ta} = \frac{\omega^2 r_{or} \left(\frac{r_{is}-r_{or}}{2}\right)^3}{\nu^2}, \tag{3.13}$$

Where ω is the angular velocity of the rotor, r_{or} the outer radius of the rotor, r_{is} the inner radius of the stator, and ν the kinematic viscosity of the fluid in the air gap. At low speeds ($N_{Ta} < 1700$), the Nusselt number N_{Nu} is set constant to 2.2. For higher speeds ($N_{Ta} > 1700$), the Nusselt number is defined as

$$N_{Nu} = 0.23\, N_{Ta}^{0.63} \cdot N_{Pr}^{0.27}, \tag{3.14}$$

with the Prandtl number $N_{Pr} = \nu/a$, where a is the thermal diffusivity of the fluid. Once the Nusselt number is obtained, the convective heat transfer coefficient can be calculated by

$$h_{airgap} = \frac{N_{Nu} \cdot k_{air}}{r_{is} - r_{or}}, \tag{3.15}$$

where k_{air} is the air thermal conductivity. Ultimately, the thermal resistance can be calculated with

$$R_{th2} = \frac{1}{2\pi k_{ir} l_S} \ln\left(\frac{r_{or}}{r_{mr}}\right) + \frac{1}{2\pi h_{airgap} \frac{r_{or}+r_{is}}{2} l_S} + \frac{1}{2\pi k_{ir} l_S p_{ir}} \ln\left(\frac{\frac{r_{iy}+r_{is}}{2}}{r_{is}}\right). \tag{3.16}$$

The equation is the sum of three terms. The first term is the conductive thermal resistance of the proportional part of the rotor between mass point and air gap. This has to be adapted according to the actual geometry of the rotor, including additional air gaps and permanent magnets. The second term represents the convective thermal resistance of the air gap. The third term is the conductive thermal resistance of the proportional part of the stator teeth between the mass point for teeth and air gap, where p_{ir} is the percentage of the stator teeth volume with respect to the total teeth and slots volume.

R_{th3} –Stator Teeth to Stator Yoke

Assuming the node for the teeth is in the center of the teeth, and the node for the yoke is in the radial center of the yoke, the thermal resistance between these nodes can be obtained by

$$R_{th3} = \frac{1}{2\pi k_{ir} l_S p_{ir}} \ln\left(\frac{r_{iy}}{\frac{r_{iy}+r_{is}}{2}}\right) + \frac{1}{2\pi k_{ir} l_S} \ln\left(\frac{r_m}{r_{iy}}\right). \quad (3.17)$$

The first term of the equation is half of the thermal resistance of the teeth, and the second term is the thermal resistance of the inner half of the stator yoke.

R_{th4} –Stator Yoke to Coolant

The thermal resistance between the stator yoke node and the coolant can be calculated with

$$R_{th4} = \frac{1}{2\pi k_{ir} l_S} \ln\left(\frac{r_{oy}}{r_m}\right) + \frac{1}{2\pi h_{yc} r_{oy} l_C}. \quad (3.18)$$

The first term of the equation is the outer half of the stator yoke thermal resistance. The second part is the thermal resistance between stator yoke and coolant, where h_{yc} is the conductive heat transfer coefficient between stator yoke and cooling liquid and l_C is the axial length of the cooling jacket. Since h_{yc} is largely dependent on the fluid dynamics in the cooling jacket, there is no easy way to calculate it analytically. The DC supply test (see page 43) is a way to obtain it by measurement.

R_{th5} – Coolant to Housing

The thermal resistance between the cooling liquid and the motor housing is calculated with

$$R_{th5} = \frac{1}{2\pi h_{ch}(r_{oy} + d_c) l_C}, \quad (3.19)$$

where h_{ch} is the conductive heat transfer coefficient from coolant to housing and d_c the width of the cooling jacket. Like h_{yc}, $h_{ch}$is best obtained by the DC supply test.

R_{th6} – Housing to Environment

Assuming natural convection outside of the motor, the thermal resistance between the motor housing and the environment can be obtained by the DC supply test with

$$R_{th6} = \frac{T_{case} - T_{air}}{P_{DC}}, \tag{3.20}$$

where T_{case} is the temperature of the case, T_{air} is the ambient temperature and P_{DC} is the heat flux from housing to environment, all obtained from the DC supply test.

R_{th7}, R_{th8} – Stator Winding to Stator Teeth and Yoke

The thermal resistance between stator winding and stator core depends both on the fill coefficient of the winding in the slot and the insulation technique. The overall conductive resistance from winding to iron can be obtained by

$$R_{cu,ir} = \frac{d_{eq}}{k_{cu,ir} A_{slot}}, \tag{3.21}$$

with A_{slot} as the contact area between winding and stator iron ($A_{slot} = l_{sb} l_S$), $k_{cu,ir}$ the equivalent conductivity coefficient of the air and insulation material in the stator slots (evaluated by the DC supply test), and d_{eq} as the equivalent thickness of the air and insulation material of the stator slots, which is calculated with

$$d_{eq} = \frac{S_{slot} - S_{cu}}{l_{sb}}, \tag{3.22}$$

where S_{slot} is the cross-sectional area of the stator slot, S_{cu} is the cross-sectional area of copper in the stator slot, and l_{sb} is the perimeter of the stator slot. The obtained overall heat resistance can then be split up into the teeth and yoke parts considering the thermal admittance, $G_{th} = 1/R_{th}$, with

$$G_{cu,ir} = G_{th7} + G_{th8}. \tag{3.23}$$

The teeth and yoke parts are proportional to the cross-sectional area of the heat transfer, and therefore have the relationship

$$\begin{aligned} G_{th7} &= \frac{A_{cu,th}}{A_{slot}}\, G_{cu,ir} \\ and\ G_{th8} &= \frac{A_{cu,yk}}{A_{slot}}\, G_{cu,ir} \end{aligned} \tag{3.24}$$

where $A_{cu,th}$ is the contact area between winding and stator teeth, and $A_{cu,yk}$ is the contact area between winding and stator yoke. Ultimately the thermal resistances can be calculated as

$$R_{th7} = \frac{A_{slot}}{A_{cu,th}} R_{cu,ir}$$
$$and\ R_{th8} = \frac{A_{slot}}{A_{cu,yk}} R_{cu,ir}. \tag{3.25}$$

DC Supply Test

As mentioned previously, the parameters h_{yc}, h_{ch}, R_{th6} and $k_{cu,ir}$ can be obtained with a DC supply test, where the rotor is at a standstill and the only source of losses are copper losses defined by $P = I^2R$. The DC supply measurement proposed in [19] with adaptations to comply with the thermal model used in this thesis is explained in the following sections.

The motor, at zero speed and with series or parallel connected windings, is supplied with a DC current (50% to 70% of the rated current). In thermal steady-state conditions, the temperatures of stator windings, stator teeth, stator yoke, coolant, housing and ambient have to be measured. By solving the proposed thermal network (Figure 32, page 31), the desired parameters can be calculated.

3.2.4.2 IRON AND OTHER LOSS DISTRIBUTION

The distribution of iron losses within an electric machine is highly affected by the type of motor, the motor's geometry and the materials used. Ways for determining these losses are using finite element analysis or taking thermal measurements (requires a motor with several temperature probes in the laminations). These approaches are reported in [17, 21] for an IPM machine. The model requires data for the proportional iron losses in rotor, stator teeth and stator yoke over the whole operating speed range. If neither FEA nor thermal measurements are feasible, the data must be provided by the motor manufacturer.

3.2.5 INVERTER THERMAL PARAMETERS

Parameters for the inverter lumped element model include thermal resistances, heat capacities and masses (Figure 35). The necessary parameters are listed below.

- Thermal resistances
  - Junction – Heat sink (R_{th1})
  - Heat sink – Coolant (R_{th2})
  - Coolant – Housing (R_{th3})
  - Housing – Environment (R_{th4})
- Specific heat capacities, masses and initial temperatures
  - Junction ($C_{p\ junction}, m_{junction}, T_{0\,junction}$)
  - Heat sink ($C_{p\ heatsink}, m_{heatsink}, T_{0\ heatsink}$)
  - Coolant ($C_{p\ coolant}, m_{coolant}, T_{0\ coolant}$)
  - Housing ($C_{p\ housing}, m_{housing}, T_{0\ housing}$)

Since the layout and components used in inverters greatly affect these thermal parameters, detailed knowledge about the inverter's structure is necessary to obtain them. Per the model requirements, the user of this model will not have this information. The listed parameters need to be provided by the inverter manufacturer.

Another way to obtain the thermal resistances is by conducting measurements at a thermal steady state and calculating them with

$$R_{th,n} = \frac{\Delta T}{\dot{q}}, \tag{3.26}$$

where ΔT is the temperature difference and $\dot{q}$ the heat flux between two nodes. This requires temperature sensors for each node of the lumped parameter network.

3.3 MODEL VERIFICATION

To prove the operation of the designed model, an existing electric drive was modelled and the simulation results were compared with the measurements. The following sections describe the properties of the drive, the parameterization process, and the comparison of simulations and measurements.

3.3.1 ELECTRIC DRIVE TEST SYSTEM

The electric drive system used as a reference was the UQM PowerPhase 75 (Figure 41), a surface mounted permanent magnet synchronous motor with concentrated windings, supplied by a three phase half bridge inverter with insulated gate bipolar transistors (IGBTs).

Figure 41: UQM PowerPhase 75 drive system [22]

Table 2 gives an overview of the main drive characteristics. It shows that the motor is operated in field weakening mode from 2875rpm to 8000rpm (i.e. can provide the maximum power in more than 50% of its operating range).

Table 2: UQM PowerPhase 75 motor characteristics

Base Speed	2875rpm
Maximum Speed	8000rpm
Base Torque	150Nm
Base Power	45kW
Peak Torque	240Nm
Peak Power	75kW
Maximum Efficiency	94%
Minimum DC Voltage	240V
Cooling Liquid	50/50 Glycol-Water
Number of Phases	3

3.3.2 PARAMETER GENERATION

Following the guidelines in Section 3.2, the parameters for the model were obtained. Most of the general parameters are listed in Table 2 and can be found in the motor datasheet [22]. Unfortunately, several of the measurements required in Section 3.2 could not be obtained, since the test system was destroyed during the tests. The following text explains how all parameters were obtained, either by following the guidelines from Section 3.2 or making appropriate assumptions in order to obtain a value.

To obtain the mean stator winding resistance, the resistances between the three phases ($R_{U-V}, R_{V-U}, R_{W-U}$) were measured at a constant temperature of 25°C (Table 3) and then the mean resistance was calculated using Equation (3.27).

Table 3: Measured stator winding resistances

$R_{U\text{-}V}$	$R_{V\text{-}W}$	$R_{W\text{-}U}$
$m\Omega$	$m\Omega$	$m\Omega$
27.02	27.38	26.48

$$R_S = \frac{R_{U-V} + R_{V-W} + R_{W-U}}{6} = 13{,}48 m\Omega \text{ @ } 25°\text{C} \tag{3.27}$$

3.3.2.1 ELECTROMECHANICAL PARAMETERS

The minimum DC voltage for normal operation was obtained from the motor datasheet and is 240 volts. From this base value, a power derating table was generated (Figure 24, page 26).

For the motor's torque response, a minimum of one step response needs to be measured on a test bench. This was not possible due to damage on the test motor. Consequently, an average value based on prior measurements done by the author in laboratory classes at the Electric Drives and Machines Institute at Graz University of Technology was assumed. These measurements do not perfectly apply to the UQM drive system, but are sufficiently accurate to prove the validity of this model. Table 4 shows the used electromechanical parameters.

Table 4: Electromechanical parameters for the UQM PowerPhase 75

V_{DC_min}	τ
V	ms
240	5.0

3.3.2.2 MOTOR AND INVERTER LOSS PARAMETERS

The motor loss parameters were obtained from measurements of steady state operating points across the whole operating range. The number of measured operating points was 123, evenly distributed to the motoring and generating mode. Figure 42 shows the measured operating points.

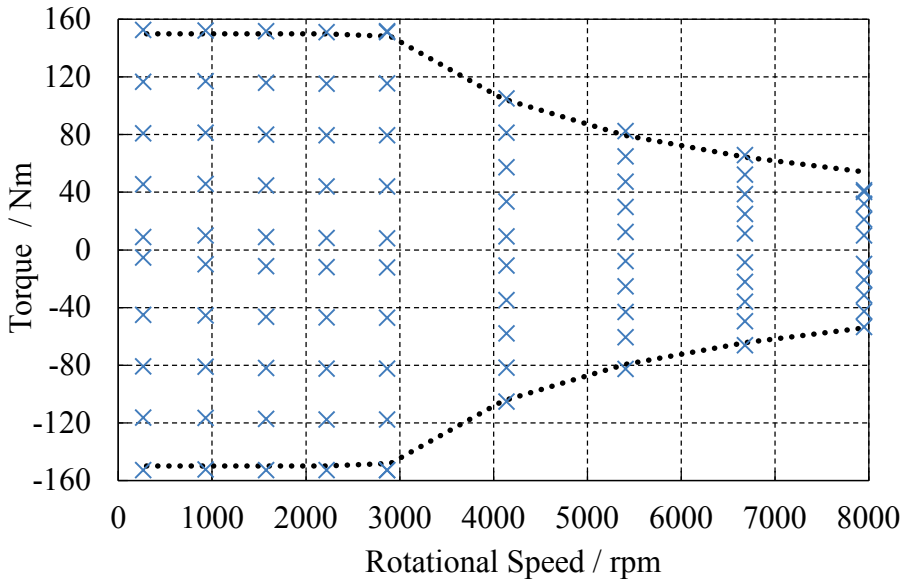

Figure 42: Measured operating points for UQM PowerPhase 75

For each operating point, the following components were measured:

- Motor speed
- Motor torque
- Motor efficiency
- Inverter efficiency
- Average stator phase current (RMS)
- Winding temperature.

With these values, the model parameters for the motor and inverter loss calculation were generated following Sections 3.2.2 and 3.2.3. The stator current, iron loss, and inverter

loss maps generated from these measurements are shown in Figure 37, Figure 38 and Figure 39 (pp. 36-37), respectively.

3.3.2.3 MOTOR THERMAL PARAMETERS

For the thermal parameters, the guidelines from Section 3.2.4 could not be followed because neither the required geometric data nor the thermal measurements were available. Therefore, a rough estimation of the geometry of the motor was used to calculate a base set of thermal resistances and masses. The specific heat capacities were based on typical material used in this type of machine. These parameters were then adapted and changed to match the available measurements. Table 5, Table 6 and Table 7 list the resulting parameters for the motor thermal model.

Table 5: Thermal resistances for UQM PowerPhase 75 Motor

R_{th1}	R_{th2}	R_{th3}	R_{th4}	R_{th5}	R_{th6}	R_{th7}	R_{th8}
K/W	*K/W*	*K/W*	*K/W*	*K/W*	*K/W*	*K/W*	*K/W*
0.2	0.392	0.03	0.005	0.0145	0.3	0.023	0.053

Table 6: Specific heat capacities for UQM PowerPhase 75 Motor

$C_{p\ rotor}$	$C_{p\ teeth}$	$C_{p\ yoke}$	$C_{p\ winding}$	$C_{p\ coolant}$	$C_{p\ housing}$
J/(kgK)	*J/(kgK)*	*J/(kgK)*	*J/(kgK)*	*J/(kgK)*	*J/(kgK)*
500	500	500	385	4181	897

Table 7: Masses for UQM PowerPhase 75 Motor

m_{rotor}	m_{teeth}	m_{yoke}	$m_{winding}$	$m_{coolant}$	$m_{housing}$
kg	*kg*	*kg*	*kg*	*kg*	*kg*
7	5	12	11	2	2

3.3.2.4 INVERTER THERMAL PARAMETERS

Similar to the motor thermal parameters, there was insufficient data available to obtain the inverter thermal parameters according to Section 3.2.5. Again, values were assumed and adapted to fit the measurements. Table 8, Table 9 and Table 10 show the resulting parameters.

Table 8: Thermal resistances for UQM PowerPhase 75 Inverter

R_{th1}	R_{th2}	R_{th3}	R_{th4}
K/W	*K/W*	*K/W*	*K/W*
0.013	0.015	0.08	0.3

Table 9: Specific heat capacities for UQM PowerPhase 75 Inverter

$C_{p\ junction}$	$C_{p\ heatsink}$	$C_{p\ coolant}$	$C_{p\ housing}$
J/(kgK)	*J/(kgK)*	*J/(kgK)*	*J/(kgK)*
80	897	4181	897

Table 10: Masses for UQM PowerPhase 75 Inverter

$m_{junction}$	$m_{heatsink}$	$m_{coolant}$	$m_{housing}$
kg	*kg*	*kg*	*kg*
0.05	1.5	1.8	0.5

3.3.3 Comparison of Model and Electric Drive Measurements

After the model was fully parameterized, the model's behavior was compared to the real drive system. The measurements from the UQM PowerPhase 75 used for this comparison are from an automated test run covering a large part of its operating range. Because this was the only test run available for this motor, not all features of the model could be evaluated. The test run is illustrated in Figure 43.

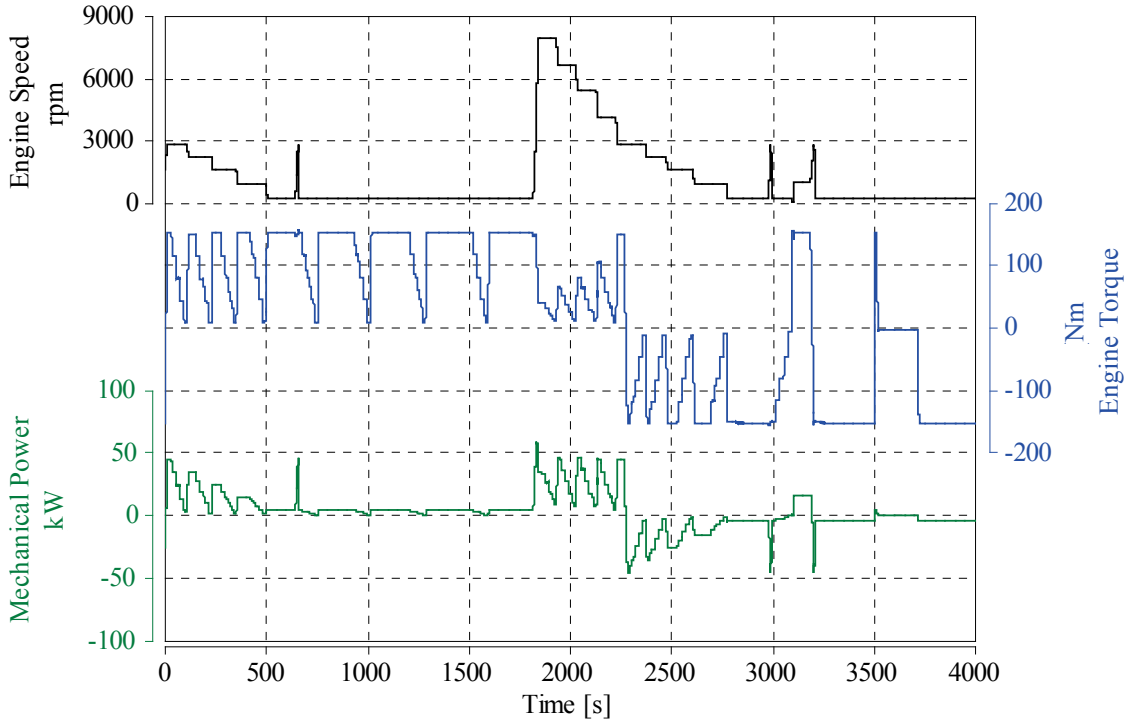

Figure 43: Test run of UQM PowerPhase 75 drive

The measurement was done at a frequency of 10Hz (i.e. a time step of 100ms), which is sufficient for showing the capabilities of the thermal model. However, the transient electromechanical behavior could not be evaluated since the time constant for the torque delay is smaller than the time between two measurements.

The temperatures of the motor coolant at inlet and outlet are illustrated in Figure 44, comparing the measurements with the simulation results. The measured inlet temperature was used as an input for the simulation. The figure shows that the simulated outlet temperature matches very well with the measurement. The largest difference between measurements and model can be found in the beginning, where the thermal model takes additional time to equilibrate. There is also a discrepancy between 2000s and 2500s because around

2100s the motor was operated in overload condition. Overload operation has not been modelled for this test due to the lack of measurements outside the continuous operating range. Besides the coolant temperatures, only the stator winding temperature was measured accurately and could be compared with the simulation results. Figure 45 shows the measured and simulated stator winding temperatures. The simulation matches the measurements well with exception to the range around 2500s. A possible explanation for this deviation could be insufficient accuracy when generating the lookup table for the copper losses.

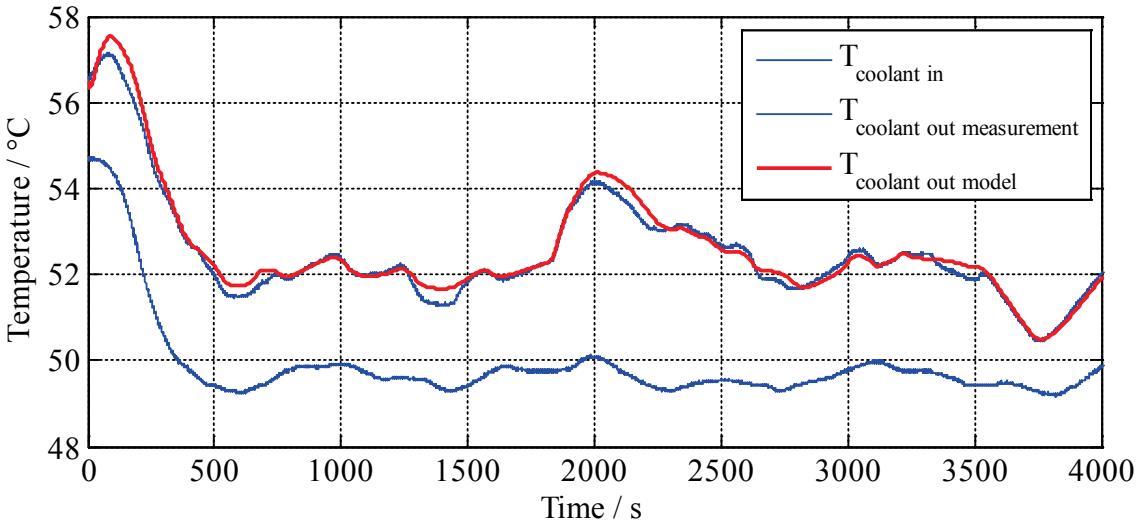

Figure 44: Comparison of motor coolant temperatures

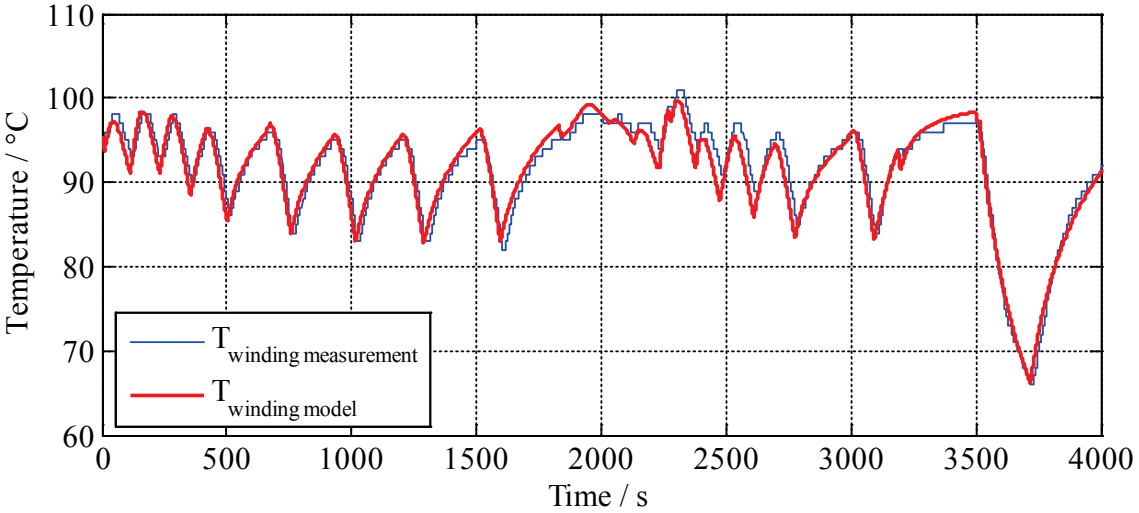

Figure 45: Comparison of stator winding temperatures

The coolant temperatures at the inverter inlet and outlet are illustrated in Figure 46. Similar to the motor simulation, the measured inlet coolant temperature was used as an input

for the model. The simulated outlet coolant temperature matches well with the measurement. The simulation deviates from the measurement in the range between 2000s and 2300s, which is probably the result of a measurement error. After reviewing the test setup and talking to the test rig operators, a possible cause could be additional air convection or vibration at high rotational speeds. Figure 47 compares the DC current from measurement with the simulation result, which matches well. It also shows the overload operation between 1800s and 2300s.

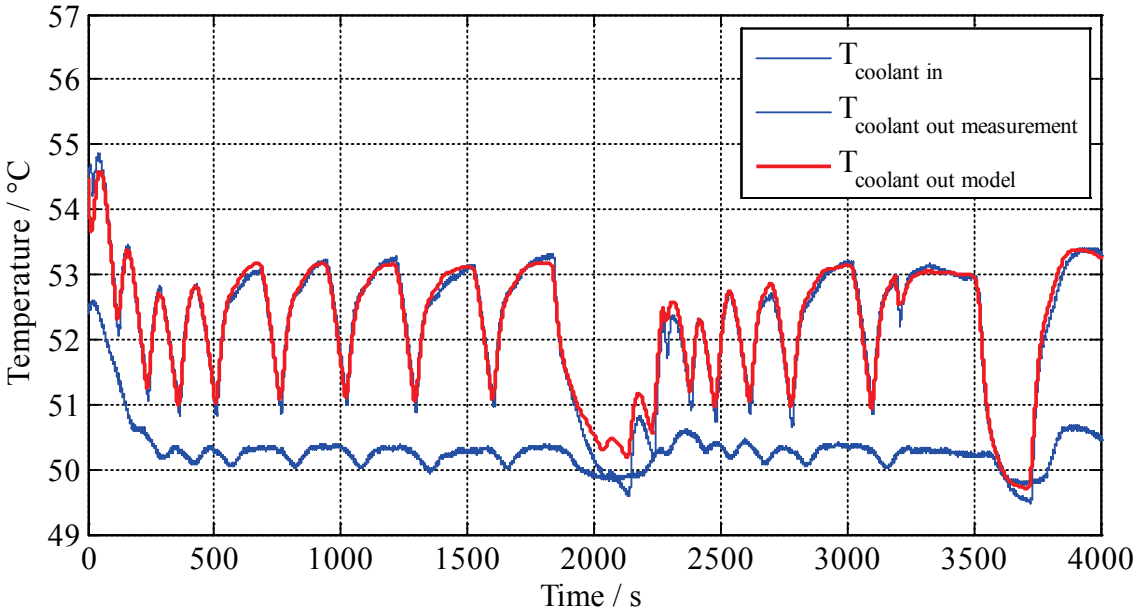

Figure 46: Comparison of inverter coolant temperatures

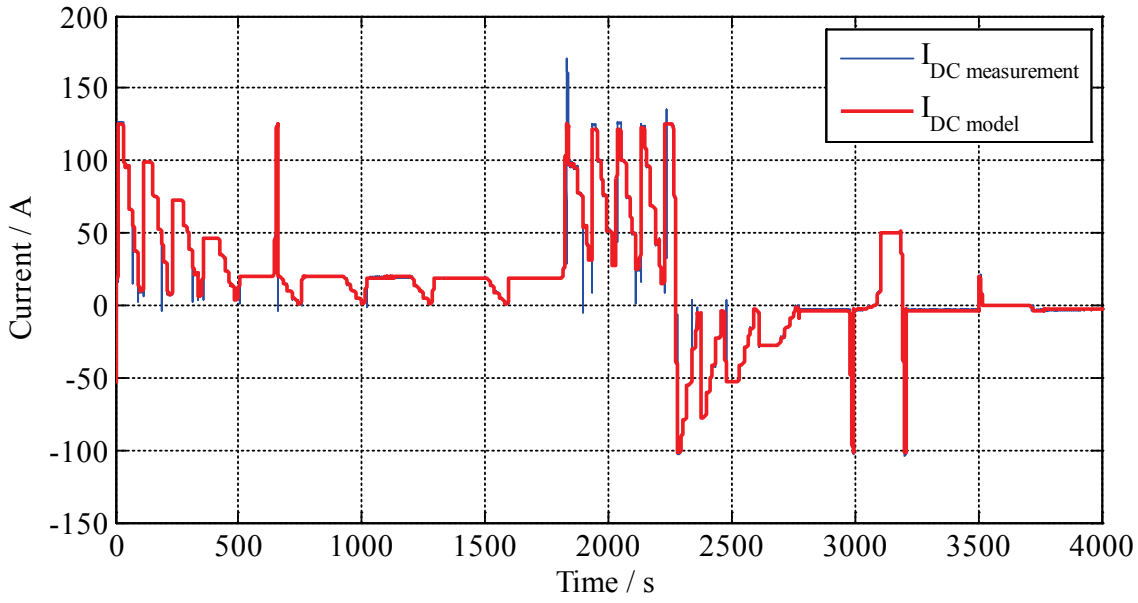

Figure 47: Comparison of DC currents

The mean deviations between the measurement and simulation were calculated, and are listed in Table 11. The simulation results match well with the measurements. Considering the temperature range of the coolant and the winding temperature, it makes sense that the mean deviation for the winding temperature is significantly higher than for the coolant temperatures.

Table 11: Mean deviations between simulation and measurement

$\Delta T_{Coolant\ Out\ Motor}$	$\Delta T_{Coolant\ Out\ Inverter}$	$\Delta T_{Stator\ Winding}$
$°C$	$°C$	$°C$
0.167	0.188	1.864

3.4 INTEGRATION IN THE SIMULATION ENVIRONMENT

The final goal of this work was the integration of the designed model into VSM-PTM, the transient engine model for VSM. The desired hybrid architecture comprises two electric drives and one turbocharged 6 cylinder gasoline internal combustion engine. One electric drive is connected to the ICE crankshaft through a spur gear unit (MGU-K) and the second one is directly attached to the shaft of the turbocharger (MGU-H).

In the following text, the integration of the model into VSM-PTM is explained and the corresponding Simulink models are discussed. Parts of the main layout of the PTM power unit are shown in Figure 48, with the additional blocks for the hybrid parts highlighted with solid red lines and the modified blocks highlighted with dotted red lines. The new *ERS* block contains the electromechanical behavior and loss calculation for both MGU-K and MGU-H, and also a battery model for the energy storage system. To link the MGU-K to the crankshaft, the *MGU-K Gbx* block (see Figure 48) was added, representing the spur gear unit. In the *Cooling ICE Electro* block, the cooling circuit for the electric drives was added, which includes the thermal models for MGU-K and MGU-H and a radiator (Figure 51, page 57).

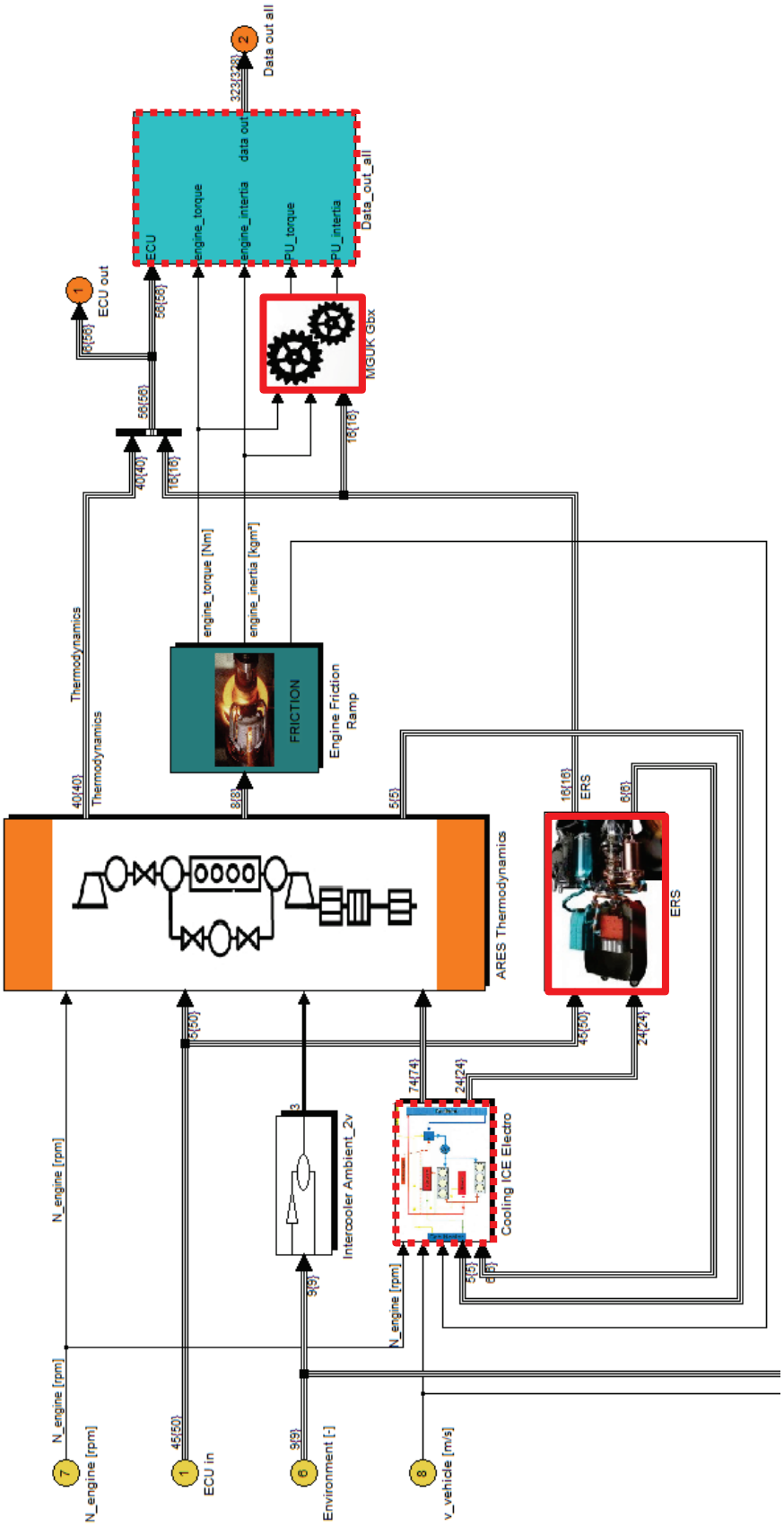

Figure 48: VSM-PTM power unit layout

The *ERS* block in Figure 50 consists of two electric drives and a battery model. Both of the electric drives comprise a model for the electromechanical behavior, loss calculation for motor and inverter, and the DC power calculation described in Section 3.1. The input signals are demand torque, speed, DC voltage and the temperatures from the thermal model. Outputs are the current torque, DC current and the motor and inverter losses. The calculation to the right of the two MGU blocks converts the output data into the VSM-PTM architecture.

The battery model was taken from an existing project within AVL and adapted to fit this application. It is based on a single cell model, including a constant internal resistance and a voltage source (Figure 49). The open circuit voltage (OCV) is a function of the state of charge (SOC) and was parameterized from voltage curves at different discharge rates.

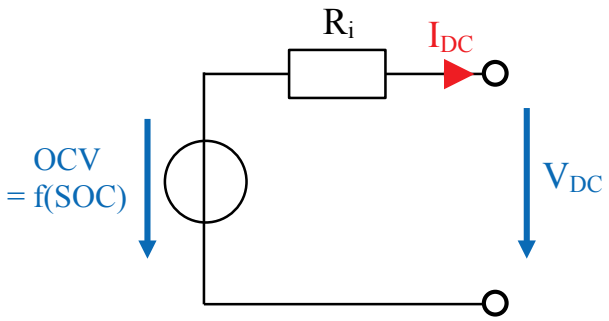

Figure 49: Battery cell model used in VSM-PTM

The input DC current to the battery pack is divided by the number of cells in parallel before being fed into the cell model. The resulting cell voltage is then multiplied by the number of cells in series. The power loss for each cell $P_{L,cell} = I_{DC,cell}^2 R_i$ are multiplied by the overall number of cells in the battery pack to calculate the battery losses.

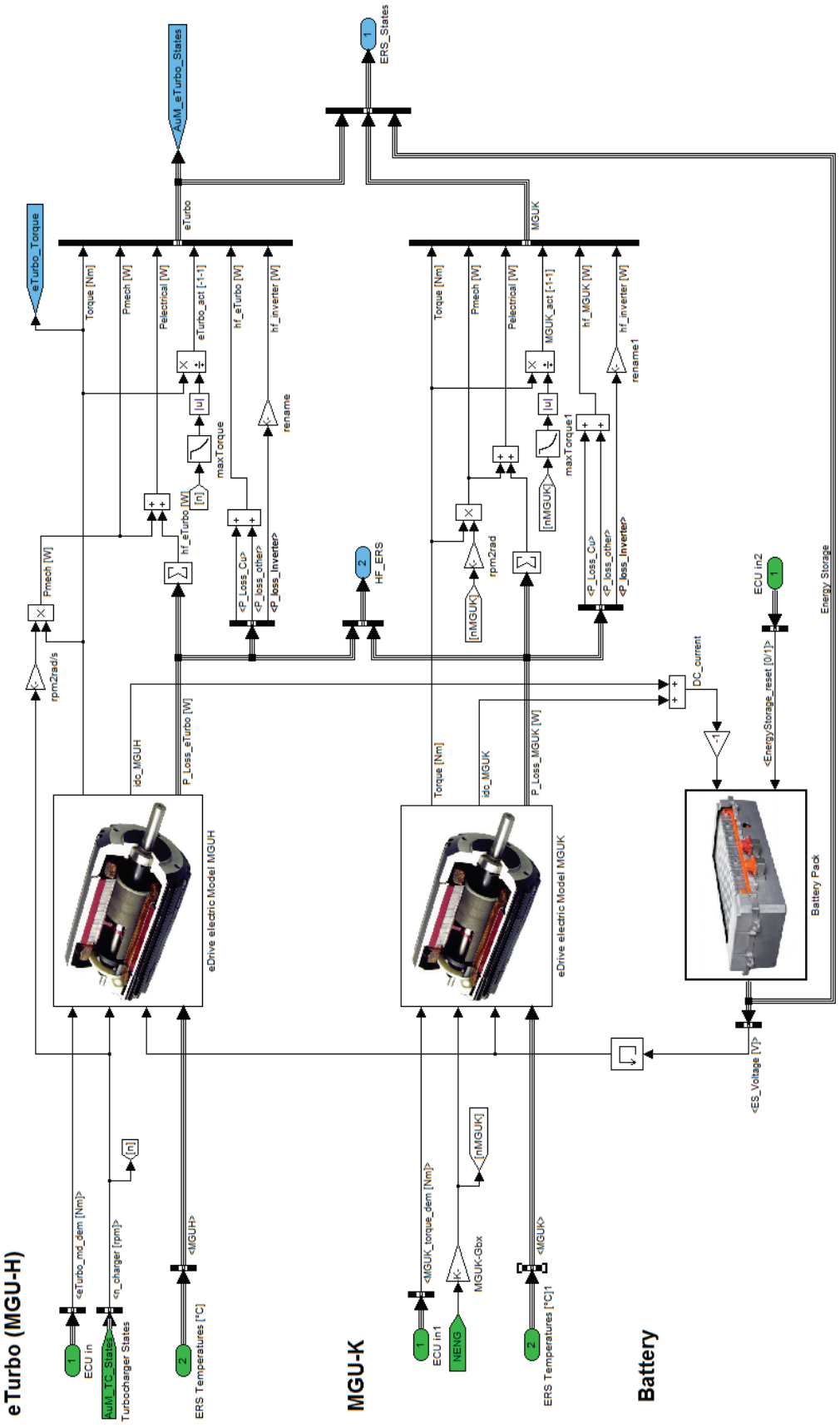

Figure 50: ERS block layout

The thermal models for MGU-H and MGU-K, as well as their common cooling circuit, were implemented in the *Cooling ICE Electro* block and are shown in Figure 51. On the left, the losses coming from the loss calculation in the *ERS* block are fed into the thermal models for motors and inverters. The single thick connecting-line in the model is the flow of cooling liquid. After exiting the radiator, the liquid first flows through the MGU-H motor and inverter, and then MGU-K motor and inverter before flowing back into the radiator.

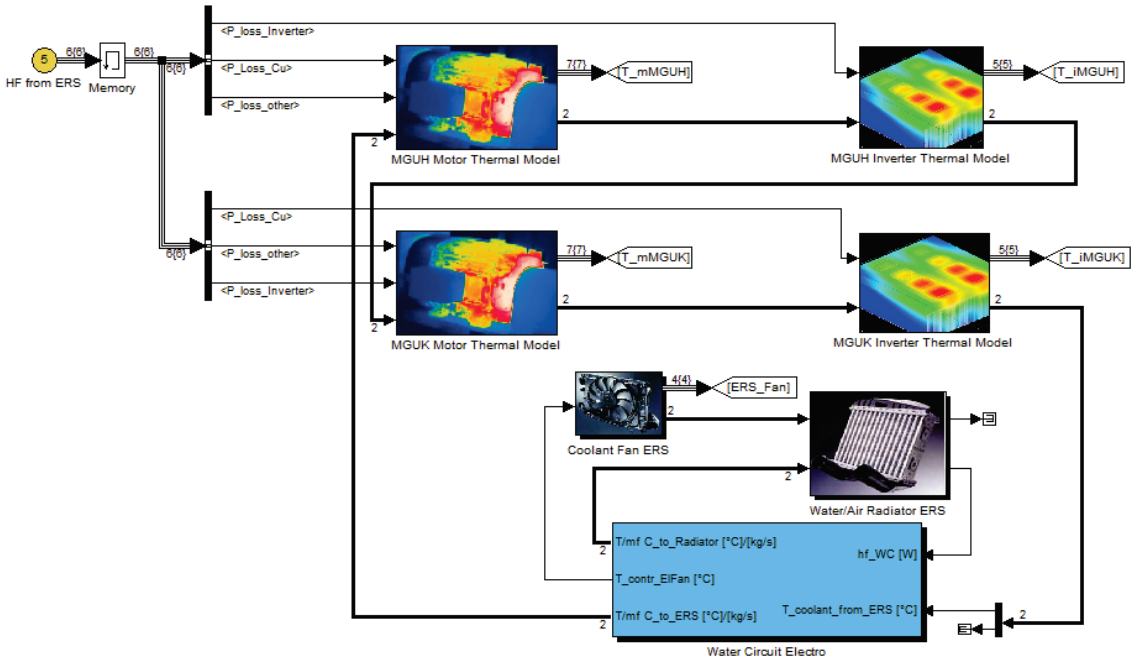

Figure 51: Additional ERS cooling circuit in the Cooling ICE Electro block

The *Water Circuit Electro* block (Figure 52) models the cooling liquid in the hoses between the different components and the coolant pump. As illustrated, the water pump is attached to the ICE crankshaft.

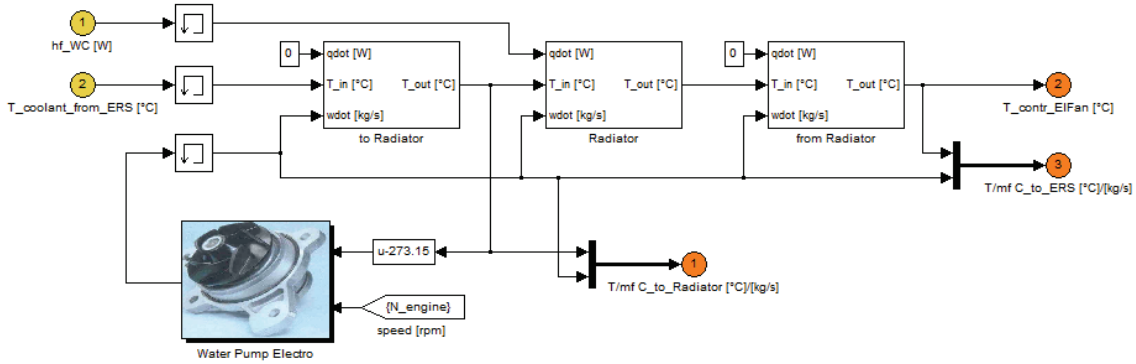

Figure 52: Water circuit electro block

4 RESULTS

The result of this thesis is a flexible and fast model for electric powertrains and the electric parts of hybrid powertrains. The following section first discusses the model capabilities for a single electric drive, and then presents the model behavior in VSM-PTM.

4.1 MODEL CAPABILITIES

The designed model for an electric drive is versatile and meets all the requirements defined in Section 1.2. Due to its simplicity, it can be used for most types of radial flux machines, such as permanent magnet motors, induction motors, or synchronous reluctance motors. In addition, the computation times of the model are short, making it perfectly suitable for real time operation.

As the test with the UQM PowerPhase 75 drive system indicates, the model accuracy seems promising. The model matches the measurements well, with a mean deviation of less than 0.2°C for the coolant outlet temperature, and less than 2°C for the stator winding temperature (Table 11). At this time, only one test has been done to verify the model, which recorded only parts of the necessary channels. Consequently, the full model behavior could not be tested. While the general characteristics of the thermal model look good, there were no measurements available to verify the full range of modelled temperatures or any dynamic operation.

The proposed parameterization methods make it easy to set up the model, pending the acquisition of specific measurements on a test rig. In case that not all nodes of the thermal model are needed, the model can be further simplified by reducing the number of lumped elements.

The model provides the physical interfaces that were required for integration into VSM-PTM and combination with the battery model. The interfaces of the thermal models were designed in a way that the order of the components in the cooling circuit can be easily changed.

Since the model is simple, there are several limitations. Due to the required measurements of motor and inverter, the model is not suitable for electric drive development, which would require evaluation of the effects of changes in specific machine parameters or control algorithms. The only way to do this is to make new measurements or do appropriate simulations in order to get the required input data for the model. Another major limitation stems from the fact that the model uses measurements of steady state operating points and does not account for any transient behavior in the machine other than torque delay.

4.2 SIMULATION IN VSM-PTM

To show how the designed model works within VSM-PTM, a demonstration simulation has been set up. It uses a typical setup for open wheeled single seater cars with a turbocharged V6 engine, including two electric motors (see Section 3.4). Because no measurements of electric drives used in racing applications were available, parameters were formulated based on the measurements from the UQM PowerPhase 75 (see Section 3.3.1) and the 2014 Formula One regulations [4]. The maximum power for the MGU-K is 120kW, with a maximum speed of 50krpm. The maximum power of the MGU-H is 100kW. The simulation was done for one lap on the Italian race track Autodromo Nazionale Monza (Figure 53).

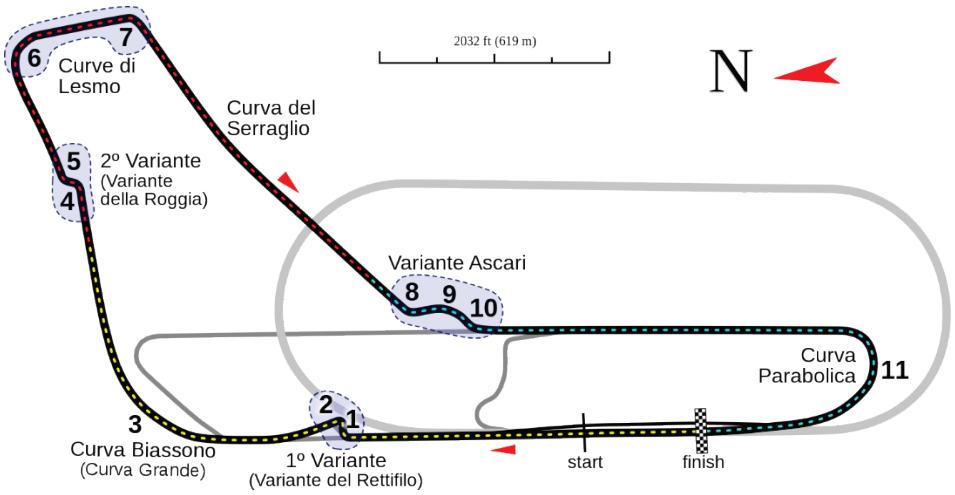

Figure 53: Autodromo Nazionale Monza track layout [23]

Some of the simulation results are presented on the following pages. Figure 54 gives a general overview of the lap with the vehicle speed plotted in the top graph and the corresponding pedal positions below. It shows the four long wide open throttle sections of the

track, as well as the characteristic corners, most notably the *Curva di Lesmo* from 2000m to 2500m. The two bottom plots in Figure 54 show the torque and rotational speed of the ICE. Again, these plots reflect the track layout well. The shift operations are visible, causing only a minor torque reduction during the shift due to the use of a sequential gearbox.

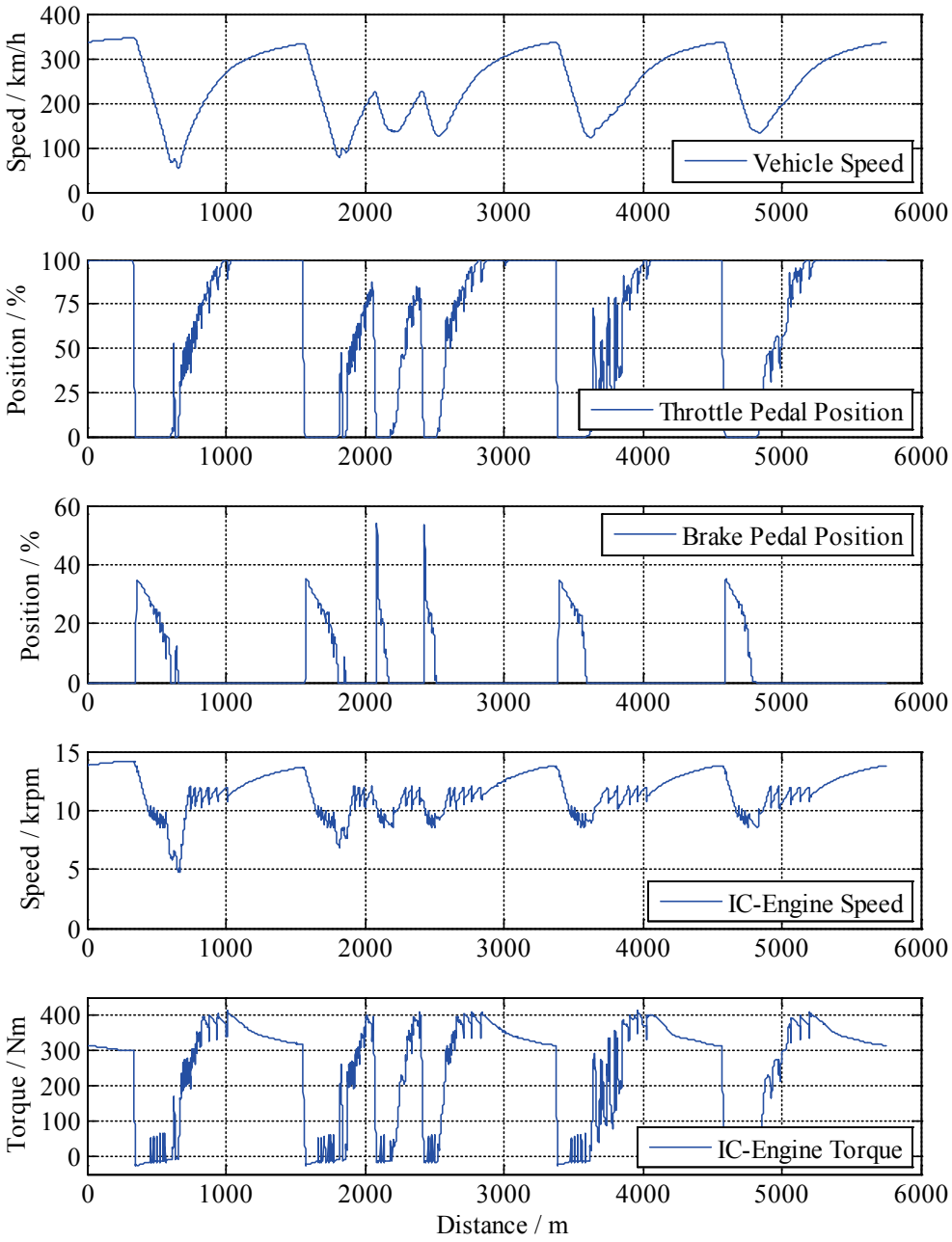

Figure 54: VSM Monza Lap Vehicle Data

Figure 55 shows information about the two electric drives in the powertrain (i.e. rotational speed and torque for MGU-K and MGU-H). The MGU-K is attached to the ICE crankshaft through a single speed transmission, and therefore shows the same speed profile as

the ICE. In contrast, the MGU-K torque curve differs greatly from the ICE curve because a negative torque is applied when braking to harness braking energy and recharge the battery. In the acceleration phases, the MGU-K does not start operating until the ICE approaches full throttle. Below this threshold, the wheels are mostly operated at the slip limit and additional torque from the MGU-K would only result in wheel spin.

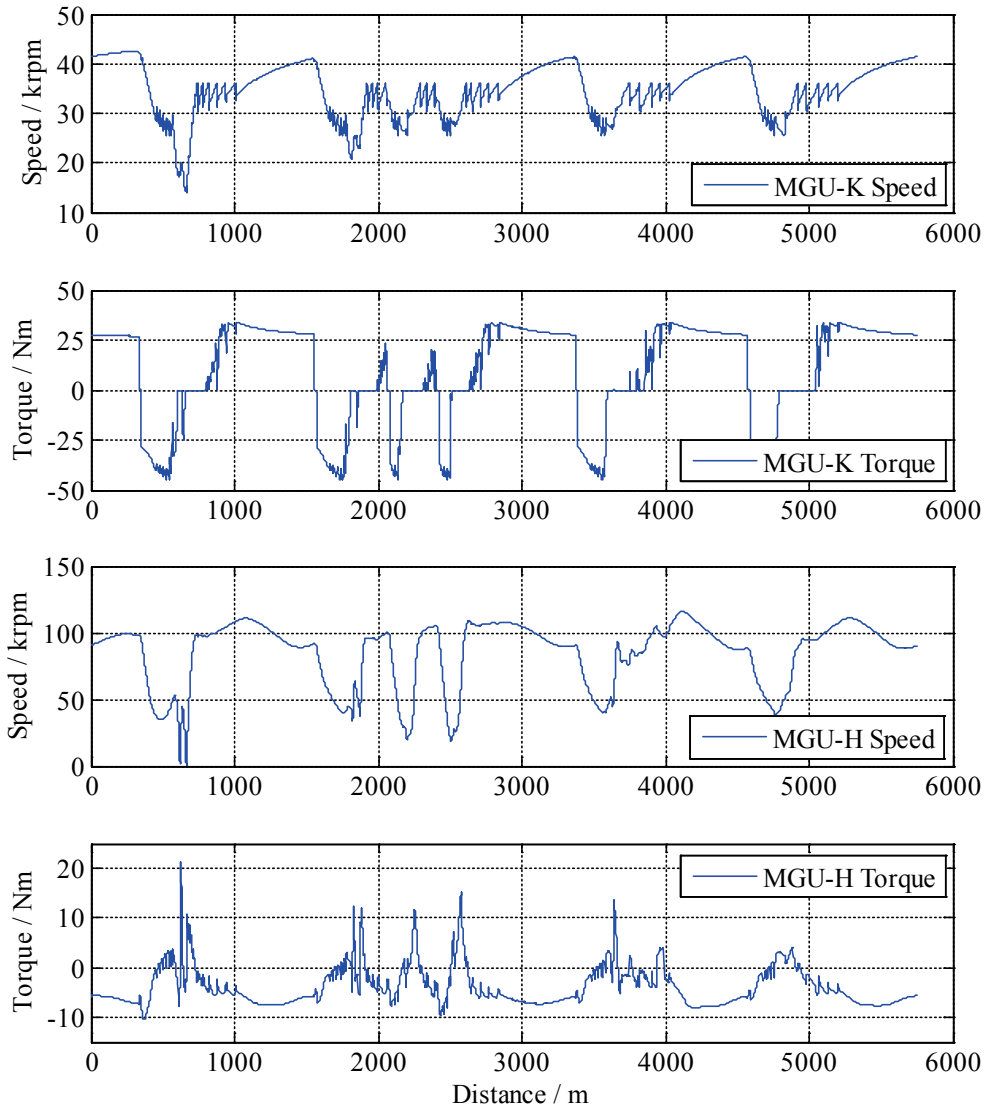

Figure 55: VSM Monza lap electric dive data

The MGU-H profiles in Figure 55 reflect the operating point of the combustion engine. When the ICE is accelerating from low speeds, the MGU-H produces positive torque to quickly speed up the turbocharger and reduce the turbo lag. In high load operating points, the power harnessed by the exhaust gas turbine is more than necessary for the compressor

turbine, which allows the MGU-H to control the charging pressure by converting the excess power to electricity.

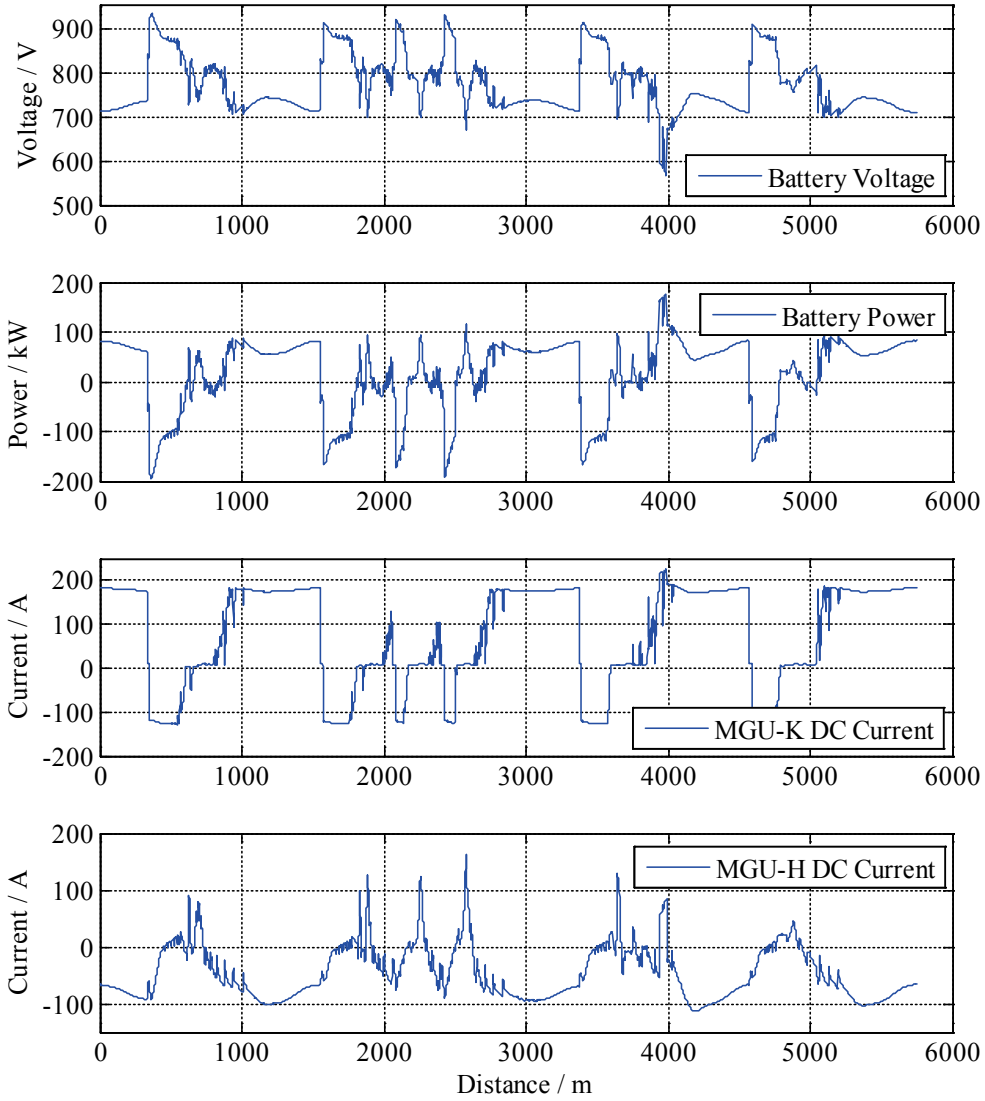

Figure 56: VSM Monza lap ERS data

In Figure 56, data about the energy storage is shown. The top two plots show the battery voltage and power, where the battery voltage is directly connected to the battery power. At high discharge (positive) power, the voltage drops; at high charge (negative) power, the voltage rises. Here, the biggest stress on the battery is at the beginning of braking when MGU-K is fully recuperating and MGU-H is still generating energy from the exhaust gas. The discharge power is usually less, because at full throttle the MGU-K gets its energy from the battery and directly from the MGU-H. This is reflected in the two

lower graphs displaying the DC currents of MGU-K and MGU-H, where the MGU-H current at high loads accounts for about half of the current to the MGU-K.

The losses of both electric drives are plotted in Figure 57. The MGU-K losses are higher than the MGU-H losses, because it has a higher nominal power than the MGU-H and is mostly operated at full load. In contrast, the MGU-H is used to control boost pressure and rarely runs at full load. The losses in the inverters are significantly less than the motor losses due to their higher efficiency.

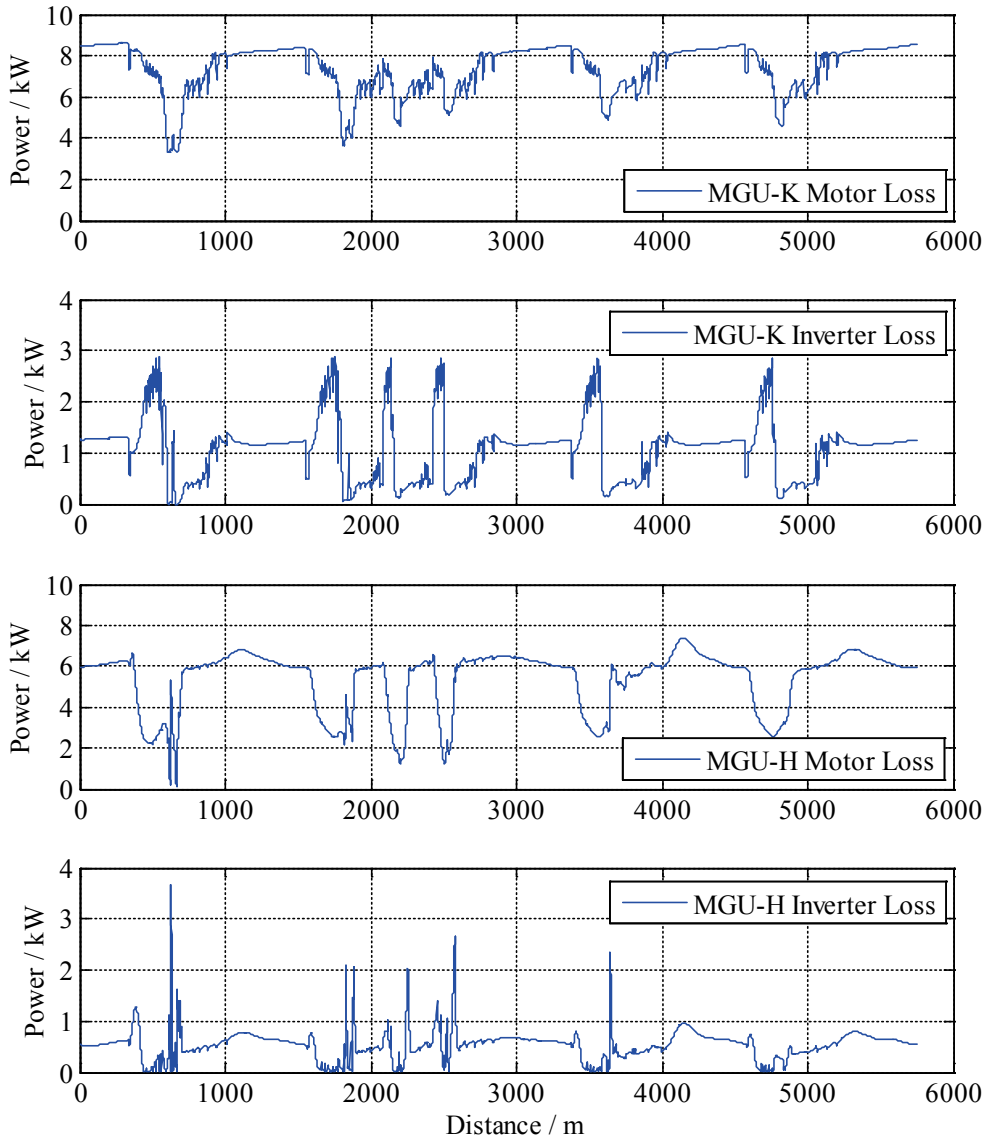

Figure 57: VSM Monza lap electric drive losses

5 DISCUSSION

The goal of the project was to develop a Matlab® Simulink® model for the electric drives in hybrid powertrains for motorsports applications, and their integration in VSM-PTM. The designed model should be easy to use and parameterize, and blend in with the layout and design of the existing vehicle simulation model.

The result of the project is a flexible model for electric drives, which can be used with most types of radial flux machines (e.g. induction machines or permanent magnet synchronous machines). It models the electromechanical and thermal behavior of both motor and inverter, and accounts for the effects of temperature on the motor efficiency. The parameterization of the model is largely dependent on prior measurements, in order to reach high accuracy without requiring extensive knowledge about the design and control of the modelled drive. Therefore, the designed model is suitable for representing an already existing electric drive in a vehicle simulation environment, but is not suitable for most cases of electric drive development.

The designed model was seamlessly integrated in VSM-PTM, functioning well with the other components of the vehicle simulation system. In addition, an existing battery model was adapted and integrated into VSM-PTM, completing the components of a hybrid electric powertrain.

Parts of the model could not be parameterized from real measurements, since the electric drive that was used as a reference broke during the course of this thesis. Additionally, some measurements are suspected to contain errors, which cannot be investigated since the drive is not available anymore. However, the general behavior of the model seems plausible, and general the measurements that were made match well with the simulations.

Future work on this project should include full verification of the model behavior, both for the electromechanical model and the thermal model. Use of several different electric drives for racing applications would also provide information about the accuracy of the model for various types of electric drives. Since the thermal condition of batteries is a very important factor in vehicles, a thermal model for the battery would also be valuable for future applications.

6 REFERENCES

[1] M. Ehsani, Y. Gao and J. Miller: "Hybrid Electric Vehicles: Architecture and Motor Drives", *Proceedings of the IEEE, Vol. 95, No. 4,* pp. 719-728, April 2007.

[2] C. Chan, A. Bouscayrol and K. Chen: "Electric, Hybrid, and Fuel-Cell Vehicles: Architectures and Modeling", *IEEE Transactions On Vehicular Technology, Vol. 59, No. 2,* pp. 589-598, February 2010.

[3] Fédération Internationale de l'Automobile: "2009 F1 Technical Regulations", 11 July 2008. [Online]. Available: http://argent.fia.com/web/fia-public.nsf/90D889BE20961303C1257483004B8AC0/$FILE/1-2009%20F1%20TECHNICAL%20REGU LATIONS%2011-07-2008.pdf. [Accessed 19 March 2015].

[4] Fédération Internationale de l'Automobile: "2015 F1 Technical Regulations", 03 December 2014. [Online]. Available: http://www.fia.com/sites/default/files/regulation/file/2015%20TECHNICAL%20REGULATIONS%202014-12-03.pdf. [Accessed 20 March 2015].

[5] J. Jwan: "www.biser3a.com", [Online]. Available: http://biser3a.com/formula-1/explained-formula-1s-energy-recovery-system-ers/. [Accessed 19 March 2015].

[6] D. Schröder: "Elektrische Antriebe – Grundlagen", Berlin Heidelberg: Springer Vieweg, 2013, ISBN: 978-3-6423-0470-5.

[7] N. Mohan: "Electric Machines and Drives", Hoboken: John Wiley & Sons, 2012, ISBN: 978-1-118-07481-7.

[8] T. Finken, M. Felden and K. Hameyer: "Comparison and design of different electrical machine types regarding their applicability in hybrid electrical vehicles", *Electrical Machines, 2008. ICEM 2008. 18th International Conference on,* pp. 1-5, 6.-9. September 2008.

[9] A. Mathoy: "Die Entwicklung bei Batterien und Antriebstechnik für Elektroautomobile", *Bulletin SEV/AES,* pp. 8-13, January 2008.

[10] Z. Zhu and C. Chan: "Electrical machine topologies and technologies for electric, hybrid, and fuel cell vehicles", *Vehicle Power and Propulsion Conference, 2008. VPPC '08. IEEE,* pp. 1-6, 3-5 September 2008.

[11] R. Fischer: “Elektrische Maschinen”, München, Wien: Carl Hanser Verlag, 2004, ISBN: 978-3-4464-0613-1.

[12] R. Park: "Two-reaction theory of synchronous machines generalized method of analysis-part I", *American Institute of Electrical Engineers, Transactions of the, vol.48, no.3,,* pp. pp.716,727, July 1929.

[13] D. Schröder: “Regelung von Antriebssystemen”, Berlin Heidelberg: Springer-Verlag, 2009, ISBN: 978-3-540-89613-5.

[14] J. Pyrhönen, T. Jokinen and V. Hrabovcova: “Design of Rotating Electrical Machines”, Second Edition, West Sussex, United Kingdom: John Wiley & Sons Ltd, 2014, ISBN: 978-1-118-58157-5.

[15] A. Krings: “Iron Losses in Electrical Machines - Influence of Material Properties, Manufacturing Processes, and Inverter Operation”, Ph.D. dissertation, Stockholm: KTH School of Electrical Engineering, 2014.

[16] J. Schützhold and W. Hofmann: "Analysis of the Temperature Dependance of Losses in Electrical Machines", *IEEE Energy Conversion Congress and Exposition (ECCE),* pp. 3159-3165, 15-19 September 2013.

[17] J.-H. Seo, D.-K. Woo, T.-K. Chung and H.-K. Jung: "A Study on Loss Characteristics of IPMSM for FCEV Considering the Rotating Field", *IEEE TRANS. ON MAGNETICS, VOL. 46, NO. 8,* pp. 3213-3216, August 2010.

[18] J. Mikleš and M. Fikar: “Process Modelling, Identification, and Control”, Berlin Heidelberg New York: Springer, 2007, ISBN 978-3-540-71969-4.

[19] A. Boglietti, A. Cavagino, M. Lazzari and M. Pastorelli: "A Simplified Thermal Model for Variable-Speed Self-Cooled Industrial Induction Motor", *IEEE TRANSACTIONS ON INDUSTRY APPLICATIONS, VOL. 39, NO. 4,* pp. 945-952, July/August 2003.

[20] M. Fénot, Y. Bertin, E. Dorignac and G. Lalizel: "A review of heat transfer between concentric rotating cylinders with or without axial flow", *International Journal of Thermal Sciences,* pp. 1138-1155, March 2011.

[21] K. Yamazaki: "Iron Loss Analysis of Interior Permanent-Magnet Synchronous Motors—Variation of Main Loss Factors Due to Driving Condition", *IEEE TRANSACTIONS ON INDUSTRY APPLICATIONS, VOL. 42, NO. 4,* pp. 1045-1052, July/August 2006.

[22] UQM Technologies Inc.: "UQM PowerPhase 75 Datasheet", [Online]. Available: http://www.neweagle.net/support/wiki/docs/Datasheets/UQM/PP75.pdf. [Accessed 9 October 2014].

[23] W. Pittenger: "Monza Track Map - Italien Grand Prix - Wikipedia, the free encyclopedia", 14 September 2008. [Online]. Available: http://en.wikipedia.org/wiki/Italian_Grand_Prix#/media/File:Monza_track_map.svg. [Accessed 28 April 2015].

7 APPENDIX

APPENDIX A MATLAB CODE: PARAMETER GENERATION

```
% ********************************************************************
% Read measurement-data from Excel-File and generate parameter-maps
% Alexander Jedinger
% 10.12.2014
%
% All thermal parameters are fitted to meet the recorder-file measurements


%% Read Excel File

[filename, pathname] = uigetfile( ...
        {'*.xls',   'XLS - Excel'; ...
         '*.*',     '*.* - All Files'}, ...
         'Select an EXCEL file');

if filename==0 return; end;

targetfile = [pathname filename];
[A,B] = xlsread([pathname filename], 'Measurement_Data');

xls_n = A(:, 1);
xls_T = A(:, 2);
xls_eta_motor = A(:, 3);
xls_eta_inv = A(:, 4);
xls_Is = A(:, 5);
xls_T_winding = A(:, 6);


%% Motor Parameters

% Base Power [W]
Base_Power = 45160;  %To match with 155Nm

% Base Torque [Nm]
Base_Torque = 155; %To cover all the points from the dyno

% Base Speed [rpm]
Base_Speed = 2875;

% Maximum Speed [rpm]
Max_Speed = 8000;

% Minimum Voltage for full power [V]
Vdc_min = 400;

% Number of Phases [-]
Phases = 3;

% Motor inertia [kg.m^2]
inertia = 0.003;

% Motor viscous friction [kg.m^2]
friction = 0.004;

% Average stator winding resistance (per phase) [Ohm]
Rs = 13.48e-3;
% stator winding temperature at resistance measurement [°C]
T_Rs = 25;
% Temperature coefficient of Stator Winding [1/K]
Rs_alpha = 3.9e-3;

% PT1 torque delay characteristics
    tau_torque_delay = 5e-3; %Time constant
%     [num, den] = tfdata(c2d(tf(1,[tau 1]),param.Solver.StepSize),'v');
%     param.Motor.TorqueDelay.Num = num;
```

```
%     param.Motor.TorqueDelay.Den = den;

% Maximum Speed Torque Limitation Curve (for plotting it in the figures)
    Max_Speed_Torque.n = 0:Max_Speed/20:Max_Speed;
    Max_Speed_Torque.T = ...
    [Base_Torque*ones(1,sum(Max_Speed_Torque.n<=Base_Speed)) ...
     Base_Power./(Max_Speed_Torque.n(Max_Speed_Torque.n>Base_Speed)*pi/30)];

% Maximum Speed-Torque Lookuptable (including dependence on Vdc)
    Vdc = 0.2:0.2:1;
    Base_Speed_vdc = (Base_Power.*Vdc)/Base_Torque *30/pi;

    n_tmp = 0:Max_Speed/100:Max_Speed;
    T_tmp = zeros(length(Vdc), length(n_tmp));
    for i=1:length(Vdc)
        T_tmp(i,:) = [Base_Torque*ones(1,sum(n_tmp<=Base_Speed_vdc(i))) ...
         Base_Power*Vdc(i)./(n_tmp(n_tmp>Base_Speed_vdc(i))*pi/30)];
    end

    figure();
    plot(n_tmp, T_tmp, 'LineWidth', 2);
    grid on;
    axis([0,8000,0,160]);
    set(gca,'ytick',0:20:160);
    legend('0.2 V_D_C','0.4 V_D_C', '0.6 V_D_C', '0.8 V_D_C', '1 V_D_C');
    xlabel('Rotor-Speed / rpm');
    ylabel('|Torque| / Nm');
    title('Power-limitation due to DC-Voltage');
    set(findall(gcf,'type','text'),'FontName','Times New Roman', 'FontSize', 12);
    set(gca,'FontName','Times New Roman', 'FontSize', 12);
    %print('TorqueLimitOverVDC','-dmeta');

    Max_Speed_Torque_LUT.n = n_tmp;
    Max_Speed_Torque_LUT.Vdc = Vdc*Vdc_min;
    Max_Speed_Torque_LUT.T = T_tmp;


%% Stator Current Lookuptable
    xnodes = 0:Max_Speed/20:Max_Speed;
    ynodes = -Base_Torque:Base_Torque/20:Base_Torque;

    StatorCurrentMap.n = xnodes;
    StatorCurrentMap.T = ynodes;
    StatorCurrentMap.Is = gridfit(xls_n,xls_T,xls_Is,xnodes,ynodes,'smoothness',0.3);

    figure();
    v = 0:20:180;
    [C,h] = contour(xnodes,ynodes,StatorCurrentMap.Is, v);
    clabel(C,h);
    hold on; grid on;
    plot(Max_Speed_Torque.n,Max_Speed_Torque.T,'black');
    plot(Max_Speed_Torque.n,-Max_Speed_Torque.T,'black');
    axis([0,8000,-160,160])
    set(gca,'ytick',-160:20:160);
    xlabel('Rotor-Speed in rpm');
    ylabel('Torque in Nm');
    title('Stator Current Map');


%% Iron and other Loss Lookuptable

    % Calculate Stator Resistance at Temperature of Measurement
    Rs_hot = Rs*(1 + Rs_alpha*(xls_T_winding - T_Rs));

    % Generation of Lookuptable
    % Calculation of Copper Losses (Is is stator current from measurement)
    P_loss_copper = 3*Rs_hot.*xls_Is.^2;

    % Calculation of Iron Losses
    % because of varying definition of eta, the Losses have to be
    % calculated differntly, according to direction of energyflow
    P_mot = xls_n*pi/30 .* xls_T .*(1-xls_eta_motor)./xls_eta_motor;
```

```
    P_gen = xls_n*pi/30 .* xls_T .*(1-xls_eta_motor);
    P_loss_motor = P_mot.*(xls_T>0) - P_gen.*(xls_T<=0);
    P_loss_iron = P_loss_motor - P_loss_copper;

    xnodes = 0:Max_Speed/20:Max_Speed;
    ynodes = -Base_Torque:Base_Torque/20:Base_Torque;

    IronLossMap.n = xnodes;
    IronLossMap.T = ynodes;
    IronLossMap.P_loss =
gridfit(xls_n,xls_T,P_loss_iron,xnodes,ynodes,'smoothness',0.2);

    figure();
    v = 500:250:3000;
    [C,h] = contour(xnodes,ynodes,IronLossMap.P_loss,v);
    clabel(C,h);
    hold on; grid on;
    plot(Max_Speed_Torque.n,Max_Speed_Torque.T,'black');
    plot(Max_Speed_Torque.n,-Max_Speed_Torque.T,'black');
    axis([0,8000,-160,160]);
    set(gca,'ytick',-160:20:160);
    title('Iron Loss Map');
    xlabel('Rotor-Speed in rpm');
    ylabel('Torque in Nm');


% Inverter Loss Lookuptable
    xnodes = 0:Max_Speed/20:Max_Speed;
    ynodes = -Base_Torque:Base_Torque/20:Base_Torque;

    % Calculation of Inverter-Losses
    % because of varying definition of eta, the Losses have to be
    % calculated differntly, according to direction of energyflow
    P_l_inv_mot = (xls_n*pi/30 .* xls_T + P_loss_motor) .*(1-xls_eta_inv)./xls_eta_inv;
    P_l_inv_gen = (xls_n*pi/30 .*(-xls_T) - P_loss_motor) .*(1-xls_eta_inv);
    P_loss_inverter = P_l_inv_mot.*(xls_T>0) + P_l_inv_gen.*(xls_T<=0);

    InverterLossMap.n = xnodes;
    InverterLossMap.T = ynodes;
    InverterLossMap.P_loss =
gridfit(xls_n,xls_T,P_loss_inverter,xnodes,ynodes,'smoothness',0.8);

    % Make Sure loss is never negative
    InverterLossMap.P_loss(InverterLossMap.P_loss<0) = 0;

    figure();
    v = 0:200:2000;
    [C,h] = contour(xnodes,ynodes,InverterLossMap.P_loss,v);
    clabel(C,h);
    hold on; grid on;
    plot(Max_Speed_Torque.n,Max_Speed_Torque.T,'black');
    plot(Max_Speed_Torque.n,-Max_Speed_Torque.T,'black');
    axis([0,8000,-160,160]);
    set(gca,'ytick',-160:20:160);
    title('Inverter Loss Map');
    xlabel('Rotor-Speed in rpm');
    ylabel('Torque in Nm');


%% Motor Thermal Parameters


% Distribution of iron losses to teeth and yoke
iron_loss_distribution.teethLUT.x = [0 4000 8000];
iron_loss_distribution.rotorLUT.x = iron_loss_distribution.teethLUT.x;
iron_loss_distribution.yokeLUT.x = iron_loss_distribution.teethLUT.x;
iron_loss_distribution.teethLUT.v = [0.6 0.6 0.55];
iron_loss_distribution.rotorLUT.v = [0.1 0.13 0.25];
iron_loss_distribution.yokeLUT.v = [0.3 0.27 0.2];

% Masses [kg]
mass.rotor = 9.5;
mass.teeth = 5;
```

```
mass.winding = 11;
mass.yoke = 12;
mass.coolant = 2;
mass.coolant_radiator = 3;
mass.housing = 2;


% Heat capacities [J/(kg K)]
heat_capacity.rotor = 500;
heat_capacity.teeth = 500;
heat_capacity.winding = 385;
heat_capacity.yoke = 500;
heat_capacity.coolant = 4181; %Water at 50°C
heat_capacity.housing = 897; % assuming Aluminum

% thermal Resistances [K/W]
    % Geometry Data [m] (based on the UQM Motor)
    airgap_length = 1e-3;
    slot_depth = 40e-3;
    slot_width_back = 24e-3;
    tooth_width = 20e-3;
    YokeThickness = 40e-3;
    l_Yoke = YokeThickness/2;
    number_of_slots = 12;
    rotor_diameter = 90e-3;
    stator_diameter = 250e-3;
    stack_height = 140e-3;
    thickness_cooling_jacket = 10e-3;

    % heat transition coefficient [W/(m^2 K)]
    alpha_Cu2Stator = 180; %Assuming a reasonable value (without any calculations)
    alpha_Yoke2Coolant = 580; %From UQM Measurement in Nominal Point

    % heat transition coefficient from rotor to stator
        nu_air = 14.95e-6; %kinematic viscosity of air at 25°C
        a_air = 20e-6; %thermal diffusity of air at 20°C and 1 bar
        k_air = 0.0262; %thermal conductivity of air
        omega = 2875*pi/30; %(0:Max_Speed/10:Max_Speed)*pi/30; %speed vector
        R1 = rotor_diameter/2;
        R2 = R1 + airgap_length;

        N_Taylor = sqrt(omega^2*R1*((R2-R1)/2)^3 /nu_air^2);
        N_Prantl = nu_air/a_air;
        N_Nusselt = 0.23*N_Taylor^0.63 *N_Prantl^0.27;

        alpha_Rotor2Stator = N_Nusselt*k_air/airgap_length;

    % thermal conductivity [W/(m K)]

    %using same alpha for Rth coolant to housing
    Rth_coolant_housing = 1/(alpha_Yoke2Coolant*stack_height*(stator_diameter+2*thick-
ness_cooling_jacket)*pi);
    Rth_rotor_teeth = 1/(alpha_Rotor2Stator*(rotor_diameter/2+air-
gap_length/2)*2*pi*stack_height);

% Adjust parameters to match measurement:
    Rth_winding_teeth = 0.023;
    Rth_winding_yoke = 0.053;
    Rth_teeth_yoke = 0.03;
    Rth_yoke_coolant = 0.005;

thermal_resistance.rotor_shaft = 0.2;
thermal_resistance.rotor_teeth = Rth_rotor_teeth;
thermal_resistance.winding_teeth = Rth_winding_teeth; %0.039;
thermal_resistance.winding_yoke = Rth_winding_yoke; %0.1;
thermal_resistance.teeth_yoke = Rth_teeth_yoke; %0.01;
thermal_resistance.yoke_coolant = Rth_yoke_coolant; %0.001;
thermal_resistance.coolant_housing = Rth_coolant_housing; %0.001;
thermal_resistance.housing_environment = 0.3;

% initial temperatures [°C]
initial_temp.rotor = 96;
initial_temp.teeth = 85;
initial_temp.winding = 95;
```

```
initial_temp.yoke = 60;
initial_temp.housing = 52;
initial_temp.coolant = 56.5;

temp_environment_offset = 0;
temp_shaft = 65;


%% Inverter Thermal Parameters

% % thermal resistances [K/W]
Inv.thermal_resistance.junction_heatsink = 0.013;
Inv.thermal_resistance.heatsink_coolant = 0.013;
Inv.thermal_resistance.coolant_housing = 0.08;
Inv.thermal_resistance.housing_environment = 0.3;

% Masses [kg]
Inv.mass.junction = 0.05;
Inv.mass.heatsink = 1.5;
Inv.mass.coolant = 1.8;
Inv.mass.housing = 0.5;

% Heat capacities [J/(kg K)]
Inv.heat_capacity.junction = 80;
Inv.heat_capacity.heatsink = 897;  %assuming aluminum
Inv.heat_capacity.coolant = 4181; %Water at 50°C
Inv.heat_capacity.housing = 897; %assuming aluminum


% Temperatures
Inv.initial_temp.junction = 92;
Inv.initial_temp.heatsink = 55;
Inv.initial_temp.housing = 52;
Inv.initial_temp.coolant = 54.5;


%% Thermal Properties for Water Circuit

% Masses of coolant
Fluidmass.Radiator = 2;
Fluidmass.toRadiator = 0.5;
Fluidmass.fromRadiator = 0.5;



%% Save Parameter File

%Write to Parameter Struct
MDL.ARES.EPT.MGUH.Base_Power.v = Base_Power;
MDL.ARES.EPT.MGUH.Base_Torque.v = Base_Torque;
MDL.ARES.EPT.MGUH.Base_Speed.v = Base_Speed;
MDL.ARES.EPT.MGUH.Max_Speed.v = Max_Speed;
MDL.ARES.EPT.MGUH.Vdc_min.v = Vdc_min;
MDL.ARES.EPT.MGUH.NumberOfPhases.v = Phases;
MDL.ARES.EPT.MGUH.Inertia.v = inertia;
MDL.ARES.EPT.MGUH.Rs.v = Rs;
MDL.ARES.EPT.MGUH.T_Rs.v = T_Rs;
MDL.ARES.EPT.MGUH.Rs_alpha.v = Rs_alpha;
MDL.ARES.EPT.MGUH.tau_torque_delay.v = tau_torque_delay;
MDL.ARES.EPT.MGUH.MaxSpeedTorqueMap.x = Max_Speed_Torque_LUT.n;
MDL.ARES.EPT.MGUH.MaxSpeedTorqueMap.y = Max_Speed_Torque_LUT.Vdc;
MDL.ARES.EPT.MGUH.MaxSpeedTorqueMap.v = Max_Speed_Torque_LUT.T;
MDL.ARES.EPT.MGUH.StatorCurrentMap.x = StatorCurrentMap.n;
MDL.ARES.EPT.MGUH.StatorCurrentMap.y = StatorCurrentMap.T;
MDL.ARES.EPT.MGUH.StatorCurrentMap.v = StatorCurrentMap.Is;
MDL.ARES.EPT.MGUH.IronLossMap.x = IronLossMap.n;
MDL.ARES.EPT.MGUH.IronLossMap.y = IronLossMap.T;
MDL.ARES.EPT.MGUH.IronLossMap.v = IronLossMap.P_loss;
MDL.ARES.EPT.MGUH.InverterLossMap.x = InverterLossMap.n;
MDL.ARES.EPT.MGUH.InverterLossMap.y = InverterLossMap.T;
MDL.ARES.EPT.MGUH.InverterLossMap.v = InverterLossMap.P_loss;
```

```
MDL.ARES.EPT.MGUH.Thermal.Mot.iron_loss_distribution.teeth.v =
iron_loss_distribution.teeth;
MDL.ARES.EPT.MGUH.Thermal.Mot.iron_loss_distribution.yoke.v =
iron_loss_distribution.yoke;
MDL.ARES.EPT.MGUH.Thermal.Mot.iron_loss_distribution.rotor.v =
iron_loss_distribution.rotor;
MDL.ARES.EPT.MGUH.Thermal.Mot.mass.rotor.v = mass.rotor;
MDL.ARES.EPT.MGUH.Thermal.Mot.mass.teeth.v = mass.teeth;
MDL.ARES.EPT.MGUH.Thermal.Mot.mass.winding.v = mass.winding;
MDL.ARES.EPT.MGUH.Thermal.Mot.mass.yoke.v = mass.yoke;
MDL.ARES.EPT.MGUH.Thermal.Mot.mass.coolant.v = mass.coolant;
MDL.ARES.EPT.MGUH.Thermal.Mot.mass.housing.v = mass.housing;
MDL.ARES.EPT.MGUH.Thermal.Mot.heat_capacity.rotor.v = heat_capacity.rotor;
MDL.ARES.EPT.MGUH.Thermal.Mot.heat_capacity.teeth.v = heat_capacity.teeth;
MDL.ARES.EPT.MGUH.Thermal.Mot.heat_capacity.winding.v = heat_capacity.winding;
MDL.ARES.EPT.MGUH.Thermal.Mot.heat_capacity.yoke.v = heat_capacity.yoke;
MDL.ARES.EPT.MGUH.Thermal.Mot.heat_capacity.coolant.v = heat_capacity.coolant;
MDL.ARES.EPT.MGUH.Thermal.Mot.heat_capacity.housing.v = heat_capacity.housing;
MDL.ARES.EPT.MGUH.Thermal.Mot.thermal_resistance.rotor_shaft.v =
thermal_resistance.rotor_shaft;
MDL.ARES.EPT.MGUH.Thermal.Mot.thermal_resistance.rotor_teeth.v =
thermal_resistance.rotor_teeth;
MDL.ARES.EPT.MGUH.Thermal.Mot.thermal_resistance.winding_teeth.v =
thermal_resistance.winding_teeth;
MDL.ARES.EPT.MGUH.Thermal.Mot.thermal_resistance.winding_yoke.v =
thermal_resistance.winding_yoke;
MDL.ARES.EPT.MGUH.Thermal.Mot.thermal_resistance.teeth_yoke.v =
thermal_resistance.teeth_yoke;
MDL.ARES.EPT.MGUH.Thermal.Mot.thermal_resistance.yoke_coolant.v =
thermal_resistance.yoke_coolant;
MDL.ARES.EPT.MGUH.Thermal.Mot.thermal_resistance.coolant_housing.v =
thermal_resistance.coolant_housing;
MDL.ARES.EPT.MGUH.Thermal.Mot.thermal_resistance.housing_environment.v =
thermal_resistance.housing_environment;
MDL.ARES.EPT.MGUH.Thermal.Mot.initial_temp.rotor.v = initial_temp.rotor;
MDL.ARES.EPT.MGUH.Thermal.Mot.initial_temp.teeth.v = initial_temp.teeth;
MDL.ARES.EPT.MGUH.Thermal.Mot.initial_temp.winding.v = initial_temp.winding;
MDL.ARES.EPT.MGUH.Thermal.Mot.initial_temp.yoke.v = initial_temp.yoke;
MDL.ARES.EPT.MGUH.Thermal.Mot.initial_temp.housing.v = initial_temp.housing;
MDL.ARES.EPT.MGUH.Thermal.Mot.initial_temp.coolant.v = initial_temp.coolant;
MDL.ARES.EPT.MGUH.Thermal.Mot.temp_environment_offset.v = temp_environment_offset;
MDL.ARES.EPT.MGUH.Thermal.Mot.temp_shaft.v = temp_shaft;

MDL.ARES.EPT.MGUH.Thermal.Inv.thermal_resistance.junction_heatsink.v =
Inv.thermal_resistance.junction_heatsink;
MDL.ARES.EPT.MGUH.Thermal.Inv.thermal_resistance.heatsink_coolant.v =
Inv.thermal_resistance.heatsink_coolant;
MDL.ARES.EPT.MGUH.Thermal.Inv.thermal_resistance.coolant_housing.v =
Inv.thermal_resistance.coolant_housing;
MDL.ARES.EPT.MGUH.Thermal.Inv.thermal_resistance.housing_environment.v =
Inv.thermal_resistance.housing_environment;
MDL.ARES.EPT.MGUH.Thermal.Inv.mass.junction.v = Inv.mass.junction;
MDL.ARES.EPT.MGUH.Thermal.Inv.mass.heatsink.v = Inv.mass.heatsink;
MDL.ARES.EPT.MGUH.Thermal.Inv.mass.coolant.v = Inv.mass.coolant;
MDL.ARES.EPT.MGUH.Thermal.Inv.mass.housing.v = Inv.mass.housing;
MDL.ARES.EPT.MGUH.Thermal.Inv.heat_capacity.junction.v = Inv.heat_capacity.junction;
MDL.ARES.EPT.MGUH.Thermal.Inv.heat_capacity.heatsink.v = Inv.heat_capacity.heatsink;
MDL.ARES.EPT.MGUH.Thermal.Inv.heat_capacity.coolant.v = Inv.heat_capacity.coolant;
MDL.ARES.EPT.MGUH.Thermal.Inv.heat_capacity.housing.v = Inv.heat_capacity.housing;
MDL.ARES.EPT.MGUH.Thermal.Inv.initial_temp.junction.v = Inv.initial_temp.junction;
MDL.ARES.EPT.MGUH.Thermal.Inv.initial_temp.heatsink.v = Inv.initial_temp.heatsink;
MDL.ARES.EPT.MGUH.Thermal.Inv.initial_temp.housing.v = Inv.initial_temp.housing;
MDL.ARES.EPT.MGUH.Thermal.Inv.initial_temp.coolant.v = Inv.initial_temp.coolant;
MDL.ARES.EPT.MGUH.Thermal.Inv.temp_environment_offset.v = temp_environment_offset;

MDL.ARES.EPT.COOLING.WATER_CIRCUIT.Water_Circulation_Electro.cp_coolant.v =
heat_capacity.coolant;
MDL.ARES.EPT.COOLING.WATER_CIRCUIT.Water_Circulation_Electro.initial_temp_coolant_toRadi
ator.v = initial_temp.coolant;
MDL.ARES.EPT.COOLING.WATER_CIRCUIT.Water_Circulation_Electro.initial_temp_coolant_inRadi
ator.v = initial_temp.coolant;
MDL.ARES.EPT.COOLING.WATER_CIRCUIT.Water_Circulation_Electro.initial_temp_coolant_fromRa
diator.v = initial_temp.coolant;
```

```
MDL.ARES.EPT.COOLING.WATER_CIRCUIT.Water_Circulation_Electro.m_coolant_toRadiator.v =
Fluidmass.toRadiator;
MDL.ARES.EPT.COOLING.WATER_CIRCUIT.Water_Circulation_Electro.m_coolant_inRadiator.v =
Fluidmass.Radiator;
MDL.ARES.EPT.COOLING.WATER_CIRCUIT.Water_Circulation_Electro.m_coolant_fromRadiator.v =
Fluidmass.fromRadiator;


%Save and clear all
save('param_v4_UQM','MDL');
clearvars -except MDL;
```

APPENDIX B MOTOR THERMAL MODEL IN SIMULINK

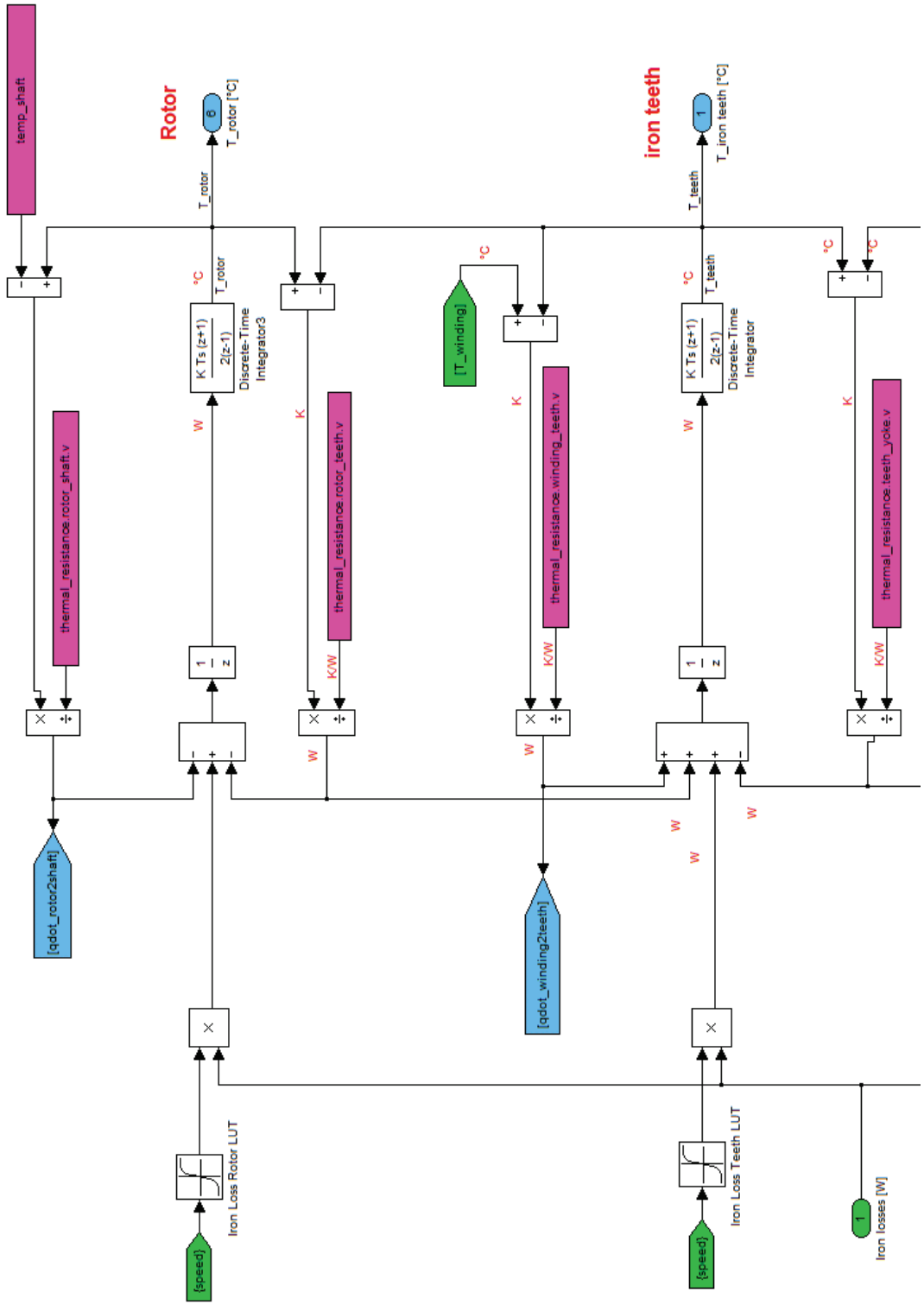

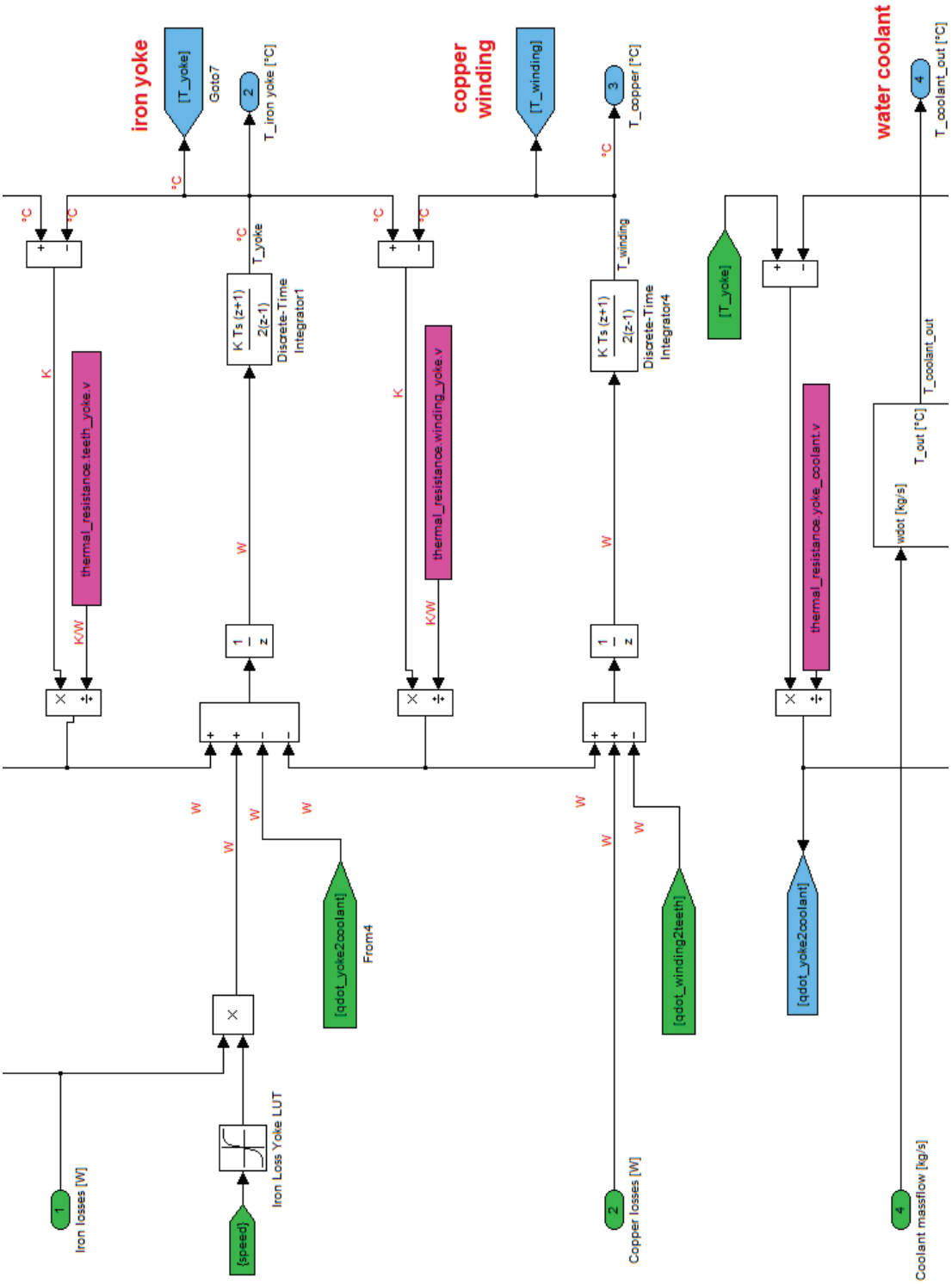
iron yoke
[T_yoke]
Goto7
2
T_iron yoke [°C]
copper winding
[T_winding]
3
T_copper [°C]
water coolant
4
T_coolant_out [°C]
°C
T_yoke
T_winding
K Ts (z+1) / 2(z-1)
Discrete-Time Integrator1
Discrete-Time Integrator4
K
K/W
W
thermal_resistance.teeth_yoke.v
thermal_resistance.winding_yoke.v
thermal_resistance.yoke_coolant.v
1 / z
[qdot_yoke2coolant]
From4
[qdot_winding2teeth]
[qdot_yoke2coolant]
T_coolant_out
T_out [°C]
wdot [kg/s]
1
Iron losses [W]
{speed}
Iron Loss Yoke LUT
2
Copper losses [W]
4
Coolant massflow [kg/s]

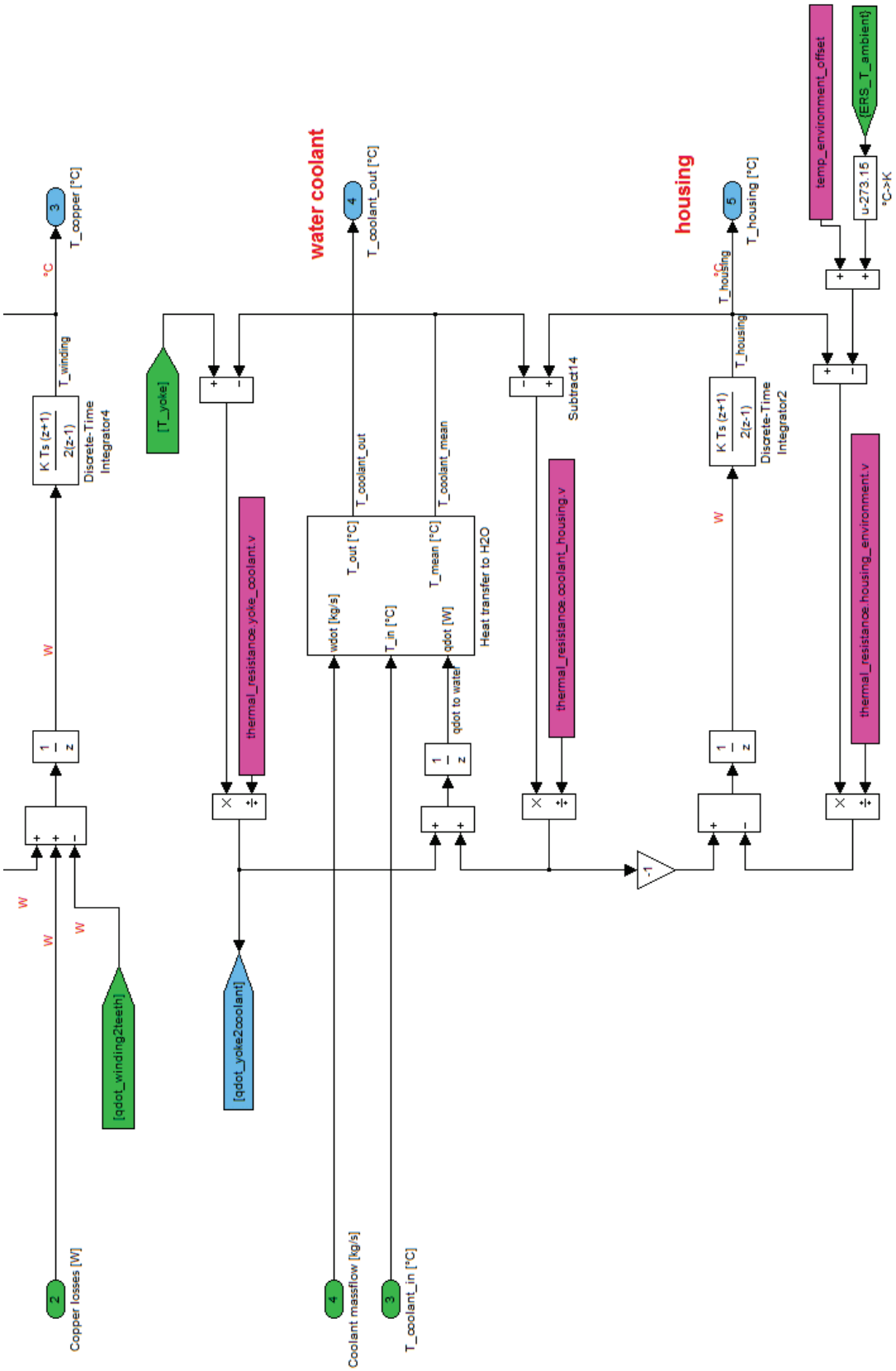
water coolant
housing
T_copper [°C]
T_coolant_out [°C]
T_housing [°C]
temp_environment_offset
[ERS_T_ambient]
u-273.15
°C->K
T_winding
K Ts (z+1) / 2(z-1)
Discrete-Time Integrator4
[T_yoke]
thermal_resistance.yoke_coolant.v
T_coolant_out
T_coolant_mean
T_out [°C]
T_mean [°C]
wdot [kg/s]
T_in [°C]
qdot [W]
Heat transfer to H2O
qdot to water
Subtract14
thermal_resistance.coolant_housing.v
T_housing
K Ts (z+1) / 2(z-1)
Discrete-Time Integrator2
thermal_resistance.housing_environment.v
W
[qdot_winding2teeth]
[qdot_yoke2coolant]
Copper losses [W]
Coolant massflow [kg/s]
T_coolant_in [°C]

APPENDIX C INVERTER THERMAL MODEL IN SIMULINK

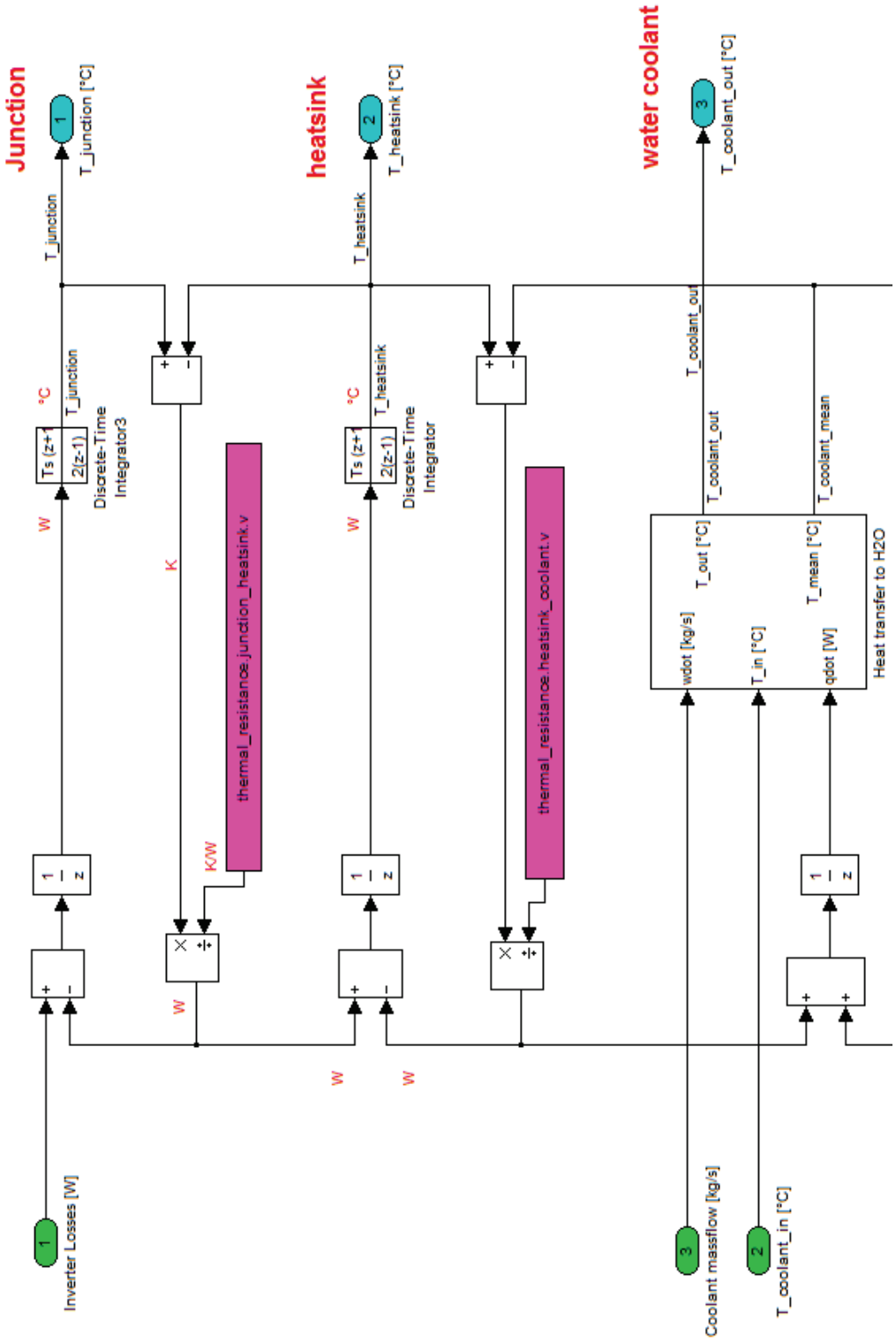

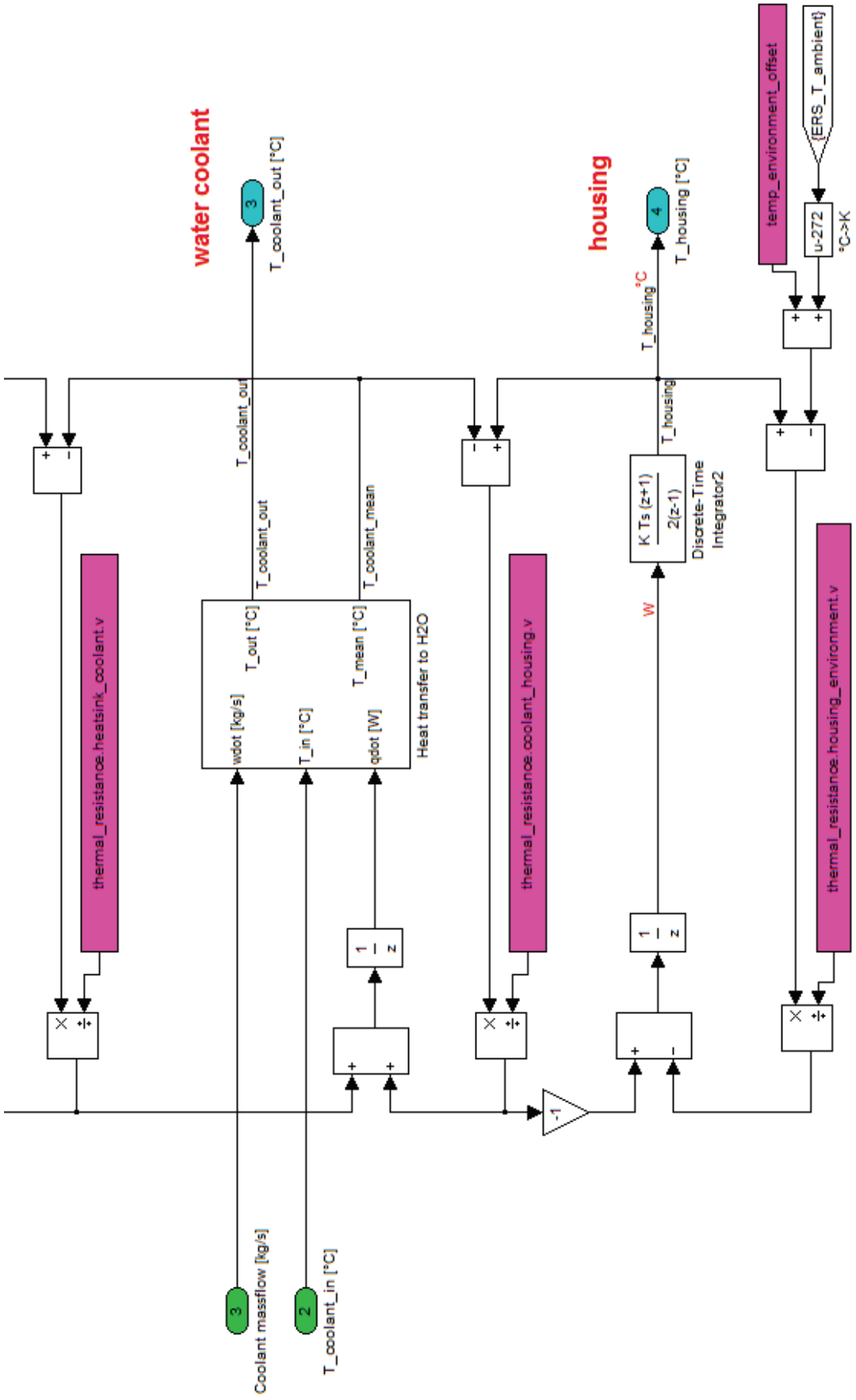
water coolant
housing
T_coolant_out [°C]
T_housing [°C]
temp_environment_offset
ERS_T_ambient
u-272
°C->K
T_housing °C
T_coolant_out
T_coolant_mean
T_housing
K Ts (z+1) / 2(z-1)
Discrete-Time Integrator2
W
T_out [°C]
T_mean [°C]
wdot [kg/s]
T_in [°C]
qdot [W]
Heat transfer to H2O
thermal_resistance.heatsink_coolant.v
thermal_resistance.coolant_housing.v
thermal_resistance.housing_environment.v
Coolant massflow [kg/s]
T_coolant_in [°C]
-1